Microfluidic System for Detecting an Antibiotic

Ruan Vitor Silva Oliveira
Master in Engineering Physics
Department of Physics and Astronomy
Faculty of Sciences of the University of Porto and Faculty of Engineering of the University of Porto
2024/2025

Microfluidic System for Detecting an Antibiotic

Ruan Vitor Silva Oliveira

Dissertation carried out as part of the Master in Engineering Physics

Department of Physics and Astronomy

2024/2025

Supervisor FCUP
Dr. André Pereira, Auxiliar Professor, Porto University

Supervisor CeNTI
Dr. Liliana Truta, R&D Researcher, CeNTI

Designer Supervisor CeNTI
Ana Catarina Ribeiro, Designer, CeNTI

Antes de mais, peço desculpa pela extensão desta dedicatória. Não sabemos quando a vida nos dará novas oportunidades para dedicar bons momentos às pessoas importantes, por isso peço licença para citar alguns nomes.

Começo por dedicar este momento à minha ***Mãe, Simone****, minha fiel incenticadora em todos os sentidos, desde as primeiras passagens aéreas ao apoio emocional, o meu eterno porto seguro. Ao meu* ***Padrasto****,* ***José Luiz,*** *pelo ombro de apoio e pelo equilíbrio nos momentos mais difíceis. Aos meus* ***Avós****,* ***Domingos Ramos e Ernestina****, que sempre cuidaram dos mínimos pormenores da minha infância para que eu chegasse* ***"blindado"*** *à vida adulta; ao* ***Dr. Luli*** *e* ***Dona Olga****, meus fiéis incentivadores e fonte de energia; ao meu amigo* ***Leonardo****, pela parceria em todas as horas, das mais fáceis às mais difíceis, às amigas* ***Rayna*** *e* ***Deise****, pelos risos fáceis cheios de ternura e à minhas* ***Tias Luana*** *e* ***Aurilene****, por serem a minha família e suporte de carinho mesmo tão longe de casa. Bem como a torcida das tias* ***Rute , Luísa, Neuma, Terezinha e Cirlei****.Além dos meus tios* ***Albeto*** *e* ***Ciro****.*

Por fim, queria dedicar também às minhas pacientes ***Tainá*** *e* ***Denise****, que, apesar de terem partido precocemente, tal como o meu* ***avô Domingos****, há dias, continuam vivas em cada gota de alegria, esperança e fé que deixaram em mim.*

Ao meu ***Avô****, não era este o plano, mas consigo ouvir a sua voz a transmitir todo o orgulho em ter um engenheiro na família.*

No intuito de manter o estatuto de bom irmão, dedico, também, aos meus irmãos ***Pedro Luiz*** *e* ***Sophia Victória****, obrigado pela irmandade que me mantém de pé, assim como aos meus primos, tios e demais familiares.*

E dedico a si, ***pessoa de bem****, que venha a ler este texto e que possa, através de atitudes simples, transformar o dia ou a vida de alguém.*

Acknowledgements

Undoubtedly, the moment of giving thanks is one of the most meaningful parts of a thesis. With that in mind, I would like to begin by thanking the CeNTI team, starting with the team leaders, David and Daniela, for accepting my application for this opportunity and, above all, for introducing me to my supervisor, Dr. Liliana Trutta. To Engineer Liliana, my deepest gratitude for being my voice, my feet, my hands, and at times, my neural compass. Thank you for your warmth, dedication, and tireless support in every meeting, every iron solution, and every potentiostat calibration. Likewise, I thank my supervisor for introducing me to my internship godparents, Engineers Pedro António and Sónia Alves. Thank you to my godfather, Pedro, for the partnership, the electronic soldering, and for receiving my technical requests with such humility. To my godmother Sónia, the magical engineer, what a joy it was to have you as my supervisor for good laboratory practices. Thank you, dear godmother, for being my safe harbour and for restoring my energy and strength every time they threatened to fade. Thank you for every coffee and every piece of chocolate shared during this internship.

I also want to thank Designer Ana Ribeiro for her collaboration, dedication, talent, and inspiring creativity. I'm sure that, as a designer, she is number one, truly unbeatable. And to Mrs. Silvia, thank you for welcoming me so warmly and for warming my heart every day at the entrance of CeNTI with your greetings, sweet words, and kind kisses. And, of course, I would like to extend my sincere thanks to the entire CeNTI team, especially Jorge, Ana Moreira, Mariana, Alan, Aline, Talita, João, Vinicius, Isaque Sá, Helder, and all the other collaborators. Thank you for making the days lighter.

Now, I would like to extend my heartfelt thanks to my FCUP community. I want to begin by thanking Professor Dr. André Pereira. Fate had it that my very first lab class was with Professor André, and the cycle comes full circle with him as my internship supervisor. Thank you for your encouragement and for being a true example of a Professor and Researcher. Each of us, as students, aspires to follow in Professor André's footsteps, and we would consider ourselves lucky to possess even 50% of the competence, talent, and drive that he embodies to make a difference. I also want to thank my fellow FCUP classmates, namely Ana Carolina, Elisa, Sara, Rute, Ângela, Isabelle, Bernardo, Caua, Felipe, Rita, Miguel, Ricardo Júnior, Vitória, Joyce, Luca, Júlia and Vinícius. It's only fair to say that, if I've come close to the finish line, it was thanks to your partnership. Thank you, always!

Resumo

O aumento no número de mortes causadas por bactérias resistentes a antibióticos é um alerta que exige medidas urgentes. É fundamental acompanhar de perto a resistência provocada por vestígios de antibióticos presentes em águas residuais, o que reforça a necessidade de investir em sistemas de monitoramento capazes de avaliar esses recursos hídricos de forma mais eficiente e precisa. Com esse propósito, o trabalho desenvolvido no CENTI propôs a criação de um sistema microfluídico modular voltado para o uso de sensores eletroquímicos seletivos à norfloxacina, um dos antibióticos mais comuns encontrados em águas residuais, integrados a outros mecanismos de transdução complementares. Tanto a plataforma microfluídica quanto o sensor foram projetados com foco em alta sensibilidade, seletividade, portabilidade e baixo custo.

O sensor eletroquímico foi produzido por meio de impressão serigráfica, a utilizar tintas de carbono e prata no processo de impressão dos eletrodos. Para garantir a seletividade, foi desenvolvido um polímero com impressão molecular (MIP) a partir de pirrol, com a norfloxacina removida após a eletropolimerização, para gerar cavidades específicas para essa molécula. Também foi criado um polímero controle (NIP), sem norfloxacina, para validar a especificidade da detecção. O sensor foi testado com soluções de antibiótico em tampão de acetato e em amostras reais de água engarrafada e água da torneira, ambas dopadas com norfloxacina. Os resultados apresentaram gama de trabalho entre 0,005 pg/mL e 50,00 µg/mL. As análises por voltametria de onda quadrada revelaram coeficientes de determinação (R^2) iguais a 0,995 para amostras de água da torneira e 0,996 para água engarrafada, medidas em um módulo microfluídico específico para detecção eletroquímica, com declives de -0,0116 ± 0,0003 e 0,0251 ± 0,0006, respectivamente. Os limites de detecção (LOD) e quantificação (LOQ) foram de 0,005 pg/mL. As baixas respostas do NIP e de interferentes confirmaram que o MIP é realmente seletivo para a norfloxacina.

Na concepção dos módulos microfluídicos, bases de Lego foram adaptadas para garantir a fixação segura da configuração em cadeia dos módulos. Além disso, foi proposta uma réplica do cubo microfluídico RUBIK, capaz de integrar, em uma única estrutura, módulos com diferentes mecanismos de transdução a funcionar em paralelo, como os colorimétricos, eletroquímicos e fotoacústicos.

Palavras-chave: Impressão em tela, Sensor eletroquímico, MIP, NIP, Norfloxacina, Pirrol, Eletropolimerização, Microfluídica modular, Limite de detecção (LOD), Limite de quantificação (LOQ), Colorimétrico, Fotoacústico.

Abstract

The growing number of deaths caused by antibiotic-resistant bacteria represents a scenario that demands action. Effective surveillance is necessary regarding resistance induced by traces of antibiotics in wastewater, highlighting the importance of investing in monitoring systems that can assess residual water resources more efficiently and effectively. Recognizing the importance of this cause, the work developed at CENTI proposed the creation of a modular microfluidic system designed for the use of electrochemical sensors selective to norfloxacin (one of the most common antibiotics found in wastewater), coupled with other complementary transduction systems. The microfluidic platform and the sensor were structured to prioritize high sensitivity, selectivity, portability, and the lowest possible cost.

The electrochemical sensor was constructed through laboratory screen printing, utilizing carbon and silver inks during the electrode printing process. To ensure selectivity, a Molecularly Imprinted Polymer (MIP) was produced from pyrrole, with norfloxacin removed after electropolymerization, creating selective cavities for the norfloxacin molecule. A control polymer (NIP) was created without norfloxacin, serving to confirm the specificity of detection. The sensor was evaluated with antibiotic solutions in acetate buffer and in real samples of bottled water and tap water spiked with norfloxacin. The results indicated a working range from 0.005 pg/mL to 50.00 µg/mL. Square wave voltammetry analyses revealed an excellent coefficient of determination (R^2), with values of 0.995 for tap water samples and 0.996 for bottled water measured in a specific microfluidic module for electrochemical sensing, showing slopes of -0.0116 ± 0.0003 and 0.0251 ± 0.0006, respectively. The limits of detection (LOD) and quantification (LOQ) were 0.005 pg/mL. The low responses from the NIP and interferents confirmed that the MIP is selective for norfloxacin.

For the design of the microfluidic modules, Lego bases were adapted to enhance the securement of the modular chain configuration. Additionally, a replica of the RUBIK microfluidic cube was proposed to integrate, within a single structure, modules for different transduction mechanisms in parallel (colorimetric, electrochemical, and photoacoustic).

Keywords: Screen Printing, Electrochemical Sensor, MIP, NIP, Norfloxacin, Pyrrole, Electropolymerization, Modular Microfluidics, Limit of Detection (LOD), Limit of Quantification (LOQ), Colorimetric, Photoacoustic.

Index

List of Tables

List of Figures

List of Graphs

List of Abbreviations

CD	CARBON DOTS
CE	COUNTER ELECTRODE
CNC	COMPUTER NUMERICAL CONTROL
CV	CYCLIC VOLTAMMETRY
CWW	CONVENTIONAL WAVE VOLTAMMETRY
ECDM	ELECTROCHEMICAL DISCHARGE MACHINING
EWOD	ELECTROWETTING-ON-DIELETRIC
FDM	FUSION DEPOSITION MODELING
FTIR	FOURIER-TRANSFORM INFRARED
LOD	LIMIT OF DETECTION
LOQ	LIMIT OF QUANTIFICATION
MIP	MOLECULARLY IMPRINTED POLYMER
MJF	MULTI-JET FUSION
NFX	NORFLOXACIN
NIP	NON-IMPRINTED POLYMER
OPU	OPTICAL PICK-UP UNIT
PDMS	POLYDIMETHYLSILOXANE
PEDOT:PSS	POLY(3,4-ETHYLENEDIOXYTHIOPHENE) POLYSTYRENE SULFONATE
PVC	POLYVINYL CHLORIDE
PY	PYRROLE
RE	REFERENCE ELECTRODE
RBG	RED, GREEN, BLUE (PIXEL)
SLA	STEREOLITHOGRAPHY
SLM	SELECTIVE LASER MELTING
SLS	SELECTIVE LASER SINTERING
SPE	SCREEN-PRINTED ELECTRODES
UV	ULTRAVIOLET
WE	WORKING ELECTRODES

1. Introduction

1.1. Contextualization

This curricular internship was carried out as part of the completion of the master's degree in physical engineering at the Faculty of Sciences of the University of Porto, during the 2024–2025 academic year, within the Dissertation / Curricular Internship course unit. It was developed at the Centre for Nanotechnology and Technical, Functional and Intelligent Materials (CeNTI), in the Smart Materials department, from March 17, 2025, to August 29, 2025, with a work schedule on Mondays and Fridays between 9 a.m. and 5 p.m.

1.2. Company Overview

Founded in 2006, CeNTI is a research and technological development (R&D) institute headquartered in Vila Nova de Famalicão, Braga, Portugal. Specialized in nanotechnology and smart materials, CeNTI's mission is to create innovative products and develop technologies, including functional polymers, smart textiles, sensors/actuators, and other electronic devices, that enhance business competitiveness and promote environmental sustainability.

1.3. Objectives of the Work

The emergence of deaths caused by antibiotic-resistant bacteria has heightened international awareness of the need to monitor traces of antibiotics in water. This concern arises from the fact that even at low concentrations, antibiotics in flowing water can promote the emergence and sharing of resistance strategies among free-living pathogenic microorganisms. In this context, CeNTI proposed offering a highly sensitive, low-cost, and portable solution for detecting, in water, one of the main antibiotics used in medical practice, norfloxacin, based on the design of a screen-printed electrochemical sensor.

In addition to ensuring efficiency at extremely low concentrations, CeNTI prioritized methodologies that minimize the need for reagents and reduce costs associated with expensive operational equipment and clean rooms. The intersection of these goals led to the development of a microfluidic platform manufactured using additive 3D printing techniques. Although initially intended for electrochemical calibration, the platform was designed to analyze samples or analytes in parallel through integrated transduction

systems. Its modular architecture allows easy customization and adaptation to different detection needs.

1.4. Report Structure

This report is organized into eight chapters, each addressing specific thematic content:

- **Chapter 1** – Introduction: This section provides a comprehensive overview of the work and its contextual framework.
- **Chapter 2** – Theoretical Foundations: The relevance of the topic is discussed, along with key strategies for detecting quinolones in water, as well as materials and microfluidic fabrication methods.
- **Chapter 3** – Materials and Methods: This chapter outlines the reagents and equipment used, as well as the primary protocols and procedures employed for electrode printing and the preparation of experimental assays.
- **Chapter 4** – Results: The outcomes related to the preparation of the molecularly imprinted polymer (MIP) and, in parallel, the control sensor (NIP, Non-Imprinted Polymer) are presented. The sensor's performance is evaluated through calibration curves and electrochemical measurements of antibiotic samples in buffer solution and real water samples (bottled and tap water). The sensor's behaviour will also be evaluated using norfloxacin-doped samples, both inside and outside the electrochemical microfluidic module.
- **Chapter 5 – Microfluidic Modularity Strategies:** This section introduces the modular design strategies and describes the main design models tested for modular implementation.
- **Chapter 6 – Conclusions:** The main findings are summarized, followed by suggestions for future work in **Chapter 7**.
- **Chapter 8 – Appendices:** This final chapter includes supplementary content, such as alternative transduction methods for norfloxacin concentration that may be integrated into the setup's modules, as well as additional design materials and fabrication methodologies applicable to microfluidic modules intended for purposes beyond the scope of this study.

2. Theoretical Foundations

2.1. Public health

It is indisputable that, when it comes to life expectancy at birth, we now have a greater chance of reaching 100 years than at any other time in human history. Each additional month of life expectancy represents decades of scientific research, vast financial resources, and the effort of thousands of people. Clearly, ongoing medical research yields results. In 2023, the average life expectancy in Europe approached 82 years [1]. A hundred years ago, in the 1920s, living to between 45 and 50 years was considered most likely [2], an age that today is unthinkable as a marker for the end of life.

Undoubtedly, the rise in life expectancy is due, in part, to therapeutic advances in medicine that have responded to a wide range of diseases, with severe infections being particularly notable. In this regard, the development of antibiotics became the principal weapon for treating and surviving infections, alongside hygiene measures, sterilization, and vaccine development. The first antibiotic, Salvarsan, emerged in 1909 through Paul Ehrlich and was used to treat syphilis, an infectious disease. It was in 1928 that Alexander Fleming's discovery of penicillin marked the beginning of the "Antibiotic Era," which would later be developed and widely used during the calamity of World War II.

It is undeniable that significant therapeutic advances have been made, with billions of dollars invested and hundreds of thousands of scientists working towards medical progress. However, certain challenges continue to trouble the scientific community from time to time, with infectious diseases included among them. Recent studies project that deaths caused by bacterial infections may exceed 40 million cases by 2050 [3]. The primary concern surrounding this figure relates to the fact that many of these deaths are expected to be caused by microorganisms resistant to the main clinical antimicrobials. The World Health Organization (WHO) has been issuing daily warnings about antimicrobial resistance (AMR), a highly dynamic process of natural selection that occurs in microorganisms, including bacteria, fungi, and viruses. This process has been significantly accelerated due to the excessive and indiscriminate use of antibiotics, not only in human medicine, but also in veterinary and agricultural practices, sectors which currently contribute significantly to the worsening of this issue (Figure 1) [4].

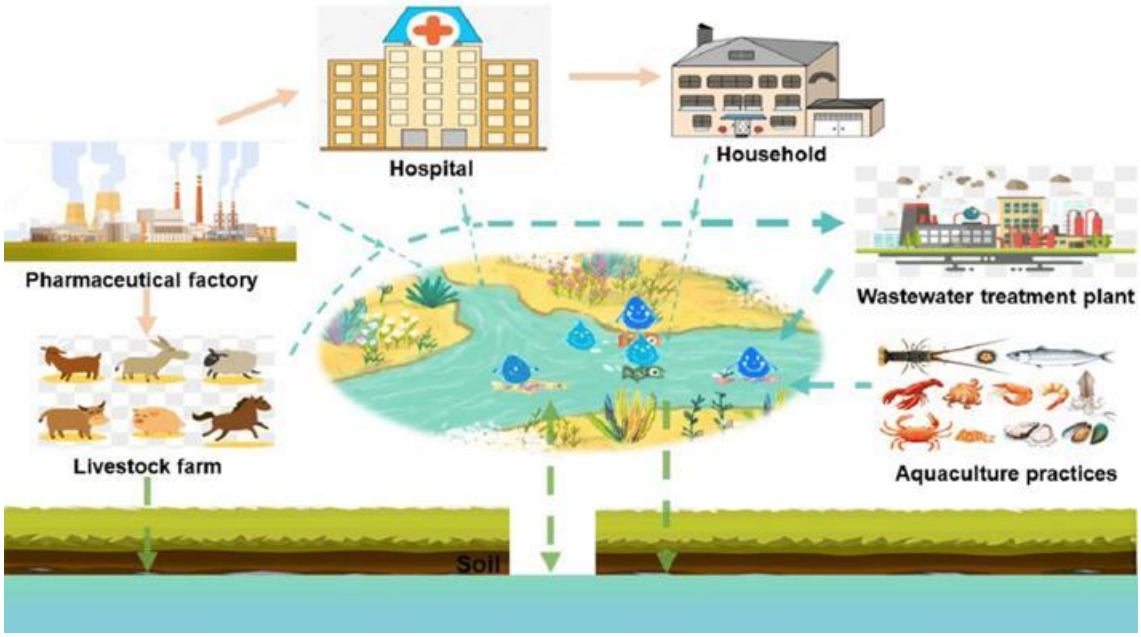

Figure 1 Diagram highlights the various sources of antibiotic trace pollutants in aquatic ecosystems, including hospitals, households, livestock farms, and aquaculture practices [5].

For comparative purposes, the same study [3] indicated that the likelihood of developing sepsis caused by antibiotic-resistant organisms was 25% higher in 2019 compared to 1990. Moreover, the World Health Organization (WHO) expects that, by 2050, deaths resulting from sepsis caused by infections with resistant microorganisms, those that do not respond to conventional treatments, will surpass deaths caused by cancer. The estimated economic impact is projected to reach trillions of dollars per year by 2050 [3].

2.2. Antibiotic Monitoring

The most common way to classify antibiotics considers factors such as their molecular structure, mode of action within the body, route of administration (whether by injection, orally, or through topical application), and the range of microorganisms they effectively target. Antibiotics with similar chemical structures usually show comparable efficacy, toxicity, and allergic reactions. The main categories of antibiotics, based on their chemical or molecular composition, include Beta-lactams, Macrolides, Tetracyclines, Quinolones, and Aminoglycosides.

Among the antibiotics that microorganisms most rapidly develop resistance to, fluoroquinolones stand out [6]. The discovery of norfloxacin and ciprofloxacin in the early 1980s marked the emergence of fluoroquinolones, a new class of antibiotics that quickly

gained widespread use in treating urinary and respiratory infections. These compounds interfere with enzymes essential for DNA replication, particularly in Gram-negative bacteria [7], and were soon heavily prescribed by the medical community.

However, due to the speed at which bacteria adapt and develop resistance, quinolones began to be used more as a second-line option, especially in cases where first-line antibiotics failed or could not be used due to allergies [8]. In fact, microorganisms can become resistant much faster than previously expected. This rapid pace became evident in 1987, when researchers identified fluoroquinolone-resistant strains just four years after the patent was filed [9]. Other studies have shown that resistance can develop in even less time; some report the emergence of resistant strains after just a single three-day course of ciprofloxacin treatment [10].

From an epidemiological perspective, researchers in the United States observed an increase in the proportion of Escherichia coli (E. coli) strains causing acute pyelonephritis that were resistant to antibiotics, from 0.2% in 1997 to 6.3% in 2010 [11]. In Spain, the rate of quinolone-resistant strains rose from 9% in 1992 to 17% in 1996 [12]. In South Korea, between 2002 and 2004, studies identified resistance rates of 19.8% in similar cases [13].

Despite strict medical guidelines for prescribing quinolone-class antibiotics, their use remains high, largely due to the high incidence of urinary and respiratory infections. Recent data covering the period from 1990 to 2021 indicate a significant 66.4% increase in urinary tract infections [14]. This rise has led to greater antibiotic consumption, which in turn increases the presence of these compounds in the environment.

2.3. Pharmacokinetics of Norfloxacin and the Environment

Pharmacokinetics examines how the body handles a substance, from absorption and distribution to metabolism and elimination. In the case of antibiotics like quinolones, the way the body processes the drug directly influences the development of bacterial resistance. Adjusting the dose and treatment schedule plays a crucial role in ensuring the therapy works effectively while minimizing bacterial exposure to low drug concentrations, which can accelerate resistance.

Hospitals and households often release quinolones into wastewater without breaking them down (Norfloxacin, in part, leaves the body naturally unchanged), contributing to environmental contamination. These active compounds in the environment put microbial communities under selective pressure, which can worsen resistance. Understanding

how quinolones behave in the body is therefore essential, not only for treating infections effectively but also for helping to control the broader spread of antibiotic resistance.

2.3.1. Pharmacokinetics

After oral administration, between 30% and 40% of the norfloxacin is rapidly absorbed through the gastrointestinal tract, while the remainder is eliminated via the faeces. Around 1.5 hours after ingestion (at doses ranging from 400 mg to 800 mg), the drug reaches its peak plasma concentration. The absorbed portion distributes quickly throughout the body, achieving particularly high concentrations in tissues such as the kidneys and prostate, between 100 and 300 times higher than in the bloodstream [15]. Its half-life is approximately 3.25 hours, and it does not accumulate in plasma, even during prolonged treatment. The liver metabolizes most of the norfloxacin, and the body excretes it in the urine, both in its unchanged form and as active metabolites.

Quinolones reach body tissues with ease, which makes them useful for treating a wide variety of infections beyond the urinary tract, such as pneumonia, skin and joint infections, and gastrointestinal conditions. Doctors often turn to ciprofloxacin, levofloxacin, gatifloxacin, and moxifloxacin in these situations [15,16].

On a molecular level, quinolones work by blocking two key enzymes, DNA gyrase and topoisomerase IV, that bacteria need to replicate their DNA. Without these enzymes, the bacteria can’t reproduce, and they eventually die off [16].

Resistance tends to emerge in several ways (see summary of resistance mechanisms in Figure 2). Some bacteria undergo mutations in their own DNA, while others change the permeability of their membranes by reducing porin proteins, which normally allow the antibiotic to enter the cell. In some cases, bacteria adjust the genes that control efflux pumps, pushing the drug out before it can take effect. They can also share resistance genes through plasmids, allowing entire microbial communities to become resistant over time [16].

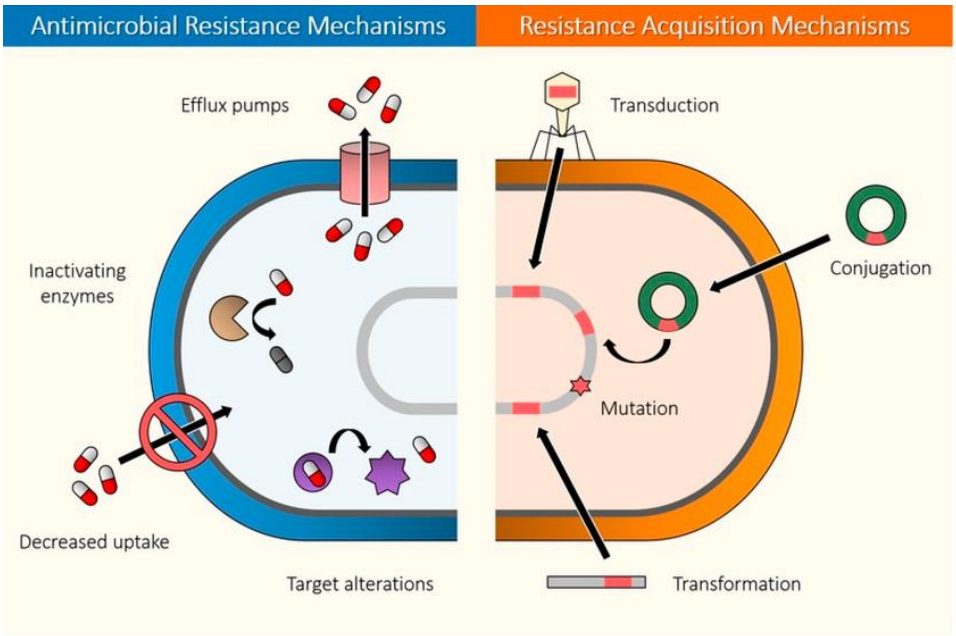

Figure 2 Antimicrobial resistance occurs when bacteria develop mechanisms to neutralize antibiotics. The diagram above illustrates the main resistance mechanisms, including enzymatic inactivation, efflux pumps, horizontal gene transfer, and reduced influx, among others [17].

2.3.2. Impact of Antibiotics on the Environment

Plasmids play a central role in the spread of acquired resistance among bacteria found in aquatic environments contaminated with traces of antibiotics. Much of this contamination, particularly in wastewater, stems from the uncontrolled disposal of effluents linked to aquaculture and livestock farming, as well as untreated hospital waste.

Recent studies have shown that prolonged exposure to antibiotics, even at very low concentrations (in the range of ng/L to µg/L), can be enough to trigger the development of resistance genes in bacteria. One investigation [18] looked at the presence of antibiotic residues and plasmids carrying resistance genes in the Guandu and São João river basins, as well as in domestic tap water in the state of Rio de Janeiro. Researchers detected clarithromycin, sulfamethoxazole, and azithromycin in both untreated and drinking water. Using metagenomic analysis, they identified 4,881 Antibiotic Resistance Genes in Guandu, 3,705 in São João, and 3,385 in potable water, highlighting a clear link between antibiotic pollution in wastewater and the emergence of bacterial resistance mechanisms.

Aware of the scale of the problem, the scientific community has begun documenting antibiotic contamination in water bodies worldwide (see Table 1). For instance,

Baiyangdian Lake in China contains ofloxacin at 428.00 ng/L and flumequine at 2.64 ng/L, while the Hutuo River shows levels of ofloxacin at 198.00 ng/L [19]. Wastewater treatment plants, which are expected to concentrate such residues, also show alarming figures. Ciprofloxacin concentrations reached 88.01 ng/L in Durban, South Africa, and 5.52 ng/L in Madrid, Spain [19]. In Portugal, the detection rate of antibiotics in aquaculture wastewater stood at 90.3% [19]. These findings underscore the serious consequences of widespread antibiotic use in agriculture and aquaculture, as well as the limitations of current water treatment systems on a global scale.

Table 1 Concentration of major quinolone antibiotics in wastewater.

Aquatic environment	Location	[CIP], ng/L	[OFL], ng/L	[NFX], ng/L	Reference
Treatment plant (effluent)	Madrid, Spain	5524.0	365.0	-	[20]
Treatment plant (effluent)	Durban, South Africa	88.0	1578.0	89.0	[21]
Treatment plant (effluent)	Guizhou, China	489.5	328.5	229.6	[22]
Treatment plant (effluent)	North, Portugal	4.4	5.5	24.6	[23]
Treatment plant (effluent)	Dalian, China	0.0	3.2	2.8	[24]
Treatment plant (effluent)	Bohai Laizhou Bay, China	7.0	16.4	5.5	[25]

CIP: Ciprofloxacin; OFL: Ofloxacin; NFX: Norfloxacin

There is currently no universally accepted threshold for what constitutes a safe concentration of antibiotic residues in wastewater. Regulatory standards vary considerably across regions, reflecting differences in environmental policy and local ecological conditions. Within the European Union, environmental authorities employ the Environmental Risk Assessment (ERA) framework to evaluate the potential impact of chemical substances on aquatic ecosystems.

This assessment relies on a fundamental comparison between two key parameters. The first, the Predicted Environmental Concentration (PEC), estimates the level of a substance in water by taking into account its usage patterns and rate of degradation. The second, the Predicted No Effect Concentration (PNEC), defines the maximum concentration considered safe for aquatic environments, where no adverse effects are expected to occur. Biological risk is indicated when the PEC/PNEC ratio exceeds 1. In the case of quinolones, achieving a PEC/PNEC ratio below 1 requires concentrations to fall within the range of 7.0 to 80 ng/L (equivalent to 7.0×10^{-6} to 8.0×10^{-5} µg/mL) [26].

However, the data presented in Table 1 show that measured concentrations in several regions frequently exceed these thresholds. Although the situation is concerning, these findings also encourage the development of effective policies for monitoring antibiotic residues in wastewater.

These findings underscore the serious consequences of widespread antibiotic use in agriculture and aquaculture, as well as the limitations of current water treatment systems on a global scale.

2.3.3. Methods for Detecting Norfloxacin in Wastewater

The detection of antibiotics in wastewater is a well-established area of research, supported by a substantial body of literature. Traditional methods for identifying quinolones rely primarily on chromatographic techniques, such as High-Performance Liquid Chromatography (HPLC) [27]. When HPLC is coupled with Mass Spectrometry (HPLC-MS), the result is a highly sensitive “gold standard” method. One of its key advantages is the ability to analyze multiple samples simultaneously; for instance, studies have successfully detected 19 different quinolones in just four minutes [28]. However, these techniques require sophisticated instrumentation, with high costs and limited portability being among their main drawbacks.

A large portion of studies tend to avoid costly setups and methodologies, opting instead for electrochemical sensing approaches, which are more affordable, highly sensitive, and versatile. Electrochemical transduction measures the flow of electrons between the electrode surface and the electroactive species involved in redox reactions. Schematically, these reactions occur when an oxidized species accepts electrons to convert into its reduced form, as illustrated in Equation 1:

$$O + ne^- \rightleftharpoons R \qquad \text{(Equation 1)}$$

The measured current directly reflects the concentration of the electroactive species at the electrode surface. As a result, the overall reaction rate is limited by either the mass transport of the species to the electrode or the rate of electron transfer.

2.4. Biosensors - operating principle and general aspects

One of the solutions developed in response to the high costs and limited portability of gold-standard detection instruments was the emergence of ELISA-based sensors, also known as Enzyme-Linked Immunosorbent Assay (ELISA) [29]. These ELISA approaches enabled the creation of sensors with improved portability, point-of-care (POC) applicability, and more balanced costs. However, certain limitations remain, including antibody instability and the requirement for refrigeration. Even so, these sensors open the door to broader discussions around the concept of biosensors.

According to the IUPAC definition, a biosensor is a device that uses specific biochemical reactions mediated by biological elements integrated with a transducer. Its primary function is to convert a biological response into a measurable signal.

A typical biosensor is composed of integrated elements. A general schematic involves an analyte coming into contact with a bioreceptor, usually an enzyme or antibody, which binds to a transducer responsible for converting the biological recognition event into a signal. This signal is then amplified, and its magnitude is displayed through a signal output unit. Depending on the type of molecular component involved, these devices are biologically classified into three main types: immunosensors (Figure 3), aptasensors (Figure 4), and enzymatic sensors (Figure 5). Regarding immunosensors, their sensitivity and specificity depend on the affinity between the antibody and the analyte. The main transduction systems used include optical [30], electrochemical [31], and piezoelectric [32] conversions, with recent developments also enabling configurations compatible with smartphones [33]

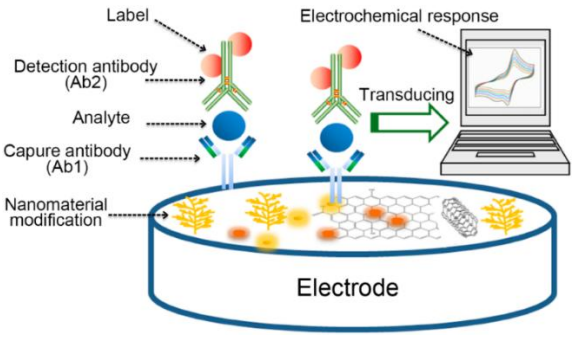

Figure 3 Illustration of an electrochemical immunosensor. Note the arrangement of antibodies on the modified electrode surface [34].

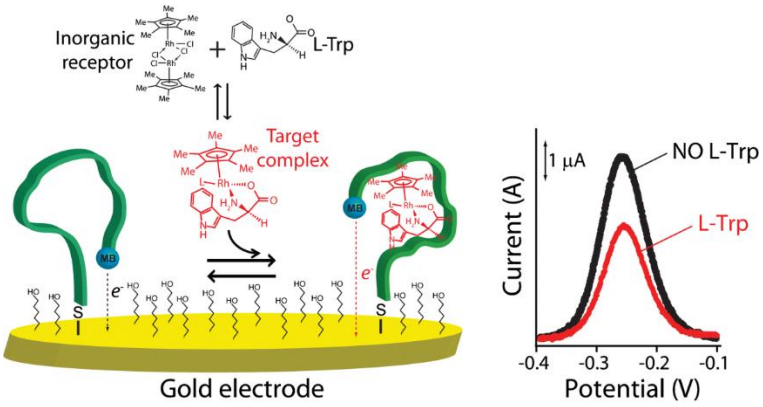

Figure 4 Schematic representation of an electrochemical sensor modified with an aptamer (left) and current readout (right) in the presence of the target analyte (NO L-Trp) [35].

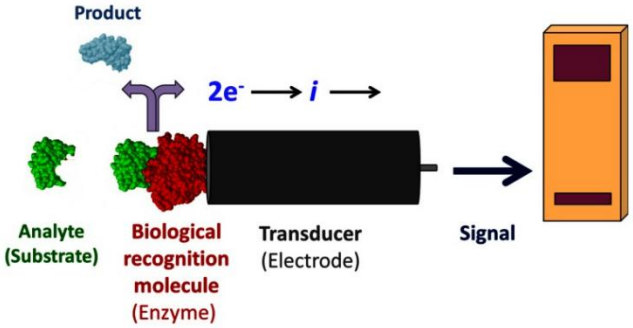

Figure 5 Schematic representation of an enzymatic electrochemical sensor. The electron flow resulting from the enzymatic redox reaction in the presence of the analyte is read by the transducer, which converts the current into an output signal [36].

Aptasensors utilize aptamers, short oligonucleotides recognized for their strong binding affinity and structural stability, which can be paired with nanoparticles or fluorescent biomolecules [37] or applied directly in electrochemical systems [38]. Enzymatic biosensors, on the other hand, rely on biochemical reactions catalyzed by enzymes with high specificity for the analyte, converting these interactions into optical [39] or electrical [40] signals.

Naturally, combining biological and non-biological elements expands the possibilities for signal transduction. For instance, integrating carbon quantum dots, graphene, or carbonized polymers with antibodies or enzymes allows researchers to harness the physical properties of these materials to enhance sensor performance. Carbon dots (CDs), in particular, are widely used in fluorescent platforms due to their photoluminescent behaviour and low toxicity, and have shown promising results in highly sensitive norfloxacin detection systems [41]. Table 2 showcases several biosensors selective for quinolones, along with a brief description of their key attributes.

Table 2 Selection of sensor examples, detailing their transduction and modification mechanisms, detection limits (LODs), and operational ranges, along with a brief comparison of their advantages relative to the conventional methods.

Method	Detection Principle	Analyte	LOD ($ng.mL^{-1}$)	Linearity ($ng.mL^{-1}$)	Advantages	Ref.
Optical – Immunosensor	Isothermal Strand Displacement Amplification	NFX	0.040	0.10 – 500.00	High sensitivity	[42]
Electrochemical – Immunosensor	Rare Earth Oxides	CIP	0.001	0.001–0.50 and 1.00–1000.00	High sensitivity	[43]
Optical – Smartphone-based System	Evanescent Wave Fluorescence Spectroscopy	NFX	15.000	5.60 – 256.80	Portable and low-cost	[44]
Piezoelectric	Magnetic Carbon Nanocomposite	CIP	2.000	5.00 – 400.00	Simplicity and speed	[45]
Optical – Fluorescence Aptasensor	Rhodamine B	OFL	0.600	7.23 – 108.41	High selectivity	[46]
Electrochemical – Aptasensor	Methylene Blue	CIP	0.033	0.10 – 149.11	Excellent sensitivity	[47]
Optical – Enzymatic Immunosensor	Paraoxonase (PO) and Lactase (Lac) Enzymes	CIP	0.003	in micrograms	Simple, but low sensitivity	[48]
Electrochemical – Enzymatic immunosensor	DNA Gyrase Immobilized on Carbon Electrode	CIP	0.500	1.00 - 10010.50	Specificity	[49]
Optical – Fluorescence	Carbon Dots (CDs)	NFX	4.247	4.25 – 6386.72	High sensitivity	[50]
Electrochemical – MIP	MIP polypyrrole–graphene–gold nanoparticles	LFX	191.540	361.40 - 36.14	high sensitivity, selectivity and reproducibility	[51]
Electrochemical – MIP	Gold nanoparticles (AuNPs) into MIP	NFX	0.150	0.32 - 31.91	Rapidity and sensitivity	[52]

CIP: Ciprofloxacin; OFL: Ofloxacin; NFX: Norfloxacin; LOD: Limit of Detection.;

2.4.1. Screen-printed electrodes

One method for fabricating electrodes for electrochemical sensors involves the use of screen printing, also known as silk-screen printing. The process itself is straightforward: specialized ink is transferred through a mesh screen, with a squeegee-like tool used to apply patterns onto flat substrates such as wood, metal, plastic, glass, and polymer. A key advantage of this approach lies in its relatively low production costs.

Conductive inks, based on materials like carbon, silver, or gold, pass through a mesh with a predefined pattern and settle onto a flat substrate, reproducing the exact design. These printed layers can reach thicknesses of up to 10 µm and resolutions of around 100 µm. The ink can be deposited in single or multiple layers and is frequently used in the fabrication of screen-printed electrodes.

After the ink passes through the mesh, it undergoes a curing process at a controlled temperature, resulting in the formation of printed electrodes. These may feature multiple working electrodes for simultaneous analysis of various analytes, or follow the conventional three-electrode layout: the Working Electrode (WE), where the reaction occurs; the Reference Electrode (RE), which maintains a stable potential to ensure precise control over the WE; and the Counter Electrode (CE), responsible for completing the circuit and allowing current to flow during the reaction.

The process, illustrated in Figure 6, offers several advantages for sensor production, including flexible design, automated batch manufacturing, high reproducibility, compatibility with various inks, ease of miniaturization, disposability, and low production costs, all of which contribute to growing interest in these electrodes.

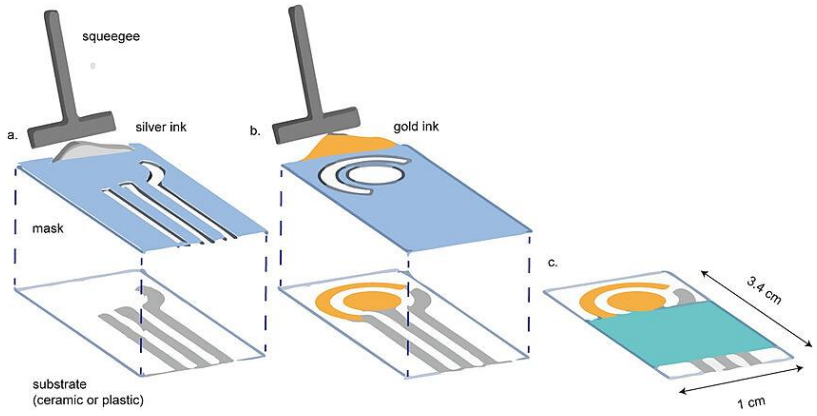

Figure 6 Illustration demonstrating the synthesis of screen-printed electrodes. In this example, conductive ink is printed onto a ceramic or plastic substrate. a) The first step involves using a stencil to print the reference electrode and contact

pads, in this case using silver ink. b) Next, a second stencil is applied to print the working and counter electrodes using gold ink. c) Finally, a hydrophobic barrier is added to cover the contact electrodes [53].

Finally, the electrochemical signal is read and made available by potentiostat devices, which must regulate the flow of current, by controlling their internal resistance, so that it passes solely between the working electrode and the counter electrode.

2.4.2. Chemically Modified Electrodes

If printed sensors show limitations in sensitivity and selectivity, one effective way to enhance both is by modifying the electrode surface. This can be achieved by incorporating materials such as nanoparticles, thin films, or organic compounds. These additions allow the sensor to detect analytes at very low concentrations and differentiate them from interfering substances. They also help reduce transduction time. Such modifications are frequently reported in the literature [54], with graphene [55], multi-walled carbon nanotube films (MWCNT) [56], and PEDOTs [57] being among the most commonly used, as illustrated in Figure 7.

Beyond direct application, polymer matrices can be engineered to create binding sites, cavities shaped specifically for the target analyte. In these cases, molecular imprinting (MIP) is the technique used to achieve this structural customization. Among the most prominent modifiers are carbon nanotubes, cylindrical carbon structures with remarkable electronic and mechanical properties. One of the key advantages of using them lies in the increased surface area and conductivity, especially when functionalized with polymers like polyaniline or polypyrrole. Metallic nanoparticles, particularly those made of gold, platinum, and silver [57], also play a significant role in analyte transduction due to their optical, electronic, and catalytic characteristics. These nanostructures can be tailored with bioreceptors and biomarkers, making them highly suitable for biosensors that demand high sensitivity, biocompatibility, and fast functionalization.

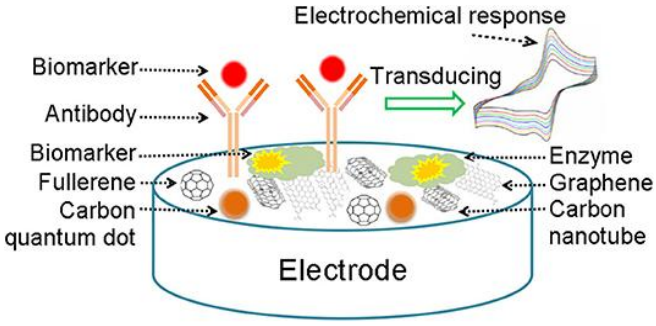

Figure 7 The diagram illustrates an electrochemical biosensor, highlighting key surface modifiers used to enhance sensitivity. Examples include modifications with graphene, carbon nanotubes, quantum dots, and carbon dots, as reported in the literature [58].

When it comes to films, graphene and its derivative, graphene oxide, stand out as two-dimensional materials with excellent electrical conductivity and a large surface area, making them ideal for electrode modification. Graphene oxide, being hydrophilic, disperses easily in aqueous solutions, which simplifies its application. Pure graphene, lacking functional groups, shows good compatibility with a wide range of compounds.

Another material worth noting is poly(3,4-ethylenedioxythiophene), also known as PEDOT. This conductive polymer has gained wide use in electrode modification thanks to its strong conductivity, chemical stability, and biocompatibility. It is often blended with other nanomaterials to create active and selective surfaces, resulting in high-performance electrochemical devices.

Beyond these, surface modification can also be tailored for selectivity. In this regard, electrochemical sensors based on molecularly imprinted polymers (MIPs), as shown in Figure 8, offer a sophisticated platform. These systems rely on the creation of specific cavities within a polymer, shaped to recognize and bind a target molecule, much like a lock and key. This design allows the sensor to pinpoint the desired substance even in complex environments.

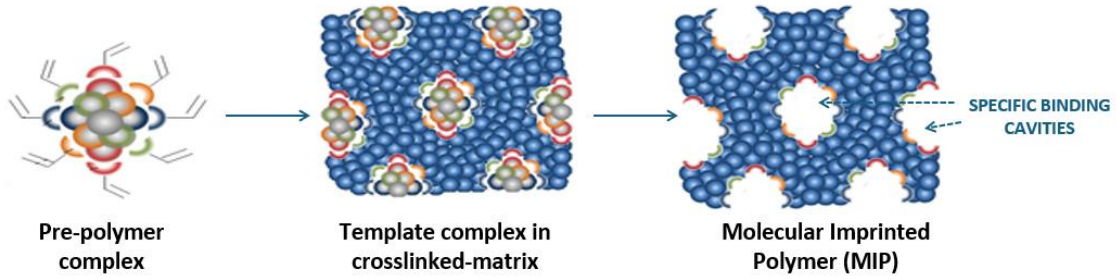

Figure 8 Schematic of Molecular Imprinting in Polymers (MIPs) assembly [59].

The target molecule leaves behind “electronic footprints” within the polymer matrix, typically fixed through electropolymerization (though other methods may also be used). Once the target molecule is removed, it leaves cavities in the matrix that are later occupied by the analyte present in the sample under analysis.

The use of MIPs in electrochemical sensors offers a favourable combination of ease of use, fast response, cost-effectiveness, and portability with high selectivity. This makes them well-suited for a wide range of applications, leading to smarter and more adaptable detection platforms.

2.4.3. Transduction Mechanisms

Current readings are most commonly visualized using cyclic voltammetry and square wave voltammetry (Figure 9). Voltammetry tracks the current at a working electrode across a defined potential range. The resulting curve reflects a combination of faradaic current, generated by redox reactions, and residual current, which arises from impurities and capacitive effects. This approach aims to establish a strong correlation between signal intensity and analyte concentration.

In cyclic voltammetry (CV) [60], the potential range is swept in both forward and reverse directions, producing curves with cathodic and anodic peaks (Figure 9, left). CV is a valuable technique for assessing thermodynamic parameters, electron transfer kinetics, and reaction reversibility. Square wave voltammetry (SWV) [60], in contrast, is known for its fast scanning and high sensitivity. It operates through a sequence of overlapping pulses, with two measurements taken per cycle. The final signal is derived from the difference between forward and reverse currents, which enhances sensitivity and makes the method particularly suitable for samples with steep concentration gradients (**Figure 9**, right).

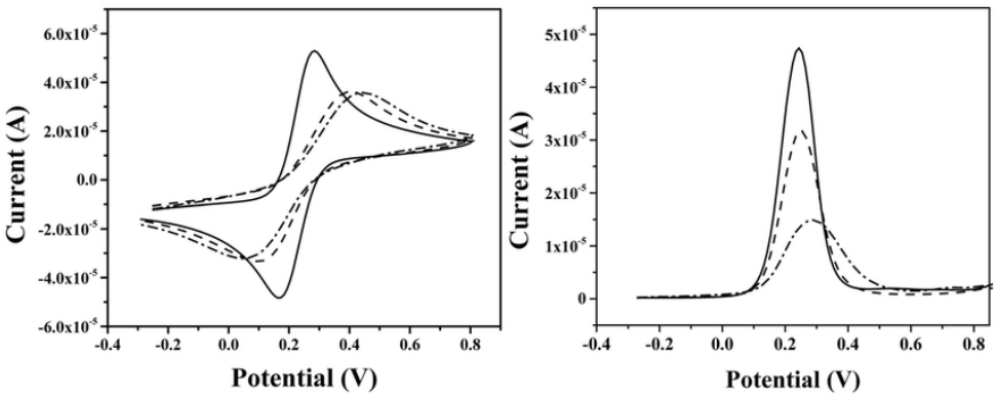

Figure 9 Diagram of cyclic voltammograms (left) and square wave voltammograms (right). Square wave voltammetry offers higher sensitivity [60].

Another important class of biosensing devices involves optical biosensors, which are based on the interaction of light with the sensor surface. Techniques include spectrometry, optical fibres, interferometry, and surface plasmon resonance, alongside optical phenomena such as absorption, fluorescence, refraction, and Raman scattering [61]. Optical detection focuses on measuring light properties, namely, amplitude, decay, polarization, phase, and energy, allowing real-time analysis and compatibility with small sample volumes.

Beyond these setups, alternative transduction mechanisms may be considered under simpler configurations and lower costs. In the case of norfloxacin, a straightforward option for qualitative detection is colorimetric methods (see Figure 10), which can be read visually or integrated with a smartphone. Iron-based reagents interact with norfloxacin molecules to form an orange-yellow complex. Optical transduction occurs through deposition of this complex onto a basic substrate, such as filter paper. Once deposited, a smartphone photograph enables RGB intensity analysis using tools such as Excel or PowerPoint [62], providing average values of primary colour components from selected image points.

These averages can be adjusted across various test solutions with differing concentrations, offering an effective qualitative and potentially quantitative approach for norfloxacin detection. Visual methods rest on the physical basis of Beer's Law [63], which defines a linear relationship between the light absorbance of a coloured material and the reagent concentration. This principle enables the quantification of norfloxacin through the RGB color intensity of the complex product.

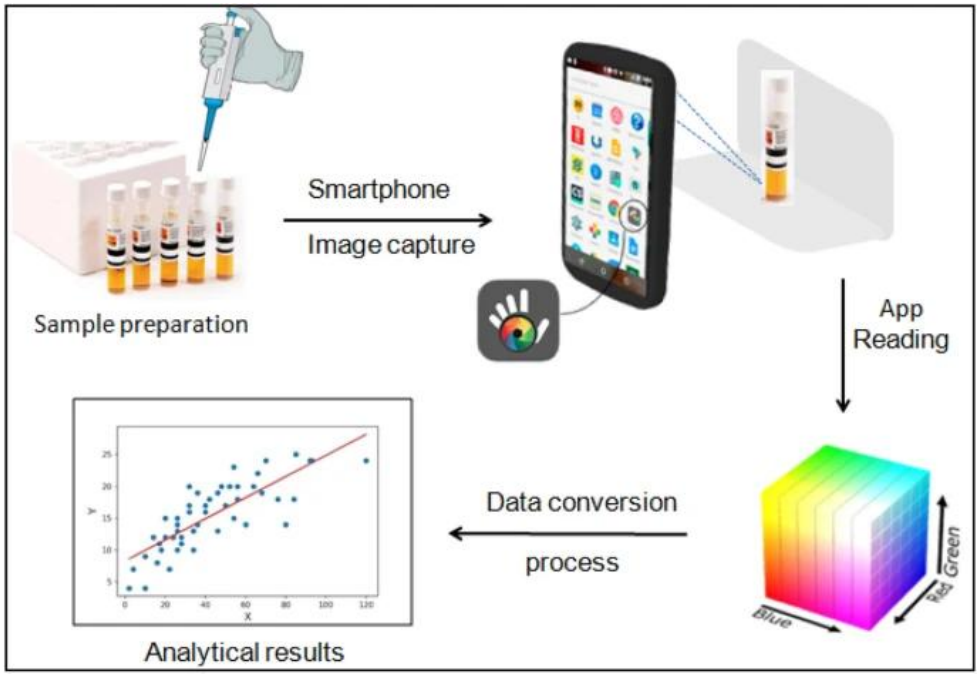

Figure 10 Smartphone-compatible colorimetric analysis. The paper-based reaction is captured using a smartphone and processed by breaking down its primary colors (RGB) [64].

A newer and promising alternative for detecting antibiotics in water is photoacoustic spectroscopy (PAS), outlined in Figure 11. The PAS mechanism relies on the photoacoustic effect, where energy from modulated light is absorbed by the specific analyte. This energy then produces pressure waves through cyclic thermal expansion

and contraction. Upon returning to its ground state, the analyte releases energy as propagating waves, detectable by microphones connected to high-performance amplification systems.

Signal amplitude corresponds proportionally to the absorbed light energy, which in turn relates to analyte concentration, along with other factors such as sound velocity and thermal expansion coefficients [65].

Adjustments in laser modulation frequency and photoacoustic cell design enhance sensitivity through acoustic resonance effects [65]. Technology holds promise for point-of-care analytical concepts, as seen in minimally invasive glucose spectroscopy applications [66].

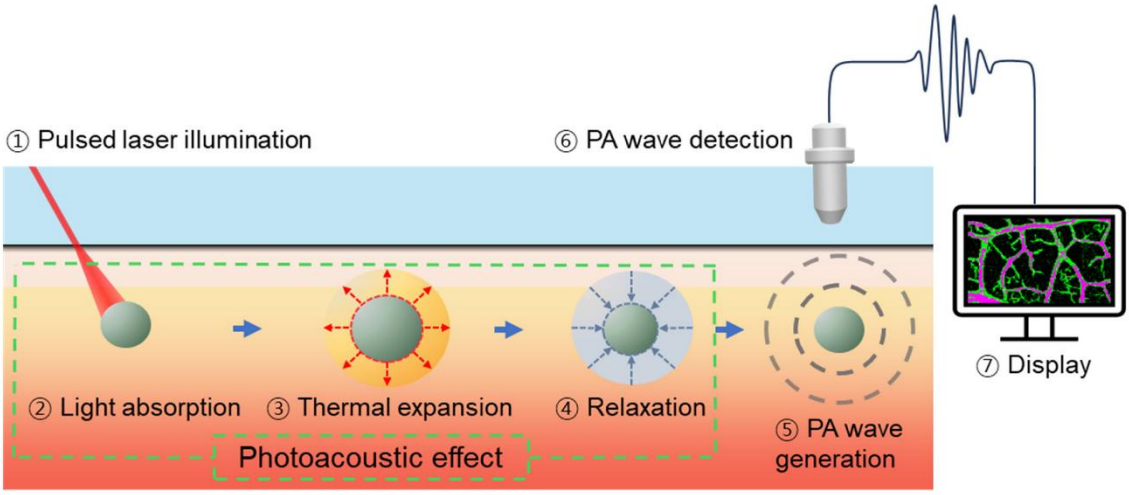

Figure 11 Schematic of photoacoustic (PA) signal generation [67].

An alternative method, defined by simplicity and efficiency, introduces magneto-osmotic sensors, as illustrated in Figure 12. The concept integrates an osmotically responsive hydrogel with a magnet attached to its surface. Signal transduction occurs through a magnetometer embedded in a smartphone, which detects magnet displacement caused by the hydrogel's swelling and contraction as solution concentrations vary [68].

The mechanism relies on osmotic potential differences. When exposed to a solution containing a specific analyte, such as glucose, the hydrogel swells if the osmotic pressure gradient of the solution is lower than that within the hydrogel. Swelling intensity increases as solution concentration decreases, due to the hydrogel's high sodium salt content. With the magnet positioned on the hydrogel surface, swelling shifts the magnet outward, depending on the dilution level of the incubating solution. This movement alters the local magnetic field, and once detected by the smartphone's magnetometer, allows correlation between magnetic field intensity and analyte concentration.

The approach reveals strong potential for low-cost biomedical assays and can be adapted for quinolone analytes, with glucose already under evaluation [68].

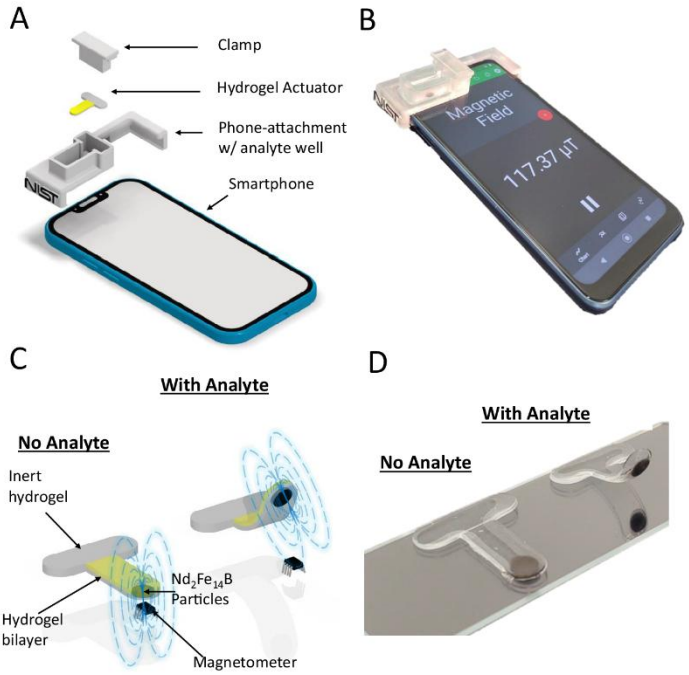

Figure 12 Design of a magnetic hydrogel-based sensor for smartphone detection: (A) Schematic of the sensor platform. (B) Smartphone application interface. (C) Detection mechanism: in the absence of the analyte, the hydrogel remains inert, and the magnetic field remains stable. When the analyte is present, the hydrogel expands or contracts, causing a shift in the magnetic field. (D) Experimental conditions: absence of analyte ("No analyte") and presence of analyte ("With analyte") [69].

2.5. Microfluidic Devices

Microfluidics enables the control and guidance of fluids through channels that are only a few micrometers wide. Working at this scale brings several advantages: it uses very little reagent, speeds up reactions and measurements, and opens the door to creating compact, portable devices. The challenge is designing these systems with sufficient precision to maximize the benefits of hydrodynamic forces. When fluid movement is well-controlled, it becomes easier to align, separate, and capture analytes with impressive sensitivity, allowing for the detection of even trace amounts. This is why this technology plays a key role in scientific research, particularly in sensing applications.

The first step in building a microfluidic device is choosing the right substrate. That choice depends on a combination of factors: the material's transparency, its biocompatibility, its ability to handle reagents, and its resistance to heat and pressure. Common options include glass, silicon, metals, polymers, and ceramics [70, 71, 72].

Among metals, aluminum and copper are popular due to their affordability, ease of machining, and resistance to heat and pressure [73, 74]. Silicon, a semimetal, is widely used in organ-on-chip systems thanks to its thermal stability, chemical compatibility, ease of fabrication, and semiconductor properties. However, it is not ideal for optical applications due to its limited transparency, especially in the visible and UV ranges [75].

Glass is a more traditional choice, often used in photolithography. It is chemically inert, stable under heat, and transparent, though its fabrication process takes longer, and its porosity can affect calibration due to volume shifts.

Polymers are another major category in microfluidics. Two of the most commonly used are polydimethylsiloxane (PDMS) and polymethylmethacrylate (PMMA) [76, 77]. PDMS is flexible, transparent, gas-permeable, and biocompatible, making it ideal for optical sensing. Still, its porous nature can be problematic with organic solvents and may lead to evaporation of analyte solutions [78].

Other polymer options include perfluorinated materials, such as Teflon (PTFE, PFA, FEP), which are thermoprocessable, chemically inert, and compatible with organic solvents. They are also transparent, moderately gas-permeable, and flexible [79]. Cyclic olefin polymers and copolymers (COPs/COCs) are also worth noting; they are transparent and chemically resistant to acids, bases, and polar solvents, with low water absorption, making them suitable for handling aggressive chemicals [80].

Two newer substrate types are gaining attention. Hydrogels, which are permeable and biocompatible, are ideal for 3D cell cultures [81]. Paper, on the other hand, is inexpensive and widely available. Its porous structure and high absorbency allow fluid to move through capillary action [82, 83], making it a strong candidate for point-of-care devices in low-resource settings.

Some devices combine different materials to get the best of both worlds. For instance, PDMS paired with glass can improve sealing and withstand high pressure [84], while PVC combined with ceramic tapes offers a low-cost solution for optical chips [85].

2.5.1. Fabrication Methods for Microfluidic Modules

A microfluidic design project must consider not only the selection of the most suitable substrate, but also the fabrication method that best matches the material of its components. Choosing the proper manufacturing technique is essential for sensor performance, as insufficient resolution or geometry can lead to poor integration between the sensor and the module, resulting in reduced sensitivity or inaccurate analyte

readings. These techniques fall broadly into two categories: mold-based approaches (such as injection micromolding and imprinting) and non-mold methods, including CNC machining, laser machining, and 3D printing.

2.5.1.1. Conventional Methods

Choosing the proper manufacturing method presents its own set of challenges, especially when attempting to match the substrate's properties with the intended design, ensuring chemical compatibility with reagents, and maintaining consistency with the chosen transduction mechanisms. In general, fabrication strategies may involve either adding or removing material, using chemical, mechanical, or laser-based techniques [86, 87, 88].

Among chemical methods, wet etching [89] and dry etching are the most commonly cited in the literature, particularly for creating channels in glass and silicon. Wet etching is a rapid process that enables the simultaneous processing of multiple plates, but it produces isotropic profiles and necessitates the use of corrosive chemicals throughout. Dry etching, also known as reactive ion etching (RIE) [90], is slower but yields more precise, anisotropic profiles. Another viable technique is electrochemical discharge machining (ECDM), which uses electrochemical sparks to remove non-conductive materials through heat or chemical reactions [91].

In the realm of mechanical processes, machining techniques are essential for working with silicon, glass, and polymers. A notable example is micromachining [92] (see Figure 13), which removes material using rotary milling tools. Other methods include water jet machining and abrasive air jet machining, both of which rely on particles to shape the workpiece.

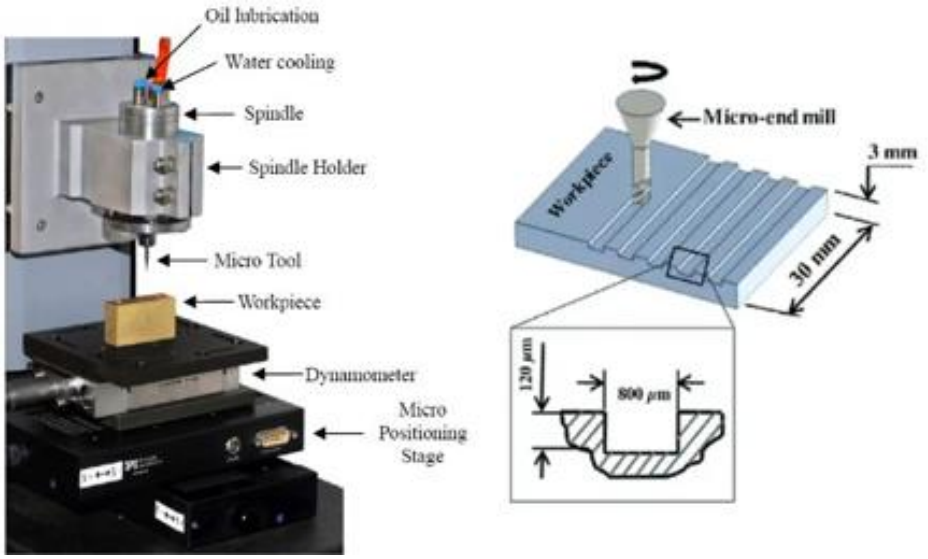

Figure 13 Photograph shows the micromachining process, specifically micromilling (left), and the result of the process on a metallic material for the creation of channels with micrometric dimensions (right) [93].

When the goal is to replicate microfluidic structures quickly and affordably, three techniques tend to be the go-to options: xurography [94], injection molding [95], and hot embossing [96] (see Figure 14). Among the most efficient methods for rapid and cost-effective replication, xurography stands out. It works by using specialized blades to cut adhesive films, enabling the quick production of microchannels without the need for costly cleanroom infrastructure. While injection molding methods [95], widely applied to thermoplastics, match xurography in speed and replicability, they sacrifice precision due to material and resolution constraints. A third method, hot embossing [96] (see Figure 14), operates on a similar principle but presses the polymer against a mold instead of injecting it.

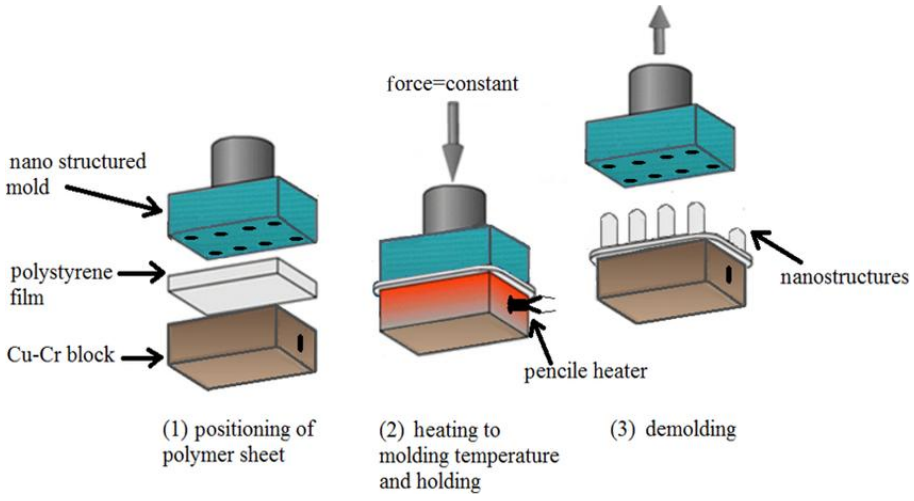

Figure 14 Diagram of the hot embossing process: placement of the polymer film (1), heating (2), and demolding (3) [97].

For optical transduction, techniques such as soft lithography, laser-based methods, and 3D printing can be employed in the design of microfluidic systems. In soft lithography [98], as shown in Figure 15, the process begins with a rigid mold. A liquid polymer (commonly PDMS elastomers) is poured over the mold, cured, and then peeled off to create the replica. Figure 15 provides further details of this procedure. However, this technique has limitations, including pattern deformation during demolding and the need for photolithography to produce the master mold, which involves cleanroom-related costs [99].

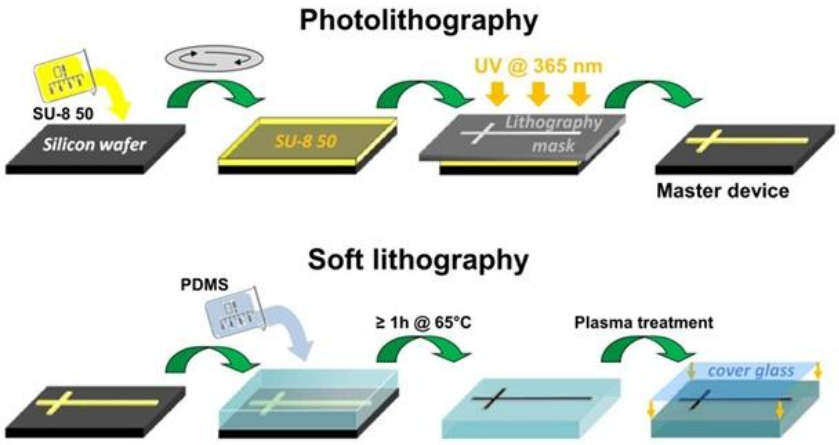

Figure 15 Fabrication of microfluidic devices combining photolithography and soft lithography [100].

The top part of the image illustrates the photolithography process. The process results in a master mold with the desired geometry, ready for use in imprinting microchannels. In the bottom part of the image, the soft lithography process is illustrated. PDMS is poured over the master mold and cured. To finalize the device, both the PDMS and a glass slide are treated with plasma, allowing them to bond and form a functional microfluidic chip.

Laser ablation processes, in turn, eliminate the need for cleanroom facilities, although the laser setup itself involves significant costs. In this technique, short laser pulses remove material by ejecting small fragments [101,102]. It is a fast and versatile method that works with a wide range of materials. In contrast to subtractive methods, stereolithography [103] represents an additive approach focused on curing rather than removing polymers. This 3D printing technique uses a laser to solidify photopolymer resins layer by layer and is particularly effective for systems requiring highly detailed designs. When ultra-high resolution is needed, two-photon polymerization (Figure 16) can be applied. This method cures the resin at specific points, voxel by voxel, offering exceptional precision, though at the cost of slower fabrication times [104].

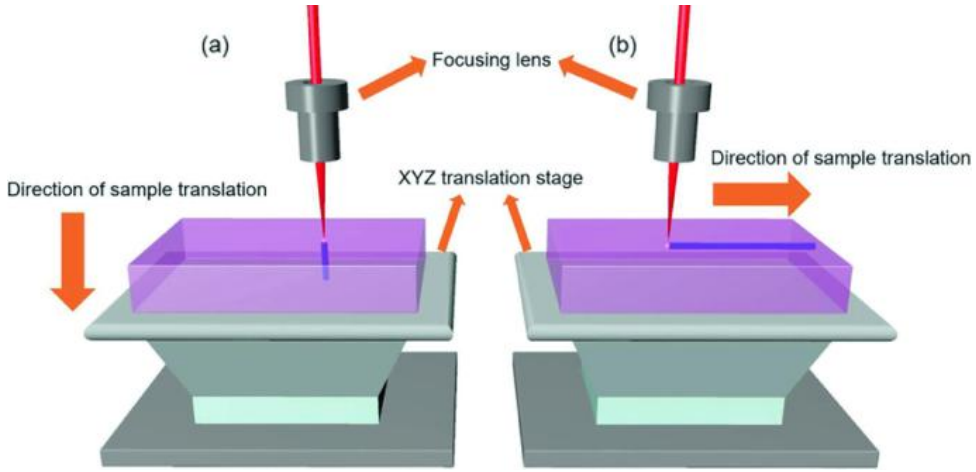

Figure 16 Two-Photon Absorption Lithography. In part (a), the laser is focused on a single point inside the material, triggering polymerization precisely at that point. Part (b) shows the laser beam being swept along a line, guided by an XYZ translation stage. The approach is able to polymerize entire lines and gradually build up complex 3D structures [105].

3D printing has become one of the most promising and effective methods for producing microfluidic channels with high precision and complexity. One of the standard techniques is fused deposition modeling (FDM), where thermoplastic filaments are extruded and melted to shape the structure. There are also methods, such as 3D printing printing (see Figure 17) and inkjet printing, which utilize photosensitive resins that are deposited and cured with great accuracy, often combining different materials in the same build [106, 107].

Just as with substrate choices, it is possible, and often beneficial, to combine fabrication techniques to overcome technical limitations and reduce costs. For example, pairing 3D printing with laser lamination allows the creation of transparent and intricate devices without relying on photolithography. This means there is no need for a cleanroom or master mask, which translates into significant savings [107].

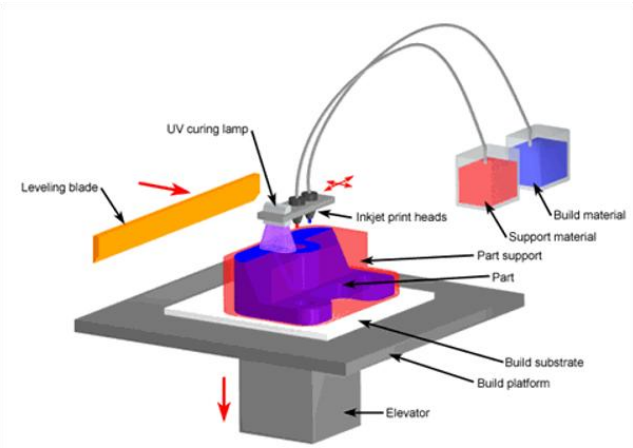

Figure 17 The image illustrates the 3D inkjet printing process used to build microfluidic structures layer by layer. A photopolymer resin is cured with UV light, while a support material is later removed. A leveling blade ensures uniform resin distribution throughout the build [108].

2.5.1.2. Alternative Methods

EWOD (electrowetting-on-dielectric) is a touchless form of digital microfluidics that manipulates tiny liquid droplets through electrowetting on a dielectric surface. In the EWOD, as illustrated in Figure 18 and Figure 19, droplets are moved across a surface containing an array of electrodes by applying electrical potentials to individual elements of the matrix. These electrodes are typically produced either by etching copper circuit boards, which are more accessible [109], or through photolithography. This method requires cleanroom conditions and, therefore, involves higher cost and complexity. The setup consists of the electrode array, a thin dielectric layer, and a hydrophobic coating [110]. One of the key advantages of this configuration is its touchless operation, which helps prevent cross-contamination.

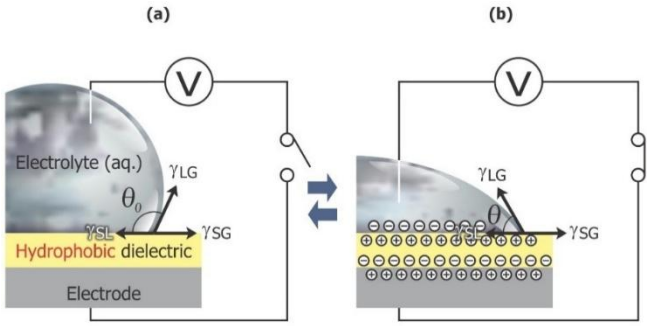

Figure 18 EWOD illustration: (a) Before applying the electric potential, and (b) After applying the electric potential [111].

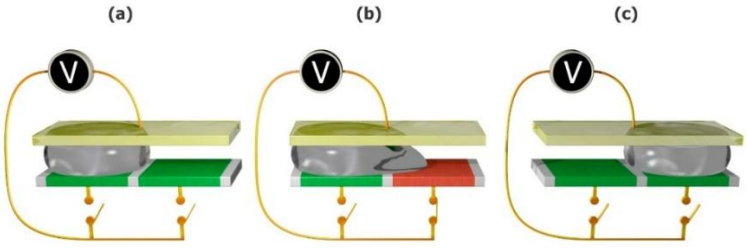

Figure 19 Movement of microliter-sized droplets using EWOD in a parallel-plate setup: (a) Both electrodes are grounded, and the droplet remains still; (b) Voltage applied to the right electrode alters the contact angle, creating a pressure gradient; and (c) The droplet moves to the right, and the electrodes are grounded again [112].

2.6 State-of-the-art conclusion

Considering technical complexity and estimated unit costs, electrochemical sensors and modules produced through additive manufacturing are viewed as the most suitable for large-scale, low-cost replicas with good sensitivity, as well as the geometric definition and flexibility required for interconnecting parts of modular microfluidic components, enabling the development of an integrated microfluidic platform.

3. Experimental Description

This chapter provides a detailed overview of the equipment, materials, reagents, and solutions used in the development of the electrochemical sensor, from electrochemical cleaning and construction of the MIP and NIP (control) to calibration of the sensors with various NFX standards in buffer and real samples, and selectivity testing. Additionally, it describes the integration and testing of the electrochemical sensor within a microfluidic device.

3.1. Equipment and Materials

Electrochemical measurements, including cyclic voltammetry (CV), square wave voltammetry (SWV), and chronoamperometry (CA), were performed using a PalmSens EmStat Pico potentiostat. This device features a printed circuit board (PCB) that enables data transfer to a computer via PSTrace software (version 5.9). The connection between the potentiostat and the electrodes was established using a PalmSens electrode reader adapter, allowing data acquisition and processing through PSTrace for subsequent analysis.

Electrode printing was carried out using a RokuPrint printer. The selected substrate was polycarbonate (PC), with a thickness of 175 µm, supplied by AGI. Electrodes were printed on the substrate in a three-component configuration: working electrodes (WE) with a diameter of 4 mm and auxiliary electrodes (CE) printed with carbon ink, and reference electrodes (RE) printed with silver/silver chloride (Ag/AgCl) ink. DuPont supplied both materials.

Characterization of electrode modifications was performed using a Fourier Transform Infrared (FTIR) spectrometer, Perkin Elmer Spectrum 100. Measurements were taken directly on the samples using the Attenuated Total Reflectance (ATR) accessory. All spectra were collected under controlled temperature and humidity conditions, representing the average of 250 consecutive acquisitions. The wavenumber range (X-axis) spanned from 650 to 4000 cm^{-1}, and the signal (Y-axis) was expressed as a percentage of transmittance. The resolution was set to 4000.

The microfluidic modules were printed using a 3D printing 3D printer, with a photopolymer material supplied by Stratasys.

3.2. Reagents and Solutions

Throughout the study, distilled water and various chemical reagents were used, including potassium ferricyanide ($K_3[Fe(CN)_6]$), anhydrous citric acid, and pyrrole (Py), obtained from Sigma Aldrich; potassium ferrocyanide trihydrate ($K_4[Fe(CN)_6]\cdot 3H_2O$, ≥98%) from Alfa Aesar; potassium chloride (KCl) from Panreac (PA-ACS-ISO); sulfuric acid (H_2SO_4, ≥95%), acetone, and glacial acetic acid supplied by Fisher Chemical; urea (99.5%) from Acros Organics; norfloxacin (NFX) from Merck; and anhydrous sodium acetate from Pronalab.

The redox pair solution $[Fe(CN)_6]^{3-/4-}$ at a concentration of 5.0 mmol/L was prepared in 0.1 mol/L KCl to ensure high ionic strength (0.18 mol/L).
For the sensor stabilization steps and the preparation of solutions used in the construction of the MIP and NIP, as well as the NFX standard solutions, a 0.2 mol/L acetate buffer solution was prepared using anhydrous sodium acetate and glacial acetic acid.

3.3. Electrode Printing by Screen-Printing

The electrode printing was carried out in the laboratory at CeNTI using the screen-printing technique (Figure 20). Carbon and silver chloride inks were selected based on their suitability for this method, particularly their ideal viscosity for the process, strong adhesion to the flexible substrate, and excellent electrochemical properties. Polycarbonate (PC) was chosen as the substrate due to its flexibility, compatibility with the selected inks, and low electrical resistivity, factors that contribute to the sensor's high performance.

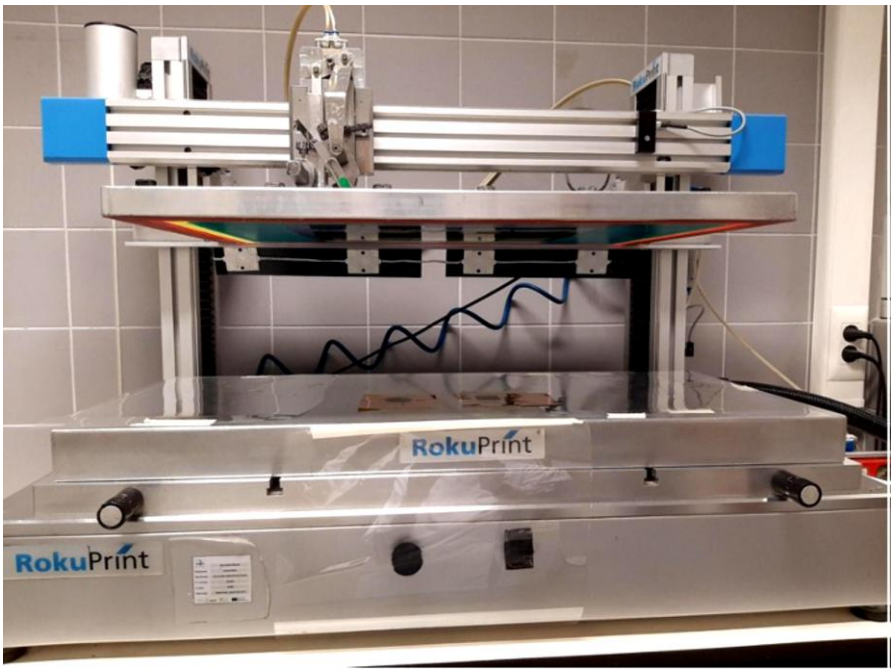

Figure 20 Screen-printing (RokuPrint).

The screen-printing process used for electrode fabrication involved several steps. Initially, the areas designated for the reference electrode (RE) were masked on the screen frame using an insulating ink, applied with a mesh suitable for precise control of ink flow and definition of the printed electrode layout (areas, spacing between electrodes, and line width). Next, carbon ink was applied in five layers to create the working (WE) and auxiliary (CE) electrodes, with drying between each layer to ensure good electrical conductivity. After printing the carbon layers, the electrodes were cured at 110 °C for 20 minutes in an oven. The next step involved cleaning the screen frame, followed by reapplication of the insulation ink, this time over the areas already printed with carbon ink. With the WE and CE areas properly protected, silver/silver chloride (Ag/AgCl) ink was applied in two passes to print the reference electrode (RE), which was then cured at 110 °C for 30 minutes in an oven. Finally, a dielectric ink was applied over the contact areas to ensure electrical insulation and protect the connections, followed by curing at 110 °C for 40 minutes. Figure 21 illustrates the various stages of the electrode printing process described above, as well as the overall layout of the electrodes (CE/WE/RE), based on the geometry proposed by Tavares et al. [113].

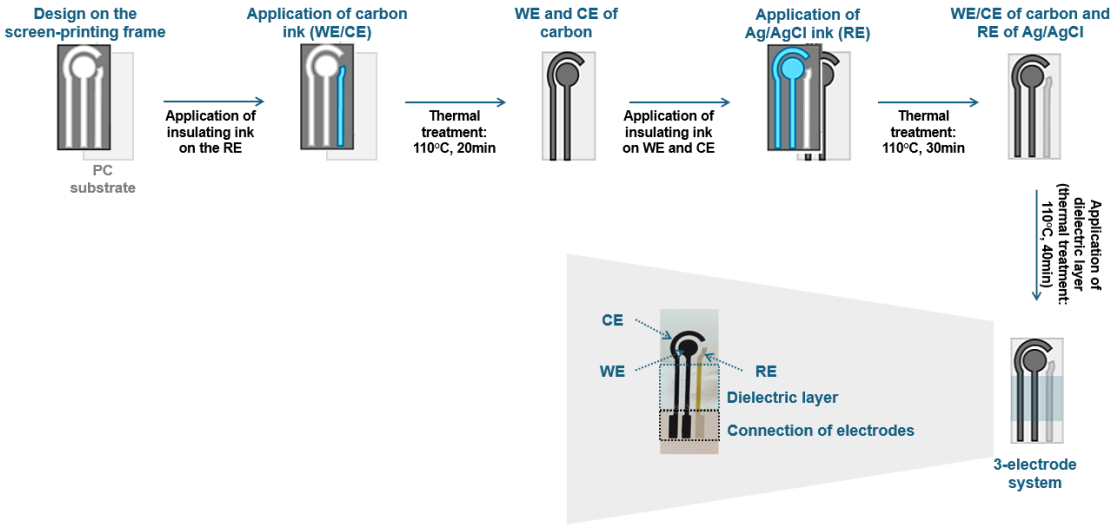

Figure 21 Schematic representation of the electrode printing process using the screen-printing technique and illustration of the final three-electrode system obtained. In blue is the part that is obstructed (blocked) during the screen printing process. In white are the electrode components that will be printed by screen printing

3.4. Preparation of Electrochemical Sensors

To ensure accurate and reproducible electrochemical measurements, preliminary preparation steps were performed on the working electrodes (WEs) before constructing the MIP and NIP sensors. A key part of this process was the electrochemical cleaning step, which aimed to remove impurities from the carbon WE surface and promote its functionalization. Additionally, the surface of the WE was modified with carbon dots (CDs) to increase the electrode's surface area and, consequently, enhance the sensor's response.

3.4.1. Electrochemical Cleaning of the WE

Although mechanical cleaning methods for electrodes exist, this study adopted electrochemical cleaning as the standard procedure, applied to all electrodes before any modification. Cleaning was performed using cyclic voltammetry within a potential range of -0.2 V to +1.8 V in an aqueous solution of 0.5 mol/L H_2SO_4. This procedure not only removed surface impurities from the carbon but also promoted the formation of functional groups, specifically hydroxyl (-OH) and carboxyl (-COOH) groups, on the WE surface, facilitating the binding of the monomer and the target molecule [114]. Based on previous studies conducted at CeNTI and supported by literature, a scan rate of 0.050 V/s was selected for a total of 30 cycles. To evaluate the effect of electrochemical cleaning on

the WE surface, an indirect analysis was performed before and after the cleaning process using the redox solution $[Fe(CN)_6]^{3-/4-}$, aiming to identify changes on the WE surface. This analysis was also conducted using cyclic voltammetry, with 10 consecutive cycles at a scan rate of 0.025 V/s and a potential range of -0.8 V to 1.0 V. The results, presented in **Appendix A1. Electrochemical Cleaning**, confirm that the adopted cleaning procedure contributes to sensor optimization.

3.4.2. Modification of the WE Surface with CDs

The synthesis of carbon dots (CDs) was carried out according to the protocol described by Zhang et al., in 2022 [107]. The process involved combining 2 g of citric acid and 4 g of urea in 20 mL of acetone under solvothermal conditions at 160°C for 4 hours. This is a low-cost, low-toxicity, and biocompatible approach, suitable for producing CDs with fluorescent properties. In addition to their optical characteristics, these nanomaterials exhibit excellent electrochemical properties, notably increasing the surface area of the working electrode (WE), which promotes the formation of multiple active sites available for electrochemical reactions.

To modify the WE, 30 µL of the synthesized CD solution was applied to the surface of the electrochemically cleaned WE and incubated at 60 °C in an oven for 60 minutes. After the incubation period, an indirect analysis was performed using the redox solution $[Fe(CN)_6]^{3-/4-}$ under the previously mentioned conditions (CV: -0.8 V to 1.0 V; 10 consecutive cycles; 0.025 V/s). **Appendix A2. Carbon Dots (CDs)** contain the results of the nanomaterial characterization (**Appendix A2.1. Characterization of CDs**), using fluorescence techniques, as well as the results of the WE surface modification (**Appendix A2.2. Modification of the WE with CDs**). Following this electrode surface modification, the construction of the sensors (MIP and NIP) was carried out.

3.5. Preparation of the Molecularly Imprinted Polymer (MIP) for NFX Detection

After the cleaning of the working electrodes (WEs), the preparation of the molecularly imprinted polymer (MIP) was carried out, a crucial step to impart selectivity to the sensor developed for NFX detection. To achieve this selectivity, MIP technology was employed, which uses conductive polymers to form the recognition matrix. One of the main challenges of this approach lies in signal transduction, particularly in establishing an efficient connection between the recognition element and the analytical signal, which requires conductive polymers with strong electrochemical properties.

In this context, and based on previous studies conducted at CeNTI, pyrrole (Py) was selected as the monomer for creating the polymeric matrix. This choice was based on its high electrical conductivity, chemical stability, ease of electrochemical polymerization, compatibility with biological molecules and other analytes, and its ability to provide selectivity to the system.

The MIP was prepared by electropolymerizing the Py monomer in the presence of the target molecule, NFX, allowing the formation of a selective polymeric matrix directly on the surface of the carbon WE. This process, in addition to being simple and fast, enables precise control over the growth of the polymeric matrix on the electrode surface.

Electropolymerization was carried out using a solution of Py and NFX prepared in acetate buffer (pH 3-4). The technique used was chronoamperometry (CA), performed at a potential of 0.8 V for different durations, including 30, 60, and 90 seconds. To determine the ideal potential for this technique, preliminary cyclic voltammetry (CV) studies were conducted on the individual compounds using two solutions: 2.0 mmol/L Py and 7.5 mmol/L NFX in acetate buffer at pH 3-4. The CV conditions involved three consecutive cycles at 0.050 V/s, within a potential range of -0.4 V to 1.6 V. Analysis of the results showed that Py undergoes electropolymerization at 0.8 V, while NFX does not exhibit electroactivity. Based on this behavior, 0.8 V was selected as the optimal potential for electropolymerization, ensuring efficient formation of the Py polymeric matrix without interference from NFX.

Once the ideal potential was defined, electropolymerization via chronoamperometry was performed using a solution containing 2.0 mmol/L Py and 7.5 mmol/L NFX in acetate buffer (pH 3-4). Additionally, different concentration combinations of the target molecule (NFX) and the monomer (Py) were tested to determine the most suitable ratio for forming a selective and efficient matrix.

3.6. Preparation of the Non-Imprinted Polymer (NIP)

In parallel with the construction of the MIP, a control sensor was prepared by synthesizing a non-imprinted polymer (NIP). The NIP was produced under the same conditions used for the MIP, except that the target molecule (NFX) was absent from the electropolymerization solution. Instead, a solution containing 2.0 mmol/L of pyrrole (Py) in acetate buffer at pH between 3 and 4 was used. The electropolymerization procedure followed the same protocol as that applied in the preparation of the MIP.

3.7. Sensor Performance

To evaluate the performance of each prepared sensor (MIP and NIP), they were subjected to a three-step experimental protocol: stabilization, NFX incubation, and electrochemical measurement.

3.7.1. Sensor Stabilization

For this step, 30 µL of acetate buffer (pH 3-4) was incubated on the working electrode (WE) for 60 minutes, with measurements taken every 30 minutes. After each incubation period, an indirect analysis was performed using the redox solution $[Fe(CN)_6]^{3-/4-}$, applying the square wave voltammetry (SWV) technique under the following conditions: frequency of 1.0 Hz, amplitude of 0.1 V, and a potential range from -0.2 V to 0.6 V. The optimal incubation time with the acetate buffer selected for an efficient sensor stabilization was 60 minutes.

3.7.2. NFX Incubation and Electrochemical Characterization

Standard NFX solutions were prepared across a range of increasing concentrations, from 0.005 pg/mL to 5.00 µg/mL. For each concentration, 30 µL of the standard solution was incubated on the surface of the working electrode (WE), in ascending order, for 30 minutes. Following each incubation step, an indirect analysis was performed using the redox solution $[Fe(CN)_6]^{3-/4-}$, applying the square wave voltammetry (SWV) technique with the following parameters: frequency of 1.0 Hz, amplitude of 0.1 V, and a potential range from -0.2 V to 0.6 V. After completing the measurement, the next standard solution was incubated on the same electrode surface. This sequential concentration accumulation approach on a single sensor was adopted to minimize experimental errors associated with the variability of printed electrodes, which may exhibit inconsistencies inherent to the printing process.

4. Results and Discussion

This chapter addresses the binding of the antibiotic NFX during sensor preparation and evaluates its performance. It also includes an analysis of the modified electrode surfaces and their performance in real water samples. Additionally, the integration of these electrochemical sensors into a microfluidic module will be presented.

4.1. Sensor Material Preparation: MIP and NIP

For the preparation of the sensor material, both MIP and NIP (control), the following steps were undertaken: (i) a study of the electropolymerization and NFX removal conditions, aimed at optimizing the electropolymerization process to achieve a sensor with high sensitivity, while ensuring the efficient removal of residual monomers or non-polymerized analyte from the surface of the working electrode (WE); (ii) an investigation into the NFX:Py concentration ratios for the electropolymerization process, to determine the optimal condition for obtaining a sensor with high sensitivity and selectivity toward NFX; and (iii) modification of the WE with carbon dots (CDs), to evaluate the impact of this modification on the overall performance of the sensor.

4.1.1. Study of Electropolymerization and NFX Removal Conditions in MIP and NIP

After selecting the potential of 0.8 V for the electropolymerization of the 7.5 mmol/L NFX:2.0 mmol/L Py solution via chronoamperometry, it was necessary to optimize the assay duration, as shown in Graph 1. To determine the best condition for analyte (NFX) immobilization, three electropolymerization times were evaluated: 30, 60, and 90 seconds. These tests were conducted cumulatively.

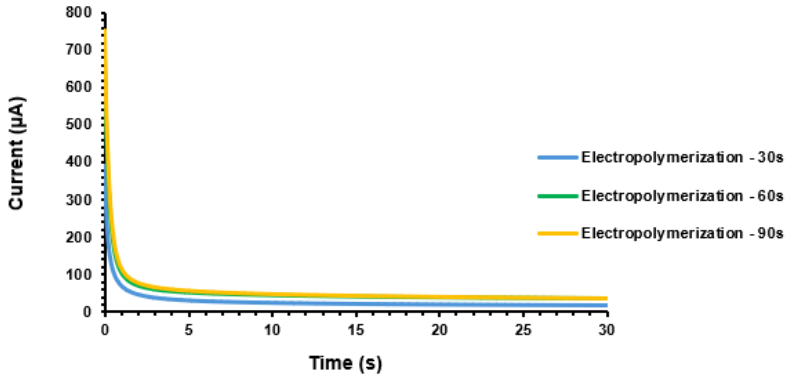

Graph 1 Representation of Current vs. Time Curves from the NFX:Py Electropolymerization Assays Performed by Chronoamperometry (cumulative trials).

During the definition of the electropolymerization parameters, the study showed that variations in the concentrations of NFX and Py in the solution, as well as the choice of electropolymerization time, resulted in different levels of sensor sensitivity. In general, it was observed that the longer the polymerization time, the greater the sensor's sensitivity, as indicated by an increase in current values. After each electropolymerization step, indirect measurements were performed using cyclic voltammetry (CV) with the redox solution $[Fe(CN)_6]^{3-/4-}$. Graph 2 displays the voltammograms obtained after each electropolymerization stage (30, 60, and 90 seconds).

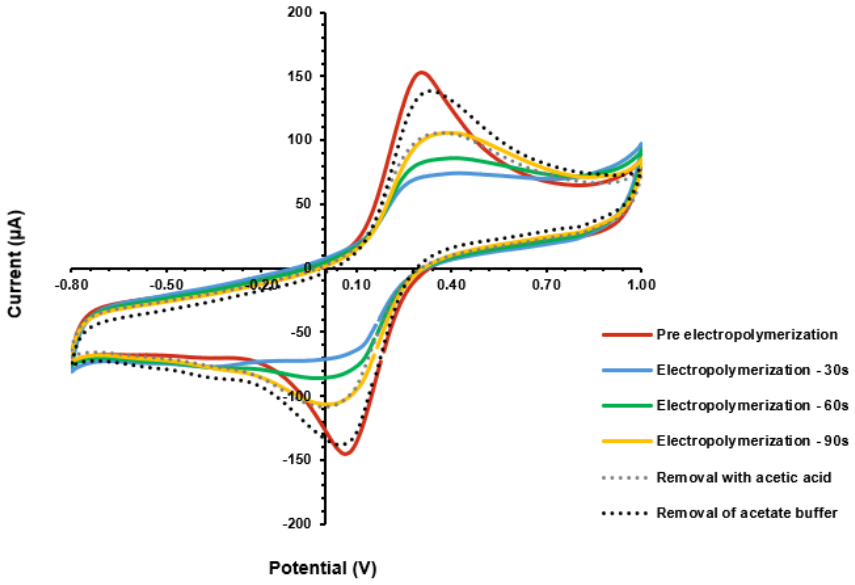

Graph 2 Voltammograms of the Different Stages in the MIP Construction Process.

Analysis of the voltammograms reveals that longer polymerization times lead to a more pronounced modification of the sensor surface, with this change being most evident at 90 seconds. This suggests greater formation of NFX-selective pores under these conditions. When comparing this condition to the sensor after electrochemical cleaning, a clear modification is observed, reflected in the decrease in current of the redox peaks and an increase in the potential difference between the peaks, with ΔE shifting from 0.25 V to approximately 0.36 V.

Once the optimal electropolymerization condition was established, NFX removal from the polymer matrix was performed. Initially, a 0.2 mol/L acetic acid solution was used, with 30 µL applied to incubate the working electrode (WE) for 90 minutes. At the end of the incubation period, measurements were taken using the redox solution $[Fe(CN)_6]^{3-/4-}$, which indicated that this step had no significant impact on the WE, as the voltammogram obtained after removal overlapped with the one from the 90-second

electropolymerization stage. Consequently, a second NFX removal procedure was adopted, involving 15 consecutive cycles at a scan rate of 0.050 V/s within a potential range of -0.5 V to 1.0 V, using an acetate buffer solution (pH 3-4). This approach proved more effective, as evidenced by a significant increase in current and a reduction in the potential separation between the redox peaks ($\Delta E \approx 0.28$ V). This procedure not only facilitated the removal of residual monomers or analytes that had not undergone electropolymerization on the WE surface but also supported the subsequent sensor stabilization step.

The same procedure was applied to the control sensor (NIP), in which electropolymerization was performed using only 2.0 mmol/L Py, without the target molecule (NFX), under the same operating conditions. Graph 3 shows the voltammograms obtained after each electropolymerization stage (30, 60, and 90 seconds).

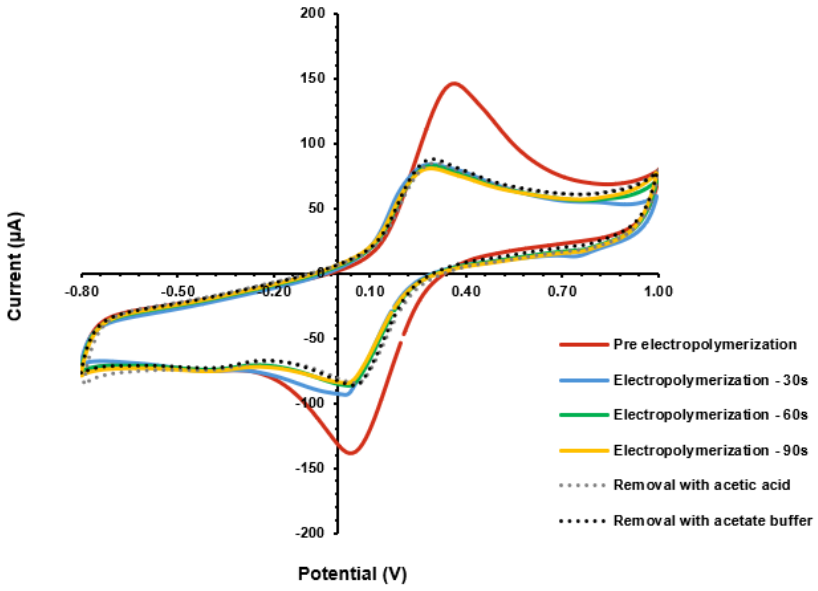

Graph 3 Voltammograms of the Different Stages in the NIP Construction Process.

Analysis of the voltammograms reveals that, similar to the behaviour observed in the MIP, longer polymerization times (60 s and 90 s) lead to greater modification of the sensor surface, as evidenced by the decrease in current at the redox peaks. During the removal processes with acetic acid (initial phase) and acetate buffer (pH 3-4) (subsequent phase), no significant changes were observed on the electrode surface. This behaviour was expected, given that the polymeric matrix did not contain NFX to be removed.

4.1.2. Study of NFX:Py Concentrations for the Electropolymerization Process

Regarding the concentration of the electropolymerization solution, an initial exploratory study was conducted using three different concentrations of NFX and Py, combined in pairs. The objective was to determine which NFX and Py concentration combinations could provide the best linear fit during calibration within a previously tested range (0.005–50 µg/mL). The tested NFX:Py concentration combinations are listed in Table 3 and the corresponding calibration results are presented in Table 4. Using an experimental design with ANOVA made the analysis more robust. The results showed that both NFX and Py concentrations significantly influenced the sensor's linearity (R^2) at $p < 0.05$, not because one dominated, but because they interacted strongly. In practice, the effect of Py on R^2 shifts depending on the amount of NFX in the solution. This means that optimizing the sensor isn't about adjusting each component on its own — it requires tuning both together.

Table 3 Representation of the NFX:Py concentration combinations studied.

Electropolymerization solutions	NFX 2.5 mmol/L	NFX 5.0 mmol/L	NFX 7.5 mmol/L
Py 1.5 mmol/L	Solution 1	Solution 2	Solution 3
Py 2.0 mmol/L	Solution 4	Solution 5	Solution 6
Py 2.5 mmol/L	Solution 7	Solution 8	Solution 9

Table 4 Results obtained from the calibration of different electropolymerization solutions.

Test solutions of MIP	Slope (µA/µg.mL^{-1})	Coefficient of Determination
Solution 1	9.071	0.30
Solution 2	6.712	0.24
Solution 3	1.119	0.38
Solution 4	1.632	0.64
Solution 5	3.220	0.70
Solution 6	4.235	0.99
Solution 7	3.927	0.99
Solution 8	3.239	0.98
Solution 9	2.275	0.85

After selecting the three NFX:Py concentration combinations that showed the most promising results for lower NFX concentration levels (solutions 6, 7, and 8), calibrations were repeated across a broader range of NFX concentrations (0.005 to 50 µg/mL). From this study, it was concluded that the most promising NFX:Py concentration combination for detecting low NFX levels, close to ng/L in wastewater, is 7.5 mmol/L NFX and 2.0 mmol/L Py. Graph 4 presents the calibration curve for the MIP constructed under this electropolymerization solution condition, followed by the molecule removal processes described earlier (section 4.1.1). This figure also includes the fitting matrix of the resulting calibration curve.

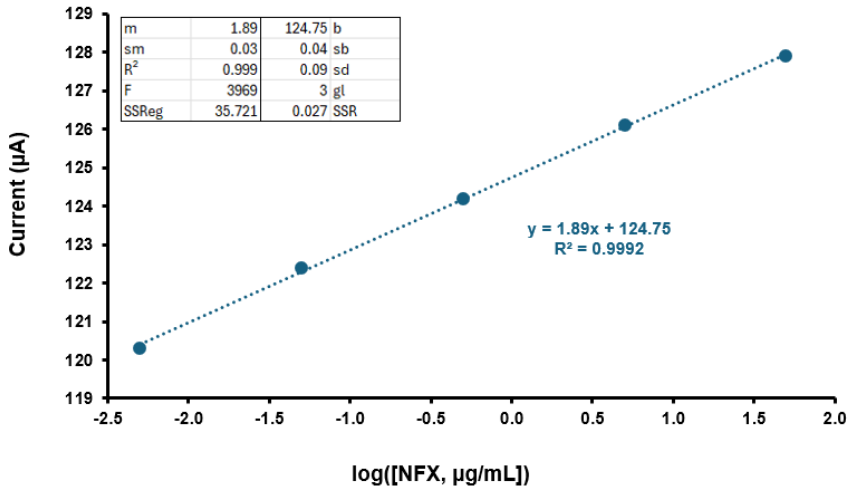

Graph 4 Graphical representation of the calibration of the MIP constructed using the electropolymerization solution containing 7.5 mmol/L NFX and 2.0 mmol/L Py (solution 6). Linear fit of the calibration curve is shown within the concentration range of 0.005 to 50 µg/mL

Based on the results obtained, the MIP prepared under electropolymerization conditions of 7.5 mmol/L NFX and 2.0 mmol/L Py exhibited linear behaviour within the concentration range of 0.005 to 50 µg/mL, with a determination coefficient of 0.9992, indicating a strong linear relationship between the analyte concentration and the sensor response.

4.1.3. Modification of the Working Electrode (WE) with Carbon Dots (CDs)

As previously mentioned, this study included a parallel investigation into modifying the working electrode (WE), aiming to assess improvements in the sensor's electrochemical properties. Notably, the increase in the WE's surface area was highlighted, as it promotes the formation of multiple active sites available for electrochemical reactions.

Following the results presented in **Appendix A2: Carbon Dots (CDs)**, the construction of the sensors (MIP and NIP) was carried out according to the conditions described in

earlier sections. For their calibration, various standard NFX solutions were prepared within a concentration range from 5.0×10^{-19} to 25.0 µg/mL.

Graph 5 displays the calibration curves of the MIP and NIP sensors built on CD-modified WEs (1-hour incubation), corresponding to concentration ranges of 5.0×10^{-19} – 2.5×10^{-5} µg/mL and 5.0×10^{-9} – 25.0 µg/mL, respectively.

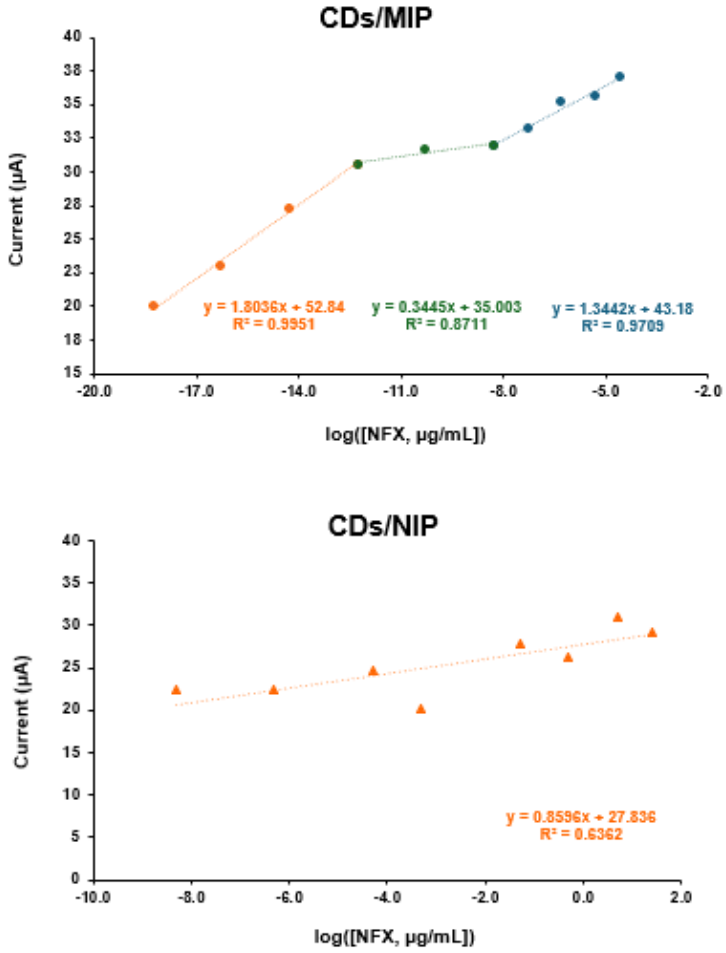

Graph 5 Graphical representation of the calibration curves for MIP and NIP sensors built on CD-modified WEs (1-hour incubation).

After incubating the sensor modified with CDs for one hour at 60°C, a distinct analytical behaviour was observed across three segments, reflecting different response regimes to NFX concentration.

The first segment (5.0×10^{-19} – 5.0×10^{-13} µg/mL), at low concentrations (orange points), stood out for its high sensitivity, with a slope of 1.804 and strong linearity ($R^2 = 0.9951$), indicating a strong and efficient initial interaction with the sensor surface.

At intermediate concentrations (5.0×10^{-13} – 5.0×10^{-9} µg/mL, orange points), sensitivity decreased, as shown by a lower slope of 0.345 and moderate linearity (R^2 = 0.8711), possibly due to saturation of binding sites or the formation of layers that interfere with interaction. However, at higher concentrations (5.0×10^{-9} – 2.5×10^{-5} µg/mL, blue points), the slope increased again to 1.344, maintaining good linearity (R^2 = 0.9709), suggesting a modified interaction regime that still allows robust detection even with greater analyte abundance.

The segmentation of the calibration curve into multiple regions somewhat compromises the interpretability and quantitative applicability of this sensor in wastewater analysis.

In contrast, results from sensors without CD modification showed good linearity across the entire concentration range analysed. Achieving a single linear fit over a wide range is desirable for calibration curves, as it ensures a predictable and consistent sensor response to variations in analyte concentration, making it preferable for NFX calibration assays in buffer. Nevertheless, it is worth noting that CD-modified sensors exhibited greater sensitivity at low NFX concentrations, with potential applicability in approaches requiring detection at fg/mL levels (such as devices for healthcare applications).

4.2. Evaluation of Sensor Performance

4.2.1. Stabilization Process

Following the electropolymerization processes and the efficient removal of the target molecule (NFX), sensor stabilization was carried out, an essential step for optimizing the sensor's analytical signal. Graph 6 illustrates the voltammograms of readings in the redox solution $[Fe(CN)_6]^{3-/4-}$, taken after NFX removal in acetate buffer (pH 3–4) and after sensor stabilization in acetate buffer following 30 and 60 minutes of incubation. These measurements were performed successively using square wave voltammetry.

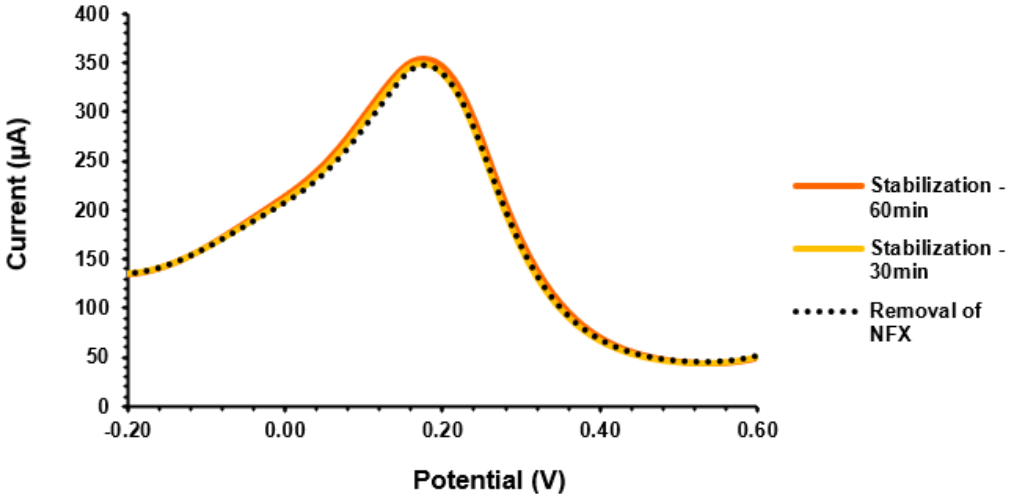

Graph 6 Voltammograms of readings in the redox solution $[Fe(CN)_6]^{3-/4-}$, following the removal of NFX in acetate buffer (pH 3–4) and subsequent sensor stabilization in acetate buffer after 30 and 60 minutes of incubation. Measurements were obtained using square wave voltammetry.

Based on the results obtained, it was observed that after 30 and 60 minutes of incubation in acetate buffer, the analytical signal did not exhibit significant changes compared to the removal stage, specifically, no notable variations in current or potential of the redox peaks were observed that would affect the sensor's sensitivity. Therefore, to ensure proper sensor stabilization, a 60-minute incubation in acetate buffer was selected for the stabilization process. As a result, the sensor is stable and ready to be calibrated with various standard NFX solutions.

4.2.2. Sensor Calibration in Acetate Buffer

After completing the sensor stabilization step in acetate buffer solution, square wave voltammetry was employed for indirect measurement using the redox pair $[Fe(CN)_6]^{3-/4-}$, due to its high sensitivity and suitability for this type of application. These analyses were conducted under a frequency of 1.0 Hz, an amplitude of 0.1 V, and a potential range from -0.2 V to 0.6 V.

For the calibration of MIP and NIP, standard NFX solutions were prepared across a broader concentration range, targeting low levels, specifically from 0.005 pg/mL to 5.00 µg/mL. These solutions were incubated on the sensors in increasing order for over 30 minutes. Graph 7 presents the voltammograms obtained from the calibration of both MIP and NIP within the selected concentration range.

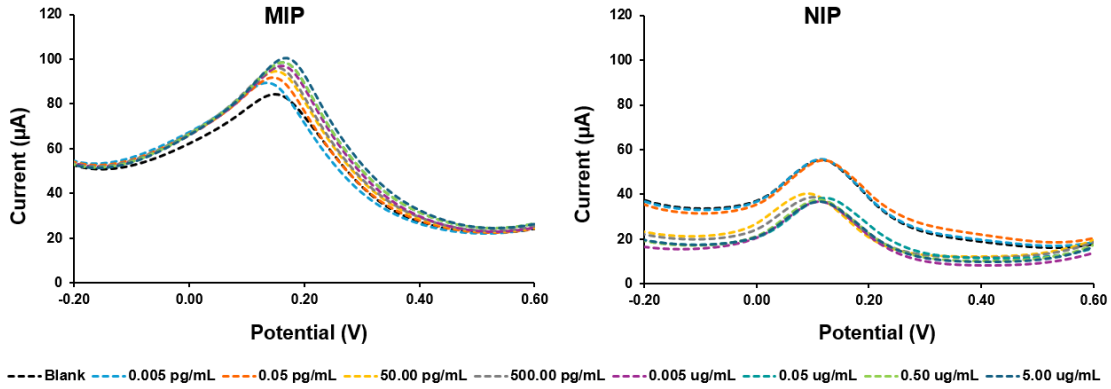

Graph 7 Representative voltammograms from the calibrations of MIP and NIP using standard NFX solutions at varying concentrations.

From the voltammograms obtained, a rising trend in the current peaks of the MIP was observed as the concentrations of the standard NFX solutions increased. In contrast, the NIP did not show the same pattern, with random variations in the signals recorded for the different NFX concentrations prepared in buffer. This behaviour aligns with expectations, as the NIP serves as a control sensor and lacks specific cavities for NFX detection.

After acquiring the voltammograms for each standard NFX solution prepared in acetate buffer (pH 3-4), calibration curves were constructed as shown in Graph 8. The sensor's response to varying NFX concentrations was evaluated based on the linear fit between the logarithm of NFX concentrations and the height of the current peak obtained at approximately 0.15 V, a characteristic peak of the redox solution $[Fe(CN)_6]^{3-/4-}$.

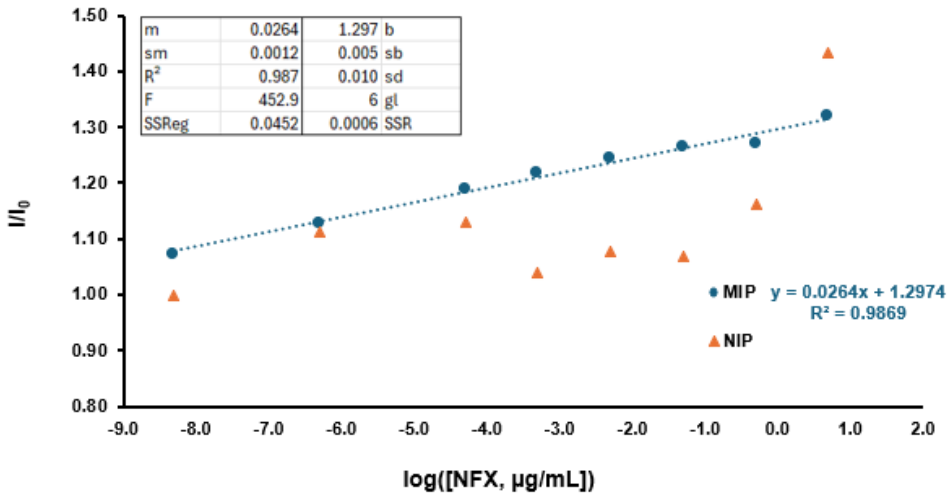

Graph 8 Representation of the linear fit obtained from the calibration of MIP and NIP within the NFX concentration range of 0.005 pg/mL to 5.00 µg/mL, using acetate buffer (pH 3-4).

The calibration curve results represent the average of three replicates. The sensor's response linearity was confirmed by the determination coefficient (R^2), which exceeded

0.98 for the MIP, indicating a strong linear correlation between analyte concentration and sensor response. This suggests that the sensor performs consistently, providing accurate measurements. Additionally, in line with IUPAC recommendations [115], two analytical parameters were determined: the limit of detection (LOD) and the limit of quantification (LOQ), both set at 0.005 pg/mL. The average relative standard deviation (RSD) was around 8%. In contrast, the NIP showed random behaviour, with a determination coefficient of approximately 0.41 and a higher average RSD of 13%, confirming the lack of selectivity and sensitivity typical of non-imprinted materials.

Overall, the developed sensors demonstrated high sensitivity, capable of detecting NFX levels below those reported in the literature (e.g., 0.015 µg/mL) [116], as also shown in Table 2.

4.2.3. Repeatability

Regarding repeatability, a MIP sensor was tested across a concentration range of 0.005 pg/mL to 50.00 µg/mL through successive measurements in the redox solution $[Fe(CN)_6]^{3-/4-}$, aiming to assess its ability to reproduce results consistently. This evaluation is illustrated by the calibration curves shown in Graph 9.

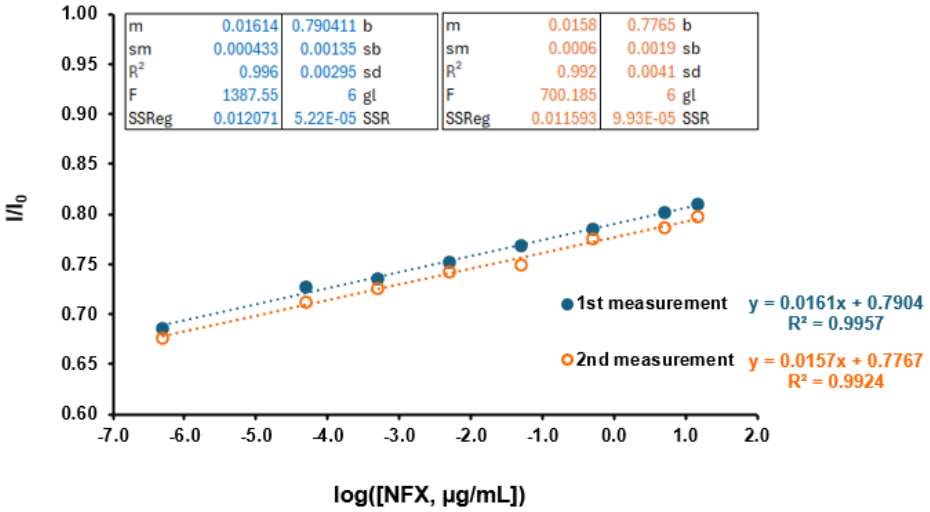

Graph 9 Repeatability study of successive measurements after incubations with varying concentrations of NFX.

According to the results obtained, the sensor showed a consistent response across successive measurements, with a slope of 0.016 and high linearity ($R^2 > 0.99$) in both cases. The average relative standard deviation (RSD) was approximately 1.6%, indicating good repeatability and measurement consistency.

4.2.4. Sensor Recovery

For the sensor recovery study, MIP was used to evaluate the possibility of reusing the sensors by removing as much of the NFX analyte as possible. All modifications made to

the MIP were assessed through indirect analysis using the redox pair solution $[Fe(CN)_6]^{3-/4-}$. Before calibration, this procedure was repeated several times to ensure the complete or partial removal of NFX, following the previously described removal methods. The MIP was then calibrated using various standard NFX solutions prepared in acetate buffer (pH 3-4), covering a concentration range from 0.005 pg/mL to 50.00 µg/mL. Graph 10 shows the calibration curves for both the original MIP and the recovered MIP.

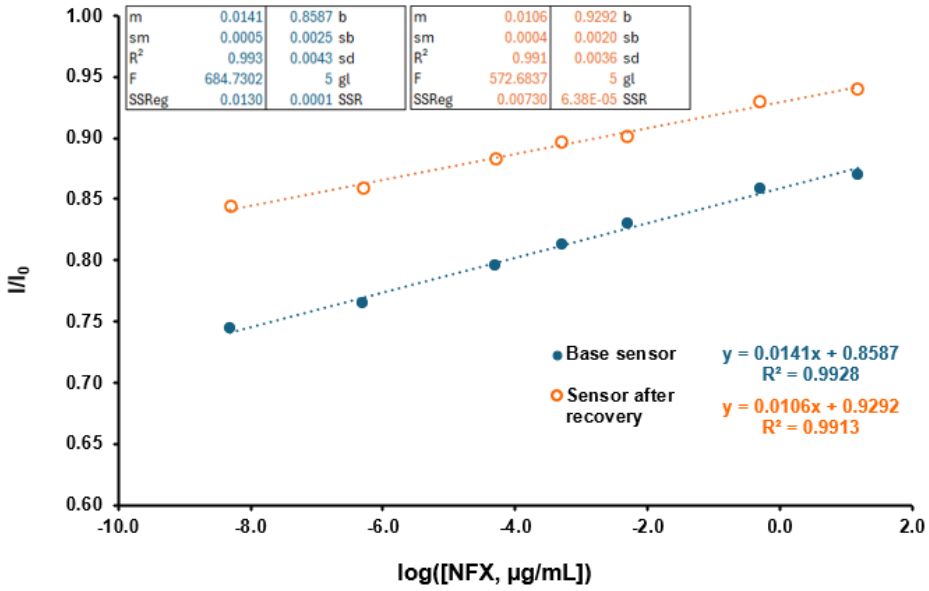

Graph 10 Recovery study of a MIP through calibration using various standard NFX solutions prepared in acetate buffer (pH 3-4), covering a concentration range from 0.005 pg/mL to 50.00 µg/mL. The graph shows the linear fit for each sensor calibration, specifically for both the original and the recovered MIP.

Based on the results obtained, there is clear evidence of a significant shift in the intensity of the current peaks, suggesting that NFX may not have been completely removed from the polymer matrix. As a result, the specific recognition sites originally defined in the MIP may not be fully accessible. This is supported by the reduced sensitivity of the sensor's response, which was higher during the initial construction of the MIP.

However, the response remains linear, with $R^2 > 0.99$, and the standard deviation between the slopes of the curves is around 0.2%. These findings indicate that the sensor can be reused, provided the observed shift pattern is taken into account during each reuse cycle. This allows for correction of the current increase, aligning it with a baseline similar to that of the MIP used for the first time.

4.2.5. Characterization of the Sensor Material by FTIR

The sensor construction steps were evaluated using the FTIR technique. For this purpose, it was necessary to identify the absorption peaks of the molecular components

of the MIP and NIP matrices, namely NFX (Figure 22 and Table 5) and Py (Figure 23 and Table 6), and assess their compatibility with the characteristic functional group peaks of these molecules.

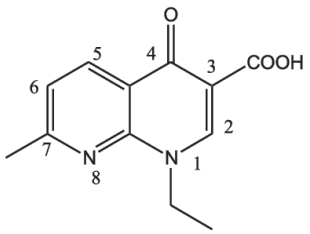

Figure 22 Molecular structure of NFX [117].

Table 5 NFX absorption peaks [118].

Peaks (cm^{-1})	Groups	Peak assignment
3550–3500	Hydroxyl group	Intermolecular H-bonding by single bridge
3500–3300	Imino-moiety of piperazinyl groups	NH stretching vibration
3000–2950	Aromatic, cyclic enes	υ=CH and Ar–H
2750–2700	Ethyl group	υCH2
2500	Acid group	Acidic υOH group
1700	Carbonyl of acids	υC=O stretching vibration
1650–1600	Quinolones	υN–H bending vibration
1500–1450	O–C–O group of acid	υs stretching vibration of the O–C–O group
1300–1250	Hydroxyl group	δO–H bending vibration
1050–1000	C–F groups	υC–F
950–900	Amines	δNH bending vibration
800	Aromatic m-distribution	δAr–H

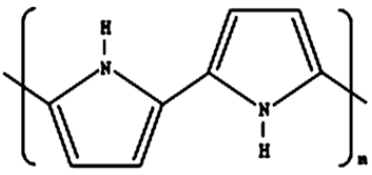

Figure 23 Molecular structure of Py [119].

Table 6 Absorption peaks of Py [120].

Type of band	Peaks (cm^{-1})
Pyrrole unit	1550
(C-N) stretching vibration	1306
(C-H) in plan deformation	1190
(N-H) in plan deformation	1037
(C-H) out-of-plane deformation	901

To better observe the modifications induced in the sensor by the MIP and NIP protocols, FTIR analyses were conducted after the electropolymerization and post-removal stages of the MIP and NIP sensors. Initially, the surface of a sensor following electrochemical cleaning, considered the base sensor, was compared to the electropolymerized MIP and NIP sensors, as shown in Graph 11. Taking into account the absorption peaks of NFX and pyrrole (Table 5 and Table 6), the NIP curves show transmittance reduction peaks in the region between 3600–3000 cm^{-1} (attributed to N–H stretching vibrations of the Py ring); between 1600–1400 cm^{-1} (close to the Py unit vibrations, around 1500 cm^{-1}); and finally between 1300–1100 cm^{-1} (associated with C–N stretching vibrations of pyrrole). These absorption peaks are characteristic of pyrrole in the NIP sensor, which aligns with expectations, as this sensor contains a non-selective pyrrole matrix.

The MIP analysis, in turn, reveals peaks similar to those of the NIP (as expected, since the MIP is a selective matrix for NFX composed of pyrrole), along with additional transmittance drops in regions corresponding to the NFX spectrum, namely between 3600–3000 cm^{-1} (which may be attributed to N–H bonds from both pyrrole and NFX, as well as OH groups from NFX); between 2750–2500 cm^{-1} (possibly associated with carboxylic groups of NFX); between 1650–1600 cm^{-1} (indicating overlap of N–H vibrations from quinolones with Py bands); and more prominently around 1700 cm^{-1} (likely linked to the C=O functional groups of NFX).

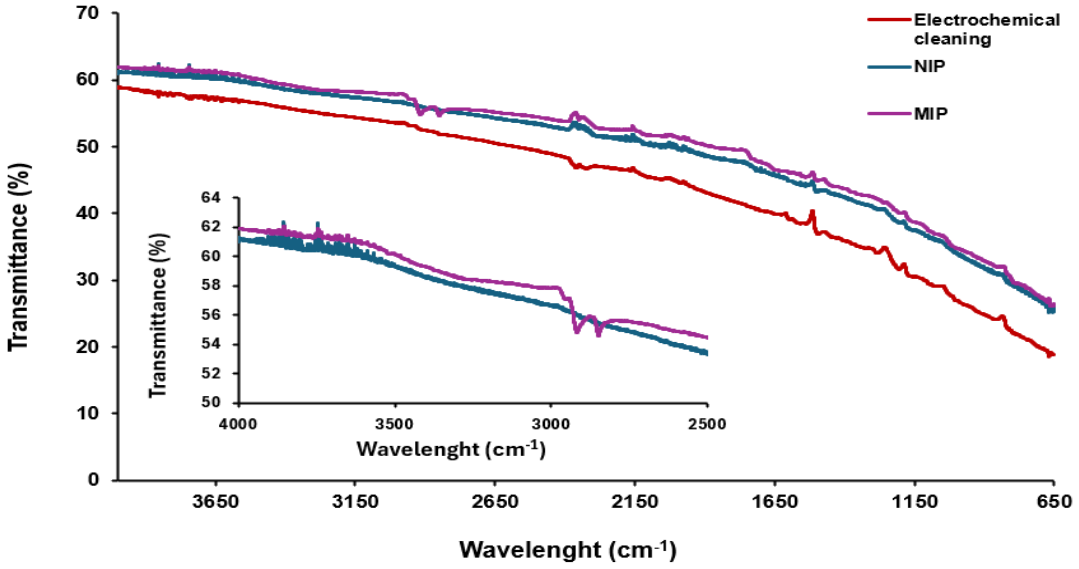

Graph 11 Representative FTIR/ATR spectra of the materials: sensor after electrochemical cleaning, MIP, and NIP.

Analogous to the analysis performed on the MIP, studies were also carried out on NIP sensors at the same construction stages, namely post-electropolymerization, after template removal, and post-calibration, as shown in Graph 12. It is worth noting that, once again, the curves are very similar and follow closely related patterns, confirming that the removal and calibration processes do not induce significant changes in the structure of the polymer matrix. In the NIP representation after electropolymerization, there is a sharp drop in transmittance in the 3600–3000 cm^{-1} region, which can be attributed to N–H stretching vibrations of the Py ring. There is also a drop between 1600–1400 cm^{-1} (close to the Py unit) and in the range between 1300–1100 cm^{-1} (which may be associated with C–N stretching vibrations). The slight variation between the NIP, NIP after removal, and NIP after calibration curves indicates that the molecules adsorbed on the surface of the NIP cause a slight decrease in absorption. However, after removal, absorption returns to baseline values, reinforcing that the Py matrix is stable and that the absorption changes observed in other graphs (with the MIP) are due to the presence or absence of NFX, not to changes in the matrix itself.

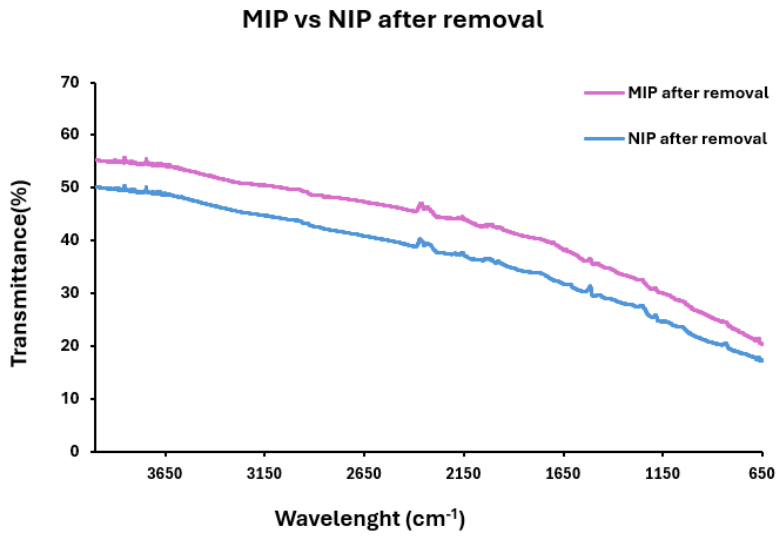

Graph 12 FTIR/ATR Spectra of the Sensor Materials, MIP and NIP, After the Removal Process.

FTIR also allows for an indirect assessment of the quality of NFX molecule removal. For this purpose, the NIP and MIP curves were compared after the removal process, as shown in Graph 12. A clear difference in transmittance between the two spectra is observed (with significantly different peak intensities), although the peaks begin to appear in similar positions. This indicates that the absorption peaks of pyrrole become predominant over those of residual NFX molecules from the antibiotic.

Thus, after the removal process, the MIP and NIP sensors exhibit surfaces that are more similar from an FTIR perspective when compared to their respective surfaces after electropolymerization. This outcome is expected, as both sensors share the same polymeric matrix and the NFX has been predominantly removed from the cavities.

4.3. Validation of the Sensor in Real Samples

The sensor validation stage began with testing on real samples, specifically tap water (pH 6-7) and bottled water from São Martinho (pH 5.95), by performing calibration curves with NFX across a concentration range from 0.005 pg/mL to 50.00 µg/mL. These tests were conducted in triplicate.

4.3.1. Application in Bottled Water Samples

In the first real sample test, the sensor was evaluated using norfloxacin prepared in bottled water samples diluted 50x in buffer solution. The pH was estimated using a pH-sensitive colorimetric strip. After dilution, the solution to be analysed showed a pH range

between 3 and 4, which is expected to result in a positive slope. Detection was successful across the replicates performed. The average linear fit can be observed in the representation shown in Graph 13, along with the NIP records.

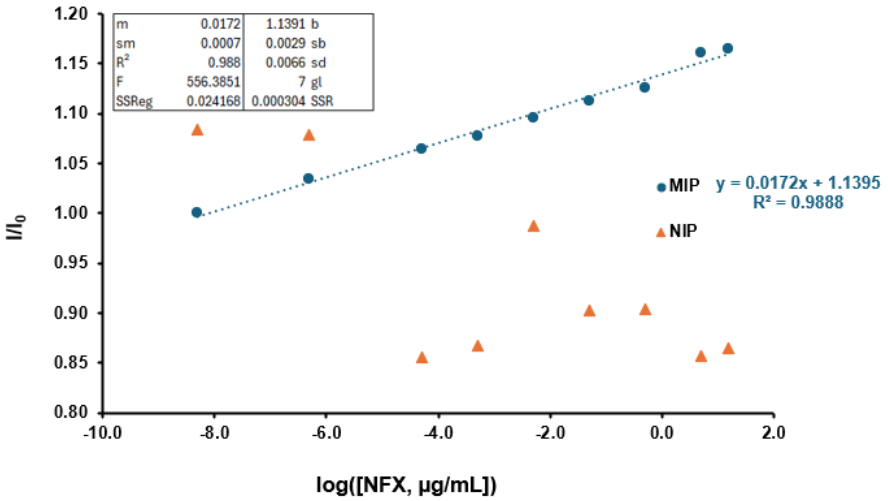

Graph 13 Representation of the Linear Fit Achieved in the MIP and NIP Calibrations, within the NFX Concentration Range from 0.005 pg/mL to 50.00 µg/mL, Prepared in Bottled Water Diluted 50× in Acetate Buffer (pH 3-4).

When calibration is carried out using a buffer, the chemical environment remains controlled, maintaining a constant pH and minimizing the presence of interfering species that could affect the analyte measurement. Comparing the calibration curve obtained with the acetate buffer solution (pH 3-4) to that obtained with the bottled water (pH 5.95), a significant difference in behaviour was observed. This change was evident in the marked reduction of the slope, to approximately half its original value (from 0.0264 for MIP calibration in acetate buffer to 0.0172 for MIP calibration in bottled water diluted 50× in buffer). This may have been caused by the presence of potential interfering ions, such as bicarbonate (11.4 mg/L), chloride (6.7 mg/L), sodium (7.0 mg/L), calcium (2.8 mg/L), and silicon dioxide (13.0 mg/L), all of which are listed in the composition of the tested bottled water, with their respective concentrations indicated in parentheses. Nevertheless, the MIP exhibited good linearity of response ($R^2 > 0.98$), with LOD and LOQ values of 0.500 pg/mL and a relative coefficient of variation of less than 20%. The NIP did not follow a linear trend, as observed with the MIP, and exhibited a relative coefficient of variation of less than 12%.

4.3.2. Application in Tap Water Samples

In the second real sample test, the sensor was evaluated using norfloxacin prepared in tap water samples diluted in 50x buffer solution. The pH was estimated to use a pH-sensitive colorimetric strip. After dilution, the solution to be analysed showed a pH range between 6 and 7, which is expected to result in a negative slope. Similar to the bottled

water test, the sensor demonstrated good selectivity toward the sample, even though it originated from a source known to contain interferents. The representative linear fit of all replicates can be observed in the plot shown in Graph 14, which also includes the NIP chart for this sensor, evaluating the same tap water sample.

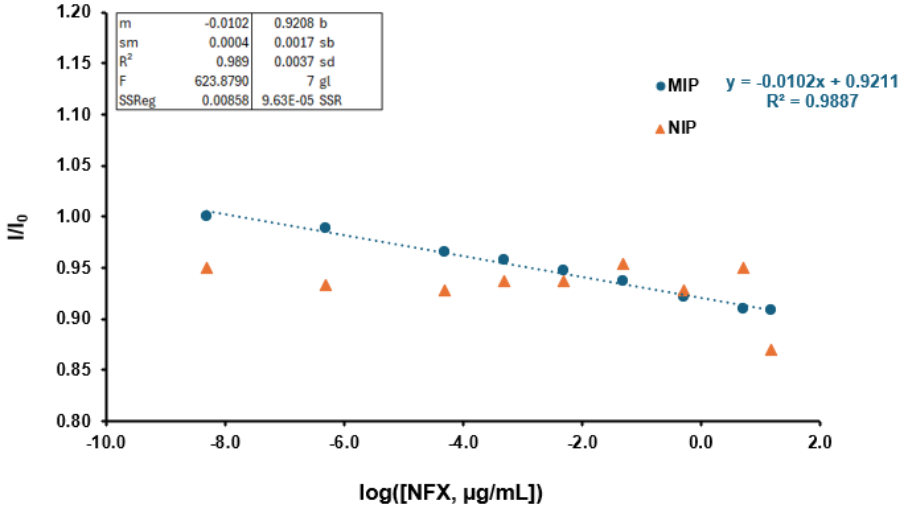

Graph 14 Representation of the Linear Fit Achieved in the MIP and NIP Calibrations, within the NFX Concentration Range from 0.005 pg/mL to 50.00 µg/mL, Prepared in Tap Water Diluted 50× in Acetate Buffer (pH 3-4).

When analysing the calibration curve profile of the MIP in tap water (pH 6-7), a change in trend was observed (negative slope), compared to the MIP tested in acetate buffer (pH 3-4) and the MIP tested in bottled water diluted 50 times in acetate buffer (pH 5.95). This effect can be explained by the amphoteric nature of NFX, a molecule that contains functional groups capable of acting as both acids and bases. The charge of NFX is determined by its functional groups: the carboxylic group (–COOH), which is a weak acid capable of losing a proton and acquiring a negative charge by converting into carboxylate ($–COO^-$), and the piperazinyl group (–NH), a weak base that can accept a proton and acquire a positive charge by forming the ammonium ion ($–NH_2^+$). In acidic pH, there is an excess of protons, favouring the protonation of the piperazinyl group, which becomes positively charged. In this condition, the carboxylic group tends to remain in its neutral form (–COOH), resulting in an overall positive net charge. In a basic medium, where protons are scarce and OH^- groups are abundant, the carboxylic group loses a proton, becoming negatively charged ($–COO^-$), while the piperazinyl group loses its proton and becomes neutral. Therefore, the net charge of NFX at basic pH is negative. At neutral pH, close to the isoelectric point of NFX, the molecule predominantly assumes a zwitterionic form, in which the carboxylic group is deprotonated ($–COO^-$) and the

piperazinyl group is protonated ($–NH_2^+$). In this form, the opposite charges cancel each other out, resulting in an overall net charge of zero.

In general, the MIP calibrations in tap water showed a sensitivity similar to that achieved in bottled water, but with an opposite trend (–0.0102 μA/μg·mL^{-1}). Regarding linearity, the MIP tested in this sample, like the MIP tested in bottled water, showed a good response with an $R^2 > 0.98$, identical LOD and LOQ values (0.005 pg/mL), and a relative coefficient of variation of less than 20%. As for the NIP, the sensor's response did not show a linear trend, as observed with the MIP, and showed a relative coefficient of variation of less than 12%. Thus, the detection methodology applied to real samples demonstrated robust analytical performance. The detection and quantification limits fall within the concentrations of NFX found in wastewater, as described in the introduction.

4.4. Selectivity study

A fundamental characteristic of a molecularly imprinted sensor is its selectivity. As discussed in the previous section, the sensor demonstrated strong binding affinity with NFX molecules. To evaluate selectivity, three significant norfloxacin interferents were tested within the context of electrochemical sensors selective to NFX via MIP technology.

Among those tested were quinolone-class antibiotics, such as ciprofloxacin, due to their molecular structure being similar to that of the target analyte, particularly in terms of functional groups and the quinolone backbone. These functional groups can interact with the MIP’s recognition sites, potentially causing cross-signals and overestimations of norfloxacin concentration.

Other compounds, such as urea and sulfadiazine, may also act as interferents. Although their chemical structures differ, they can interfere with the sensor through other mechanisms. Urea, being a small and highly polar molecule, may affect the interface between the polymer and the electrolyte, altering analyte diffusion or the kinetics of the electrochemical reaction. Sulfadiazine, a sulfonamide-class compound, can generate an electrochemical signal at potentials close to that of NFX, resulting in signal overlap and challenges to accurate quantification.

Therefore, MIP optimization must consider not only structural analogues but also molecules that mimic matrix effects, especially those commonly found in real-world samples. Calibration curves for the interferents can be found in graph 15 for sulfadiazine, ciprofloxacin, and urea.

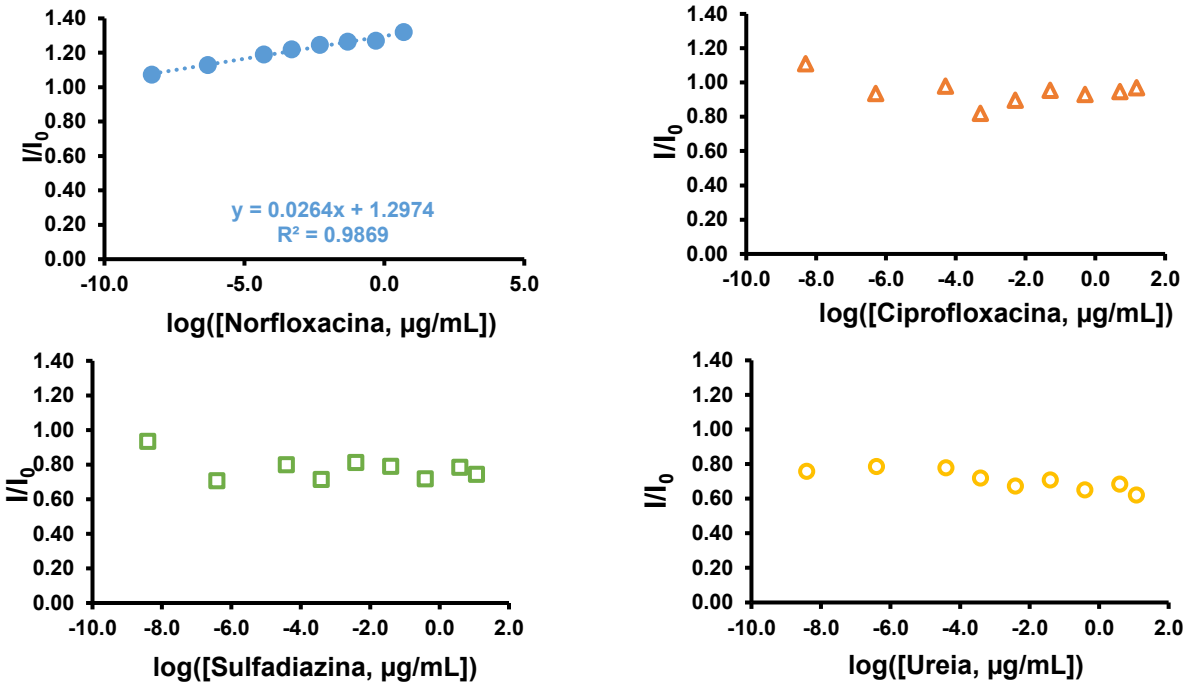

Graph 15 Evaluation of the main NFX interferents in electrochemical sensors modified with MIP: ciprofloxacin, sulfadiazine, and urea.

It is worth highlighting, as shown in the bar chart analysis, a visually linear increasing trend for the NFX sample in buffer within the working range of 0.005 pg/mL to 50.00 µg/mL. For the other interfering substances, different patterns from the expected linearity were observed, using the same concentration range studied for NFX. This indicates that the sensors do not respond linearly to these interferents.

As observed in graph 15, these molecules do not show an affinity trend toward the MIP cavities, suggesting that the cavities are not selective for these interfering analytes, and consequently, the NFX signal will not be significantly affected. It should be noted that the signal variation was observed at both high and low sensor concentrations, within the same evaluation range used for NFX calibration in buffer. Minor deviations can be easily corrected by further dilution of the samples in buffer.

4.5. Integration of the Electrochemical Sensor into a Microfluidic Module and Validation

Microfluidics can be integrated with electrochemical sensors, playing a crucial role in stages ranging from incubation to calibration and measurement. The flow regime can be either static or dynamic, and the choice of regime should be tailored to each reaction, considering whether reagent renewal or product removal is necessary. For the proposed

electrochemical sensor for NFX detection, the static regime is more advantageous as it enhances analyte, sensor surface interaction and allows for greater control over mass transport mechanisms.

Overall, calibrations within microfluidic modules are beneficial due to increased protection against interferents, temperature fluctuations, air currents, light sources, and vibrations. In static microfluidics, the absence of forced flow simplifies the analytical process, making mass transport predominantly governed by molecular diffusion. The small dimensions of the channel facilitate rapid diffusion, resulting in a more stable distribution across the sensor surface. Additionally, the micrometric setup allows for significant reagent savings and a notably shorter response time for analytical measurements.

In this context, new calibrations were performed to study the electrochemical sensor integrated into microfluidic modules using bottled water and tap water samples spiked with NFX. Graphs 16 and 17 illustrate the linear adjustments obtained during the study of the MIP-modified electrochemical sensor and its NIP equivalent for tap water and bottled water, respectively. For tap water, the sensor was tested with norfloxacin prepared in samples diluted in a 50x buffer solution. The pH was estimated using a pH-sensitive colorimetric strip. After dilution, the solution presented a pH range between 6 and 7, which is expected to result in a negative slope. The sensor was placed inside a microfluidic module designed explicitly for electrochemical transduction, as shown in Graph 16 and discussed in more detail in the section on modular microfluidic systems.

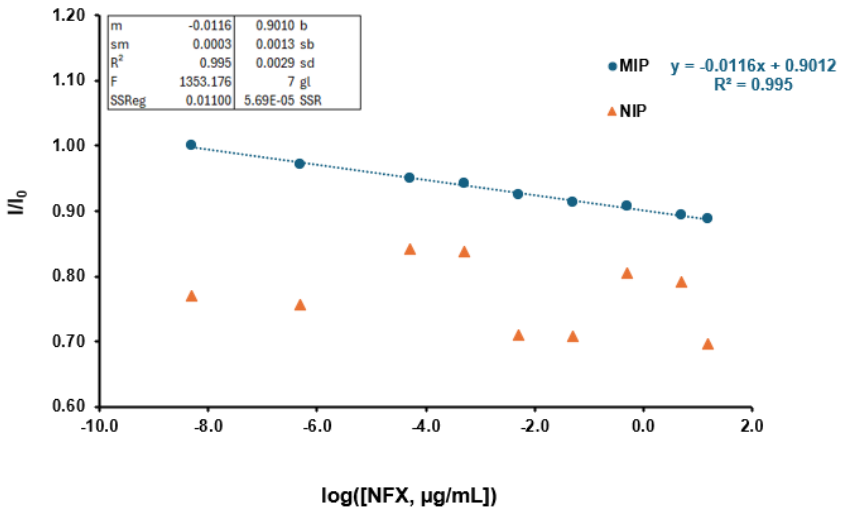

Graph 16 Linear fit obtained from the calibration of the sensor in a 3D printing microfluidic module used to analyze a real sample of tap water.

In the calibration of sensors in tap water, within a 3D printing microfluidic module, as shown in Graph 16, the average coefficient of determination was 0.995, with LOD and LOQ values of 0.005 pg/mL and a relative coefficient of variation below 20%. The NIP did not follow a linear trend as observed with the MIP and showed a relative coefficient of variation < 12%.

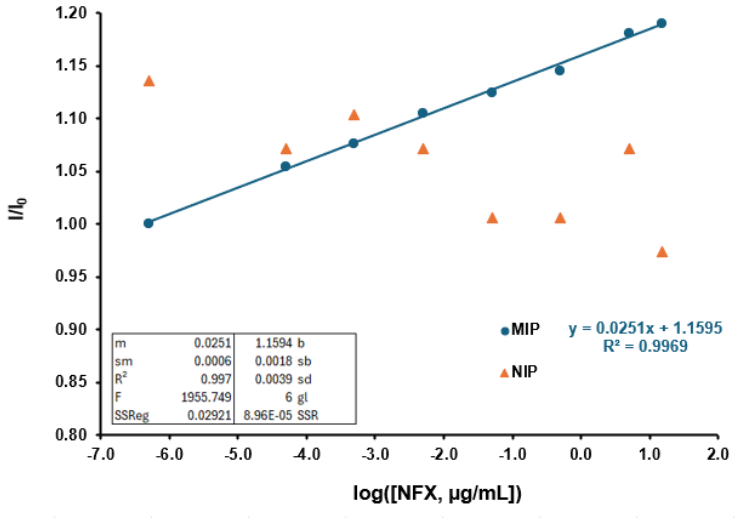

Graph 17 Linear fit obtained from the calibration of the sensor in a 3D printing microfluidic module used to analyze a real sample of bottled water.

For bottled water calibrated within a 3D printing microfluidic module, as represented in Graph 17, the average linearity coefficient was 0.997, with LOD and LOQ values of 0.500 pg/mL and a relative coefficient of variation of less than 17%. The NIP did not follow a linear trend, as observed with the MIP, and showed a relative coefficient of variation of less than 13%.

The calibration results obtained within microfluidic modules were superior to those found in the systems outside the microfluidic setup. This improvement is a consequence of controlled diffusion and continuous delivery without turbulence or flow variations, hallmarks of microfluidic systems. The inherent stability of controlled microfluidic environments is reflected in a more pronounced linear relationship between peak current and analyte concentration.

4.6. Modular Microfluidic Systems

Despite notable advancements in design, microfluidics still faces challenges due to monolithic architecture concepts that restrict analysis transduction to a single mechanism per chip. This limitation can lead to the need for additional equipment and longer processing times to complete analyses. The solution to this problem is modular microfluidics. In this concept, modules operate independently in terms of transduction

mechanisms, yet their outputs can be integrated into a single signal and reconfigured quickly.

This structure enables independent, customizable modules, providing flexible output configurations. Known as micro total analysis systems (μTAS), this approach enables the development of portable platforms that can be more easily transported outside the laboratory. μTAS is gaining increasing attention in scientific publications and patents, becoming a growing trend in the biomedical device industry.

The following section presents an attempt to build a modular concept for sensors with different transduction mechanisms, as well as parallel sensory systems for multiple sensors and samples.

4.6.1.3D printing Modules

Due to increased accessibility to the Stratasys Neo® 450/800 setup, the first microfluidic modules for electrochemical sensor calibration testing were constructed using a resin as the building material. This material exhibits relevant physical and chemical properties such as optical transparency and water resistance, making it ideal for fluid flow visualization and analysis. In many ways, its properties are similar to Acrylonitrile Butadiene Styrene (ABS) and Polyethylene Terephthalate (PET).

Initial attempts to fit the electrochemical sensor into the module began with a horizontal configuration, testing sealing mechanisms based on mechanical pressure, but with limited success. Consequently, the module was reoriented vertically to mitigate challenges inherent to inclined or horizontal setups, particularly fluid leakage. This adjustment helped resolve issues related to sealing with films and membranes. Additionally, the vertical configuration facilitated easier insertion and replacement of the sensor within the setup. The sensor’s design, which requires only 50 μL of volume, enables precise incubation control with minimal reagent consumption. A peristaltic pump (ISMATEC ISM831C Reglo digital) was added, and after experimentation, the optimized flow rate was set at approximately 80 μL/min. The pump was configured to both advance and retract the fluid, enabling more precise control over flow progression and return to the reservoir. This ensured uniform fluid retention across multiple measurements, reagent recovery, and temporal control of reagent input and output. The setup for the microfluidic module of the electrochemical sensor is shown in Figure 24.

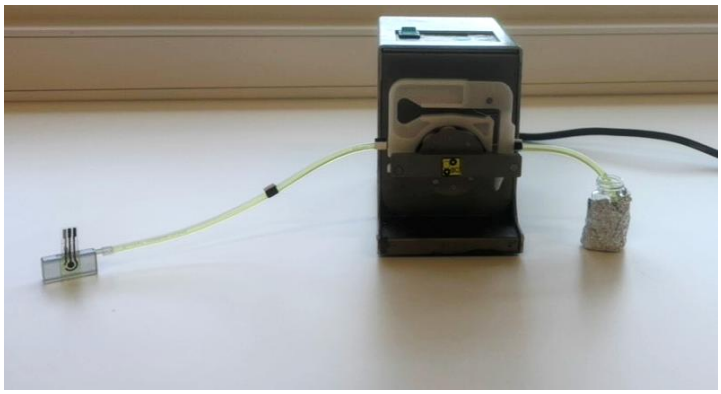

Figure 24 3D printing microfluidic module designed for incubation and calibration of electrochemical sensors.

In this initial configuration, it was possible to carry out the calibration and iron reading steps using square wave voltammetry across all points of the curves from tests with real samples in microfluidics. Using the same material as the previous module, additional microfluidic modules were developed to house sensors with different transduction mechanisms, namely colorimetric and photoacoustic systems. These modules were integrated into our modular setup to share reagents (specifically the NFX solution), which allows for increased sensitivity by acquiring multiple signals to measure concentration. Furthermore, the photoacoustic and colorimetric modules feature two to three input/output ports to enable the injection of iron and hydrogen hydroxide reagents required for the reactions involved in these transduction mechanisms.

The main advantage of this modular approach lies in its flexibility and on-demand reconfigurability, allowing the creation of complete yet fully independent systems. In the case of measuring NFX concentrations, the addition of these data can complement the electrochemical sensor, refining sensitivity in range segments where the sensor shows a lower slope or a tendency toward a plateau. In this way, it acts as a layered device for safety and redundancy, potentially signalling failure in a transducer component or reducing susceptibility to samples contaminated by multiple interferents or unusual external conditions. This reconfigurable setup is illustrated in Figure 25 below.

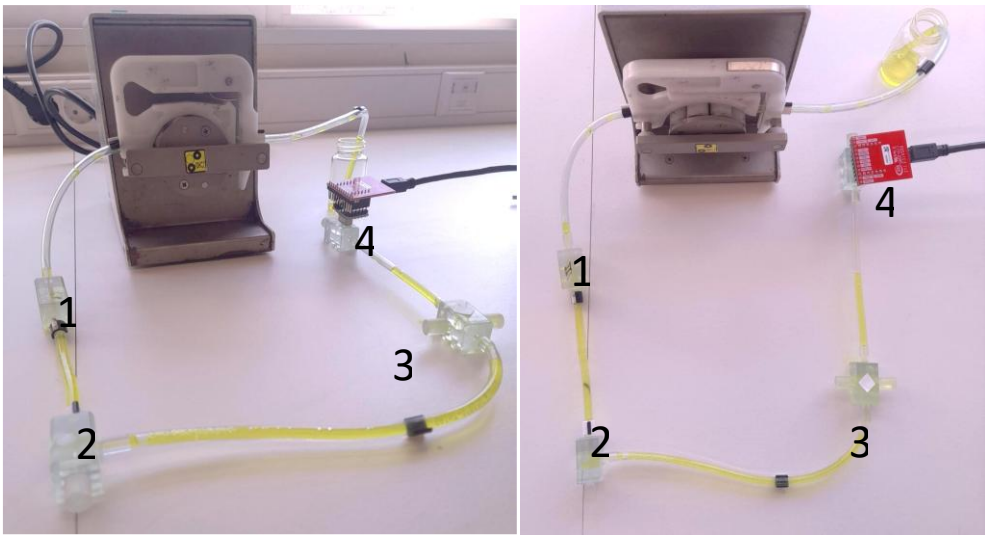

Figure 25 Modular schematic of chained 3D printing components for electrochemical, colorimetric, and photoacoustic readings. Flow is controlled by a peristaltic pump at a rate of 80 µL/min. 1- Module for electrochemical sensor placement, 2-Reagent distribution module, 3-Microfluidic module for colorimetric sensor (paper placement), 4-Microfluidic module for photoacoustic sensor

In the previous setup, a configuration referred to as modular was established. The NFX solution is initially delivered to the microfluidic module via a peristaltic pump. After an incubation period of approximately 30 minutes, the solution progresses, also under control of the peristaltic pump, to the colorimetric and photoacoustic transduction modules. Upon arrival at these sensors, complementary reagents can be added through the lateral inlets of the modules.

In the colorimetric module, an iron source is injected into the modular cavity to react with the NFX solution. In the photoacoustic module, two lateral inlets are used to introduce both an iron source and hydrogen peroxide. Below the colorimetric module, a small hole allows the resulting iron/NFX mixture to drain onto a filter paper located at the bottom of the cube. The photoacoustic sensor is positioned on the surface of its module to begin capturing the CO_2 released during the Fenton reaction. More details on the reactions and transduction mechanisms involved in these two modules can be found in **Appendix A3. Complementary Microfluidic Transduction Modules.** The electrochemical sensor, in turn, receives the iron cyanide solution at a later stage to perform electrochemical readings using a potentiostat.

From these two setups, we observed some issues related to the stability of the microfluidic components, particularly due to the connecting tubes that induce twisting

and slight imbalances in the modules, leading to difficulties in securing them and resulting in leaks and disrupted fluid flow. To overcome this limitation, an enhanced modular system with a reversible locking design was developed. This new approach aimed to ensure positional stability of the modules by anchoring them at specific points to counteract the tension caused by the connecting tubes during calibration, measurement, and reagent flow stages.

The locking strategy involved the synthesis of bases inspired by the LEGO® style, allowing for unlimited system expansion. This scalability supports serial expansion, allowing for the integration of multiple sensors while maintaining flexibility for customization based on the analyte being analysed. Additionally, this new modular architecture allows for adjustment of the relative height between modules, leveraging gravity to assist in reagent transport in more extensive systems. An image of this setup is shown in Figure 26.

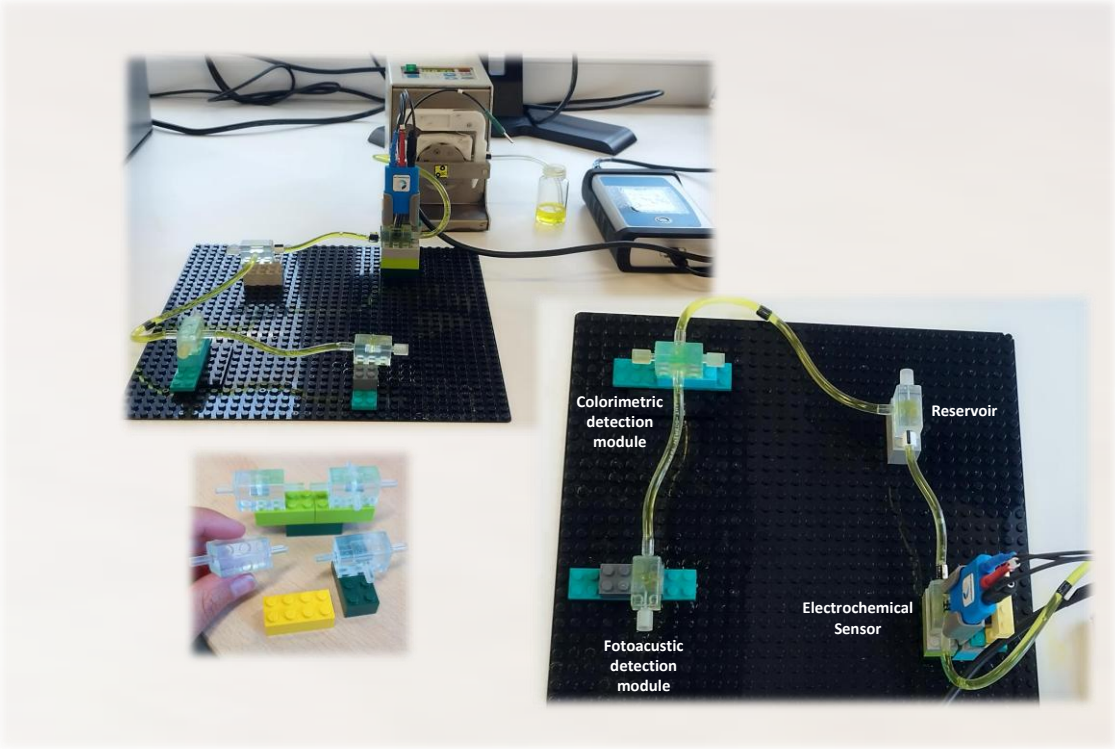

Figure 26 Adaptation of microfluidic module mounting bases using LEGO interlocking profiles, allowing setup stability in sequential chains of microfluidic modules.

Finally, inspired by studies proposing microfluidic modules in the shape of a Rubik's cube. A platform with rotational freedom and positional flexibility for integrated modular components was replicated, based on the referenced work [121]. This setup enables the integration of various types of sensors, allowing for the simultaneous analysis of three samples through sequential electrochemical, colorimetric, and photoacoustic

transductions in parallel. It vividly demonstrates the high parallelization potential of this concept.

Additionally, some intermediate modules incorporated mixer designs, which are essential for reagent preparation and reaction optimization in colorimetric and photoacoustic sensors. The ability to move and reconfigure modules is a key advantage, resulting in a complete, independent, portable, customizable, and compact setup, ideal for deployment in field environments outside the laboratory. Notable benefits include reagent savings, reduced processing time for multiple samples, and improved analytical efficiency. The Rubik-style microfluidic setup is shown in Figure 27.

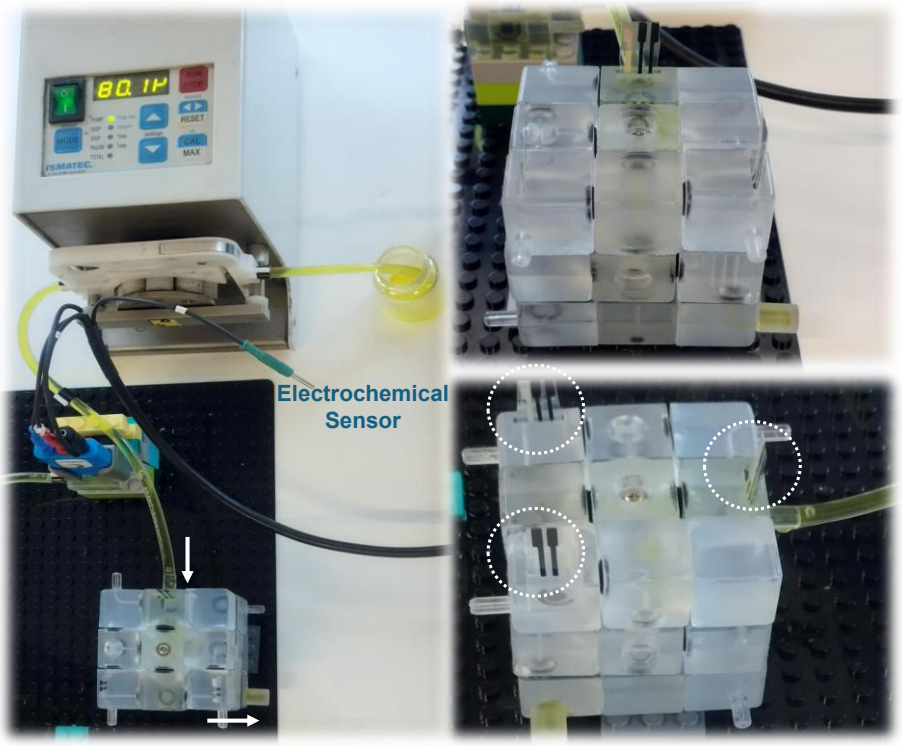

Figure 27 Modular microfluidic replica of a Rubik's Cube. The module features three inlets for electrochemical sensors, reagent mixing modules, three outlets for colorimetric transducers (designed to deliver reagents onto paper), and three ports for connecting photoacoustic sensors.

4.6.2. Complementary tests

To complement the electrochemical assays performed in the microfluidic device, two additional modules with different transduction mechanisms were integrated: optical transduction (colorimetric and fluorescence) and optoacoustic transduction (photoacoustic). Preliminary results from the integration of these modules are presented in **Appendix A4. Alternative/complementary transductions for the electrochemical detection of NFX**. Additionally, the appendices present an alternative for antibiotic

detection (**Appendix A5. Electrowetting Interfaces and Other "Touchless" Perspectives**), as well as alternative methods for fabricating microfluidic modules (**Appendix A6. Alternative Methods for Microfluidic Module Fabrication**).

5. Conclusion

In this study, an electrochemical sensor for detecting NFX was developed and integrated into a modular microfluidic system, which is associated with other transduction mechanisms. The choice to create a Molecularly Imprinted Polymer (MIP) aimed at achieving selectivity for the NFX molecule proved to be effective, as it provided good sensitivity and interference resistance at low cost. The sensor achieved a limit of detection (LOD) and limit of quantification (LOQ) of 0.005 pg/mL, well below the typical concentrations of norfloxacin quinolones found in wastewater. When compared with the electrochemical sensors in Table 2, it is evident that the LOD is the only one in the picogram range. This enables the detection of trace amounts of these antibiotics in water, offering an efficient, fast, and user-friendly method for monitoring water resources. It is also worth emphasizing that the sensor did not exhibit linear calibration patterns for the main NFX interferents, further reinforcing the selectivity of the MIP cavities constructed under NFX concentration of 7.5 mM and Py 2.0 mM. The working range of the electrochemical sensor, spanning from 0.005 pg/mL to 50 µg/mL, enables the detection of a broad spectrum of concentrations in wastewater without saturation limitations.

Real sample tests indicated that the choice of dilution solution still requires optimization. This optimization is closely related to the sample composition, as variations in salt content and pH levels can cause significant disturbances in the distribution of electric charge within the polymer matrix. Such disorders may mimic the behaviour of an interferent, leading to overestimated or underestimated measurements. Therefore, this optimization is essential for defining corrective actions based on the sample's pH or specific compositions, enabling proper adjustment of current shifts (either upward or downward) through appropriate dilution. One limitation to consider is the sensor’s recovery process, which shows a current shift after each reuse. No optimization or compensation model has yet been developed to account for this shift, which is caused by residual NFX molecules from previous readings. However, linearity is maintained. Additionally, the repeatability of data in consecutive measurements confirmed the reliability and robustness of the sensor’s construction method.

Beyond the construction and calibration of the electrochemical sensor, experimental calibrations of NFX in buffer were prepared for other transduction mechanisms, including photoacoustic effect, colorimetric assays, fluorescence assays with CDs, and magneto-osmotic assays. All four calibration methods demonstrated sufficient linearity (based on slope and determination coefficient) to be used as complementary tools to the

electrochemical electrode, providing additional insights into prognostic concentration ranges or helping determine which electrochemical adjustment to apply (sensor with or without CDs).

Regarding the electrochemical sensor, performance gains were observed when incubation, calibration, and reading were conducted within a microfluidic module. Outside the microfluidic modules, calibrations of real samples (bottled water and tap water) yielded determination coefficients (R^2) ranging from 0.980 to 0.990 and slopes of -0.0102 ± 0.0004 and 0.0172 ± 0.0007, respectively. Integration into a microfluidic module significantly improved linearity, raising R^2 to 0.995 for tap water and 0.996 for bottled water, confirming the sensitivity benefits of working within microfluidic modules, showing slopes of -0.0116 ± 0.0003 and 0.0251 ± 0.0006, respectively.

Among the other transduction methods, the photoacoustic system stood out with an almost perfect linear fit (R^2 = 0.999) and maintained the same LOD and LOQ as the electrochemical sensor. Fluorescence analysis also showed a good linear fit (R^2 = 0.994), with an LOD and LOQ of $4{,}25\times10^{-3}$ µg/mL. The magneto-osmotic method demonstrated a strong correlation (R^2 = 0.963), followed by the colorimetric method with R^2 = 0.986. These sensors can be integrated into microfluidic modules to form highly sensitive systems, enabling redundancy in measurements in the event of reading discrepancies or external failures that affect the electrochemical sensor.

The modular microfluidic strategies, utilizing LEGO base adapters and a replica of the RUBIK microfluidic module, represent an intelligent design solution that enhances portability and enables point-of-care sensor applications. The material synthesis strategy also proves economically viable. For the module fabrication, the cost per modular piece is less than 1€ lower (see Table A1 that presents a comparison of unit synthesis costs) than the cost of similar components produced by other methods referenced in the annexes. While setup expenses may be significantly higher for small-scale or unit production, considering setup and post-processing costs, the choice of the Stratasys Neo 450/800 represents a highly relevant economic decision. On a large scale, the operator reduces expenses related to clean rooms and personnel for equipment handling. While the machine is printing, no operator is required, and the part can be produced directly from a design file sent from the computer to the printer, eliminating the need for masks or moulds. This enables a more direct synthesis process, without costly intermediaries, and with minimal material waste. All of this translates into significant savings, as the operator's main expense is the resin, which in turn can yield multiple parts.

6. Future Work

Although this study has shown promising results, future work may focus on improving sensor reuse protocols to maximize NFX removal, thereby extending the sensor's lifespan and aligning with sustainability principles. Additionally, the maximum number of recovery cycles the sensor can undergo without compromising its sensitivity or accuracy should be better characterized. At the same time, the dissolution conditions for measurements should be more clearly defined. One possibility would be to integrate data obtained from other transduction mechanisms, such as those mentioned, to eventually develop an analytical computational model that indicates the optimal dilution rate for databases generated through simultaneous transductions. To achieve this, dedicated studies focusing on calibrations and nuances of other detection methods are necessary.

In the future, photoacoustic methods and the refinement of a colorimetric model are likely to be prioritized, although magneto-osmotic setup models may be applied under conditions of extreme improvisation. Regarding the microfluidic setup, efforts should be directed toward in situ coupling of the electrowetting platform as an additional option for platform digitization, a challenge that is undoubtedly great. Identical protocols may be used to construct sensors for other antibiotics in the quinolone class or for other classes whose prescriptions are related to more prevalent infections.

An interesting challenge is to couple specific sensors with the main interferents, such as those cited in this study, so that the outputs of both analytes and interferents constitute an excellent dataset for generating exact and comprehensive models by artificial intelligence. Finally, cleaning protocols for the modules after calibrations or iron readings should be considered both for the removal of iron residues and for aesthetic purposes. An optimal cleaning time should be established, as well as a chemical removal protocol for these reagents. In terms of the project's potential, one immediate suggestion is to use photoacoustic modules for calibrating electrochemical sensors, alongside exploring pyrrole-based MIP solutions for synthesizing selective sensors targeting biological analytes. The selectivity offered by MIPs can lead to savings of hundreds of euros compared to antibody-based assays. Moreover, simultaneous photoacoustic, electrochemical, and colorimetric calibration may prove to be a viable method—even if the individual sensors don't exhibit high sensitivity.

7. References

[1] Eurostat, “Mortality and life expectancy statistics,” online. Jun. 15, 2025. Accessed on: Jun. 15, 2025. Available: https://ec.europa.eu/eurostat/statistics-explained/index.php?title=Mortality_and_life_expectancy_statistics#Life_expectancy_at_birth.
[2] J. P. Mackenbach and C. W. Looman, “Life expectancy and national income in Europe, 1900-2008: an update of Preston’s analysis,” *International Journal of Epidemiology*, vol. 42, no. 4, pp. 1100–1110, Aug. 2013, doi: 10.1093/ije/dyt122.
[3] H. Zeng *et al.*, “The current status and prevention of antibiotic pollution in groundwater in China,” *International Journal of Environmental Research and Public Health*, vol. 19, no. 18, p. 11256, Sep. 2022, doi: 10.3390/ijerph191811256.
[4] M. Naghavi *et al.*, “Global burden of bacterial antimicrobial resistance 1990–2021: a systematic analysis with forecasts to 2050,” *The Lancet*, Sep. 2024, doi: 10.1016/s0140-6736(24)01867-1.
[5] E. Enshaie, S. Nigam, S. Patel, and V. Rai, “Livestock antibiotics use and antimicrobial resistance,” *Antibiotics*, vol. 14, no. 6, p. 621, Jun. 2025, doi: 10.3390/antibiotics14060621.
[6] H. Zeng *et al.*, “The current status and prevention of antibiotic pollution in groundwater in China,” *International Journal of Environmental Research and Public Health*, vol. 19, no. 18, p. 11256, Sep. 2022, doi: 10.3390/ijerph191811256.
[7] L. Zhao *et al.*, “Molecular Epidemiology and Genetic Diversity of Fluoroquinolone-Resistant Escherichia coli Isolates from Patients with Community-Onset Infections in 30 Chinese County Hospitals,” *Journal of Clinical Microbiology*, vol. 53, no. 3, pp. 766–770, Dec. 2014, doi: 10.1128/jcm.02594-14.
[8] A. Dalhoff, “Global Fluoroquinolone Resistance Epidemiology and Implictions for Clinical Use,” *Interdisciplinary Perspectives on Infectious Diseases*, vol. 2012, pp. 1–37, Jan. 2012, doi: 10.1155/2012/976273.
[9] D. C. Hooper, J. S. Wolfson, E. Y. Ng, and M. N. Swartz, “Mechanisms of action of and resistance to ciprofloxacin.,” *PubMed*, vol. 82, no. 4A, pp. 12–20, Apr. 1987, [Online]. Available: https://pubmed.ncbi.nlm.nih.gov/3034057
[10] K. Gupta, T. M. Hooton, and W. E. Stamm, “Isolation of fluoroquinolone-resistant rectal Escherichia coli after treatment of acute uncomplicated cystitis,” *Journal of Antimicrobial Chemotherapy*, vol. 56, no. 1, pp. 243–246, May 2005, doi: 10.1093/jac/dki169.
[11] D. A. Talan, S. S. Takhar, A. Krishnadasan, F. M. Abrahamian, W. R. Mower, and G. J. Moran, “Fluoroquinolone-Resistant and Extended-Spectrum β-Lactamase–ProducingEscherichia coliInfections in Patients with Pyelonephritis, United States1,” *Emerging Infectious Diseases*, vol. 22, no. 9, Aug. 2016, doi: 10.3201/eid2209.160148.
[12] J. Garau *et al.*, “Emergence and Dissemination of Quinolone-Resistant Escherichia coli in the Community,” *Antimicrobial Agents and Chemotherapy*, vol. 43, no. 11, pp. 2736–2741, Nov. 1999, doi: 10.1128/aac.43.11.2736.
[13] J.-H. Kim *et al.*, “Quinolone resistance in Community-Acquired acute pyelonephritis,” *Kidney Research and Clinical Practice*, vol. 25, no. 4, pp. 571–578, Jan. 2006, [Online]. Available: https://www.kci.go.kr/kciportal/ci/sereArticleSearch/ciSereArtiView.kci?sereArticleSearchBean.artiId=ART001148670.
[14] D. Thompson, J. Xu, J. Ischia, and D. Bolton, “Fluoroquinolone resistance in urinary tract infections: Epidemiology, mechanisms of action and management strategies,” *BJUI Compass*, vol. 5, no. 1, pp. 5–11, Aug. 2023, doi: 10.1002/bco2.286.
[15] H. Lode, G. Hoffken, M. Boeckk, N. Deppermann, K. Borner, and P. Koeppe, “Quinolone pharmacokinetics and metabolism,” *Journal of Antimicrobial Chemotherapy*, vol. 26, no. suppl B, pp. 41–49, Jan. 1990, doi: 10.1093/jac/26.suppl_b.41.
[16] K. Tang and H. Zhao, “Quinolone Antibiotics: Resistance and therapy,” *Infection and Drug Resistance*, vol. Volume 16, pp. 811–820, Feb. 2023, doi: 10.2147/idr.s401663.
[17] F. J. Álvarez-Martínez, E. Barrajón-Catalán, and V. Micol, “Tackling Antibiotic Resistance with Compounds of Natural Origin: A Comprehensive Review,” *Biomedicines*, vol. 8, no. 10, p. 405, Oct. 2020, doi: 10.3390/biomedicines8100405.
[18] K. Bianco *et al.*, “Mobile resistome of microbial communities and antimicrobial residues from drinking water supply systems in Rio de Janeiro, Brazil,” *Scientific Reports*, vol. 12, no. 1, Nov. 2022, doi: 10.1038/s41598-022-21040-7.
[19] C. Yang and T. Wu, “A comprehensive review on quinolone contamination in environments: current research progress,” *Environmental Science and Pollution Research*, vol. 30, no. 17, pp. 48778–48792, Mar. 2023, doi: 10.1007/s11356-023-26263-3.

[20] R. Rosal *et al.*, “Occurrence of emerging pollutants in urban wastewater and their removal through biological treatment followed by ozonation,” *Water Research*, vol. 44, no. 2, pp. 578–588, Jul. 2009, doi: 10.1016/j.watres.2009.07.004.
[21] A. C. Faleye, A. A. Adegoke, K. Ramluckan, J. Fick, F. Bux, and T. A. Stenström, “Concentration and reduction of antibiotic residues in selected wastewater treatment plants and receiving waterbodies in Durban, South Africa,” *The Science of the Total Environment*, vol. 678, pp. 10–20, Apr. 2019, doi: 10.1016/j.scitotenv.2019.04.410.
[22] J. Hu, J. Zhou, S. Zhou, P. Wu, and Y. F. Tsang, “Occurrence and fate of antibiotics in a wastewater treatment plant and their biological effects on receiving waters in Guizhou,” *Process Safety and Environmental Protection*, vol. 113, pp. 483–490, Dec. 2017, doi: 10.1016/j.psep.2017.12.003.
[23] A. M. P. T. Pereira, L. J. G. Silva, L. M. Meisel, and A. Pena, “Fluoroquinolones and tetracycline Antibiotics in a Portuguese aquaculture system and aquatic surroundings: Occurrence and environmental impact,” *Journal of Toxicology and Environmental Health*, vol. 78, no. 15, pp. 959–975, Aug. 2015, doi: 10.1080/15287394.2015.1036185.
[24] X.Fu et al., “Antibiotic Pollution Characteristics and Ecological Risk Assessment of Water Bodies Around Livestock and Poultry Breeding in Dalian,” Environ. Eng., vol. 41, no. 4, pp. 164–169, 2023, doi: 10.13205/j.hjgc.202304023.
[25] Q. F. Han, C. Song, X. Sun, S. Zhao, and S. G. Wang, “Spatiotemporal distribution, source apportionment and combined pollution of antibiotics in natural waters adjacent to mariculture areas in the Laizhou Bay, Bohai Sea,” *Chemosphere*, vol. 279, p. 130381, Mar. 2021, doi: 10.1016/j.chemosphere.2021.130381.
[26] C. Liu, V. Nanaboina, G. V. Korshin, and W. Jiang, “Spectroscopic study of degradation products of ciprofloxacin, norfloxacin and lomefloxacin formed in ozonated wastewater,” *Water Research*, vol. 46, no. 16, pp. 5235–5246, Jul. 2012, doi: 10.1016/j.watres.2012.07.005.
[27] M. Lombardo-Agüí, C. Cruces-Blanco, A. M. García-Campaña, and L. Gámiz-Gracia, “Multiresidue analysis of quinolones in water by ultra-high perfomance liquid chromatography with tandem mass spectrometry using a simple and effective sample treatment,” *Journal of Separation Science*, vol. 37, no. 16, pp. 2145–2152, May 2014, doi: 10.1002/jssc.201400223.
[28] T. Ding *et al.*, “[Simultaneous determination of 19 quinolone residues in honey using high performance liquid chromatography-tandem mass spectrometry].,” *PubMed*, vol. 27, no. 1, pp. 34–8, Jan. 2009.
[29] K. Wen *et al.*, “Improved fluoroquinolone detection in ELISA through engineering of a broad-specific single-chain variable fragment binding simultaneously to 20 fluoroquinolones,” *Analytical and Bioanalytical Chemistry*, vol. 403, no. 9, pp. 2771–2783, May 2012, doi: 10.1007/s00216-012-6062-z.
[30] X. Liu *et al.*, “A novel biosensor based on antibody controlled isothermal strand displacement amplification (ACISDA) system,” *Biosensors and Bioelectronics*, vol. 209, p. 114185, Apr. 2022, doi: 10.1016/j.bios.2022.114185.
[31] N. Chaudhary, A. K. Yadav, J. G. Sharma, and P. R. Solanki, “Designing and characterization of a highly sensitive and selective biosensing platform for ciprofloxacin detection utilizing lanthanum oxide nanoparticles,” *Journal of Environmental Chemical Engineering*, vol. 9, no. 6, p. 106771, Nov. 2021, doi: 10.1016/j.jece.2021.106771.
[32] E. V. Bizina, O. V. Farafonova, N. I. Zolotareva, S. S. Grazhulene, and T. N. Ermolaeva, “A piezoelectric immunosensor based on magnetic carbon nanocomposites for the determination of ciprofloxacin,” *Journal of Analytical Chemistry*, vol. 77, no. 4, pp. 458–465, Apr. 2022, doi: 10.1134/s1061934822040049.
[33] Y. Cheng *et al.*, “Reusable smartphone-facilitated mobile fluorescence biosensor for rapid and sensitive on-site quantitative detection of trace pollutants,” *Biosensors and Bioelectronics*, vol. 199, p. 113863, Dec. 2021, doi: 10.1016/j.bios.2021.113863.
[34] Z. Zhang, Y. Cong, Y. Huang, and X. Du, “Nanomaterials-Based electrochemical immunosensors,” *Micromachines*, vol. 10, no. 6, p. 397, Jun. 2019, doi: 10.3390/mi10060397.
[35] A. Idili, J. Gerson, C. Parolo, T. Kippin, and K. W. Plaxco, “An electrochemical aptamer-based sensor for the rapid and convenient measurement of l-tryptophan,” *Analytical and Bioanalytical Chemistry*, vol. 411, no. 19, pp. 4629–4635, Feb. 2019, doi: 10.1007/s00216-019-01645-0.
[36] W. Putzbach and N. Ronkainen, “Immobilization techniques in the fabrication of Nanomaterial-Based Electrochemical Biosensors: a review,” *Sensors*, vol. 13, no. 4, pp. 4811–4840, Apr. 2013, doi: 10.3390/s130404811.
[37] Z. Yan *et al.*, “Fluorescent aptasensor for ofloxacin detection based on the aggregation of gold nanoparticles and its effect on quenching the fluorescence of Rhodamine B,” *Spectrochimica*

Acta Part a Molecular and Biomolecular Spectroscopy, vol. 221, p. 117203, May 2019, doi: 10.1016/j.saa.2019.117203.
[38] S. M. T. Heidarian *et al.*, "A novel electrochemical approach for the ultrasensitive detection of fluoroquinolones based on a double-labelled aptamer to surpass complementary strands of aptamer lying flat," *Sensors and Actuators B Chemical*, vol. 334, p. 129632, Feb. 2021, doi: 10.1016/j.snb.2021.129632.
[39] E. Esen, İ. Yazgan, and D. O. Demirkol, "Bienzymatic fluorescence detection based on paraoxonase and laccase on anthracene-sequestered polyamic acid films: A novel approach for inhibition-based sensors," *Materials Today Communications*, vol. 25, p. 101672, Sep. 2020, doi: 10.1016/j.mtcomm.2020.101672.
[40] A. R. Cardoso, L. P. T. Carneiro, G. Cabral-Miranda, M. F. Bachmann, and M. G. F. Sales, "Employing bacteria machinery for antibiotic detection: Using DNA gyrase for ciprofloxacin detection," *Chemical Engineering Journal*, vol. 409, p. 128135, Dec. 2020, doi: 10.1016/j.cej.2020.128135.
[41] S. Sivaselvam, R. S. Anjana, N. S. Dhujana, M. Victor, and R. S. Jayasree, "Nitrogen-doped carbon dots: a novel biosensing platform for selective norfloxacin detection and bioimaging," *Journal of Materials Chemistry B*, vol. 12, no. 31, pp. 7635–7645, Jan. 2024, doi: 10.1039/d4tb01006j.
[42] X. Liu *et al.*, "A novel biosensor based on antibody controlled isothermal strand displacement amplification (ACISDA) system," *Biosensors and Bioelectronics*, vol. 209, p. 114185, Apr. 2022, doi: 10.1016/j.bios.2022.114185.
[43] N. Chaudhary, A. K. Yadav, J. G. Sharma, and P. R. Solanki, "Designing and characterization of a highly sensitive and selective biosensing platform for ciprofloxacin detection utilizing lanthanum oxide nanoparticles," *Journal of Environmental Chemical Engineering*, vol. 9, no. 6, p. 106771, Nov. 2021, doi: 10.1016/j.jece.2021.106771.
[44] Y. Cheng *et al.*, "Reusable smartphone-facilitated mobile fluorescence biosensor for rapid and sensitive on-site quantitative detection of trace pollutants," *Biosensors and Bioelectronics*, vol. 199, p. 113863, Dec. 2021, doi: 10.1016/j.bios.2021.113863.
[45] E. V. Bizina, O. V. Farafonova, N. I. Zolotareva, S. S. Grazhulene, and T. N. Ermolaeva, "A piezoelectric immunosensor based on magnetic carbon nanocomposites for the determination of ciprofloxacin," *Journal of Analytical Chemistry*, vol. 77, no. 4, pp. 458–465, Apr. 2022, doi: 10.1134/s1061934822040049.
[46] Z. Yan *et al.*, "Fluorescent aptasensor for ofloxacin detection based on the aggregation of gold nanoparticles and its effect on quenching the fluorescence of Rhodamine B," *Spectrochimica Acta Part a Molecular and Biomolecular Spectroscopy*, vol. 221, p. 117203, May 2019, doi: 10.1016/j.saa.2019.117203.
[47] S. M. T. Heidarian *et al.*, "A novel electrochemical approach for the ultrasensitive detection of fluoroquinolones based on a double-labelled aptamer to surpass complementary strands of aptamer lying flat," *Sensors and Actuators B Chemical*, vol. 334, p. 129632, Feb. 2021, doi: 10.1016/j.snb.2021.129632.
[48] E. Esen, İ. Yazgan, and D. O. Demirkol, "Bienzymatic fluorescence detection based on paraoxonase and laccase on anthracene-sequestered polyamic acid films: A novel approach for inhibition-based sensors," *Materials Today Communications*, vol. 25, p. 101672, Sep. 2020, doi: 10.1016/j.mtcomm.2020.101672.
[49] A. R. Cardoso, L. P. T. Carneiro, G. Cabral-Miranda, M. F. Bachmann, and M. G. F. Sales, "Employing bacteria machinery for antibiotic detection: Using DNA gyrase for ciprofloxacin detection," *Chemical Engineering Journal*, vol. 409, p. 128135, Dec. 2020, doi: 10.1016/j.cej.2020.128135.
[50] M. Yang *et al.*, "Convenient and sensitive detection of norfloxacin with fluorescent carbon dots," *Journal of Materials Chemistry B*, vol. 2, no. 45, pp. 7964–7970, Oct. 2014, doi: 10.1039/c4tb01385a.
[51] F. Wang, L. Zhu, and J. Zhang, "Electrochemical sensor for levofloxacin based on molecularly imprinted polypyrrole–graphene–gold nanoparticles modified electrode," *Sensors and Actuators B Chemical*, vol. 192, pp. 642–647, Nov. 2013, doi: 10.1016/j.snb.2013.11.037.
[52] O. T. Vu *et al.*, "Highly sensitive molecularly imprinted Polymer-Based electrochemical sensors enhanced by gold nanoparticles for norfloxacin detection in aquaculture water," *ACS Omega*, vol. 8, no. 3, pp. 2887–2896, Jan. 2023, doi: 10.1021/acsomega.2c04414.
[53] M. Zamani, C. M. Klapperich, and A. L. Furst, "Recent advances in gold electrode fabrication for low-resource setting biosensing," *Lab on a Chip*, vol. 23, no. 5, pp. 1410–1419, Jan. 2023, doi: 10.1039/d2lc00552b.

[54] R. Islam, H. T. L. Luu, and S. Kuss, “Review—Electrochemical Approaches and Advances towards the Detection of Drug Resistance,” *Journal of the Electrochemical Society*, vol. 167, no. 4, p. 045501, Feb. 2020, doi: 10.1149/1945-7111/ab6ff3.
[55] Z. Ye, L. Wang, and J. Wen, “A simple and sensitive method for determination of Norfloxacin in pharmaceutical preparations,” *Brazilian Journal of Pharmaceutical Sciences*, vol. 51, no. 2, pp. 429–437, Jun. 2015, doi: 10.1590/s1984-82502015000200020.
[56] Z. Liu *et al.*, “High-sensitive electrochemical sensor for determination of Norfloxacin and its metabolism using MWCNT-CPE/pRGO-ANSA/Au,” *Sensors and Actuators B Chemical*, vol. 257, pp. 1065–1075, Nov. 2017, doi: 10.1016/j.snb.2017.11.052.
[57] Y. Zhang *et al.*, “Selective detection of norfloxacin using MIP/PEDOT modified electrode: A study on sensing performance,” *Composites Part B Engineering*, vol. 279, p. 111432, Apr. 2024, doi: 10.1016/j.compositesb.2024.111432.
[58] C. Zhang and X. Du, “Electrochemical sensors based on carbon nanomaterial used in diagnosing metabolic disease,” *Frontiers in Chemistry*, vol. 8, Aug. 2020, doi: 10.3389/fchem.2020.00651.
[59] S. M. M. Morsi, M. E. A. El-Aziz, and H. A. Mohamed, “Smart polymers as molecular imprinted polymers for recognition of target molecules,” *International Journal of Polymeric Materials*, vol. 72, no. 8, pp. 612–635, Feb. 2022, doi: 10.1080/00914037.2022.2042287.
[60] E. Mervinetsky *et al.*, “Copper induced conformational changes of tripeptide monolayer based impedimetric biosensor,” *Scientific Reports*, vol. 7, no. 1, Aug. 2017, doi: 10.1038/s41598-017-10288-z.
[61] Y. Song, J. Qiao, W. Liu, and L. Qi, “Norfloxacin detection based on the peroxidase-like activity enhancement of gold nanoclusters,” *Analytical and Bioanalytical Chemistry*, vol. 413, no. 4, pp. 979–985, Nov. 2020, doi: 10.1007/s00216-020-03056-y.
[62] E. Trofimchuk, A. Nilghaz, S. Sun, and X. Lu, “Determination of norfloxacin residues in foods by exploiting the coffee-ring effect and paper-based microfluidics device coupling with smartphone-based detection,” *Journal of Food Science*, vol. 85, no. 3, pp. 736–743, Feb. 2020, doi: 10.1111/1750-3841.15039.
[63] C. Eboka, “Colorimetric determination of the fluoroquinolones,” *Journal of Antimicrobial Chemotherapy*, vol. 39, no. 5, pp. 639–641, May 1997, doi: 10.1093/jac/39.5.639.
[64] C. Cardozo, I. D. B. Segundo, E. R. V. P. Galvão, D. R. Da Silva, E. V. D. Santos, and C. A. Martínez-Huitle, “Decentralized environmental applications of a smartphone-based method for chemical oxygen demand and color analysis,” *Scientific Reports*, vol. 13, no. 1, Jul. 2023, doi: 10.1038/s41598-023-37126-9.
[65] D. R. Wijesinghe, M. A. Zobair, and M. Esmaeelpour, “A review on Photoacoustic spectroscopy Techniques for gas sensing,” *Sensors*, vol. 24, no. 20, p. 6577, Oct. 2024, doi: 10.3390/s24206577.
[66] P. N. S. B. S. V. Prasad V., A. H. Syed, M. Himansh, B. Jana, P. Mandal, and P. K. Sanki, “Augmenting authenticity for non-invasive in vivo detection of random blood glucose with photoacoustic spectroscopy using Kernel-based ridge regression,” *Scientific Reports*, vol. 14, no. 1, Apr. 2024, doi: 10.1038/s41598-024-53691-z.
[67] Y. Song, S. M. Park, Y. Jeong, J. Kim, and H. Lee, “Review on multispectral photoacoustic imaging using stimulated Raman scattering light sources,” *Sensors*, vol. 25, no. 11, p. 3325, May 2025, doi: 10.3390/s25113325.
[68] M. Ferris and G. Zabow, “Quantitative, high-sensitivity measurement of liquid analytes using a smartphone compass,” *Nature Communications*, vol. 15, no. 1, Mar. 2024, doi: 10.1038/s41467-024-47073-2.
[69] F. Lin *et al.*, “Smart cellulose-derived magnetic hydrogel with rapid swelling and deswelling properties for remotely controlled drug release,” *Cellulose*, vol. 26, no. 11, pp. 6861–6877, Jun. 2019, doi: 10.1007/s10570-019-02572-0.
[70] J. Hwang, Y. H. Cho, M. S. Park, and B. H. Kim, “Microchannel fabrication on glass materials for microfluidic devices,” *International Journal of Precision Engineering and Manufacturing*, vol. 20, no. 3, pp. 479–495, Mar. 2019, doi: 10.1007/s12541-019-00103-2.
[71] X. Han *et al.*, “Polymer-based microfluidic devices: A comprehensive review on preparation and applications,” *Polymer Engineering and Science*, vol. 62, no. 1, pp. 3–24, Nov. 2021, doi: 10.1002/pen.25831.
[72] A. Shakeri, N. A. Jarad, S. Khan, and T. F. Didar, “Bio-functionalization of microfluidic platforms made of thermoplastic materials: A review,” *Analytica Chimica Acta*, vol. 1209, p. 339283, Nov. 2021, doi: 10.1016/j.aca.2021.339283.

[73] Y.-S. Lin, C.-H. Yang, C.-Y. Wang, F.-R. Chang, K.-S. Huang, and W.-C. Hsieh, "An aluminum microfluidic chip fabrication using a convenient micromilling process for fluorescent Poly(DL-lactide-co-glycolide) microparticle generation," *Sensors*, vol. 12, no. 2, pp. 1455–1467, Feb. 2012, doi: 10.3390/s120201455.
[74] J. Finkensieper *et al.*, "Apicomplexan parasites are attenuated by low-energy electron irradiation in an automated microfluidic system and protect against infection with Toxoplasma gondii," *Parasitology Research*, vol. 122, no. 8, pp. 1819–1832, May 2023, doi: 10.1007/s00436-023-07880-w.
[75] J. B. Nielsen et al., "Microfluidics: innovations in materials and their fabrication and functionalization," Anal. Chem., vol. 92, no. 1, pp. 150–168, Jan. 2020. doi: 10.1021/acs.analchem.
[76] F. Alghannam *et al.*, "Recent progress in PDMS-Based microfluidics toward integrated Organ-on-a-Chip biosensors and personalized medicine," *Biosensors*, vol. 15, no. 2, p. 76, Jan. 2025, doi: 10.3390/bios15020076.
[77] R. Ecker, T. Mitteramskogler, A. Fuchsluger, and B. Jakoby, "Fabrication of an ultrathin PMMA foil for sensing applications in microfluidic systems," *Proceedings*, vol. 97, p. 48, 2024. doi: 10.3390/proceedings2024097048.
[78] M. Boodaghi and A. Shamloo, "A comparison of different geometrical elements to model fluid wicking in paper-based microfluidic devices," *AIChE Journal*, vol. 66, no. 1, Aug. 2019, doi: 10.1002/aic.16756.
[79] Y. Wang, S. Chen, H. Sun, W. Li, C. Hu, and K. Ren, "Recent progresses in microfabricating perfluorinated polymers (Teflons) and the associated new applications in microfluidics," *Microphysiological Systems*, vol. 1, p. 1, Jan. 2018, doi: 10.21037/mps.2018.08.02.
[80] A. Agha *et al.*, "A review of cyclic olefin copolymer applications in microfluidics and microdevices," *Macromolecular Materials and Engineering*, vol. 307, no. 8, Apr. 2022, doi: 10.1002/mame.202200053.
[81] A. Clancy *et al.*, "Hydrogel-based microfluidic device with multiplexed 3D in vitro cell culture," *Scientific Reports*, vol. 12, no. 1, Oct. 2022, doi: 10.1038/s41598-022-22439-y.
[82] S. Nishat, A. T. Jafry, A. W. Martinez, and F. R. Awan, "Paper-based microfluidics: Simplified fabrication and assay methods," *Sensors and Actuators B Chemical*, vol. 336, p. 129681, Feb. 2021, doi: 10.1016/j.snb.2021.129681.
[83] S. Kumar, J. B. Kaushal, and H. P. Lee, "Sustainable Sensing with Paper Microfluidics: Applications in Health, Environment, and Food Safety," *Biosensors*, vol. 14, no. 6, p. 300, Jun. 2024, doi: 10.3390/bios14060300.
[84] Q. Chen, G. Li, Y. Nie, S. Yao, and J. Zhao, "Investigation and improvement of reversible microfluidic devices based on glass–PDMS–glass sandwich configuration," *Microfluidics and Nanofluidics*, vol. 16, no. 1–2, pp. 83–90, Jun. 2013, doi: 10.1007/s10404-013-1222-9.
[85] S. P. Kojic, G. M. Stojanovic, and V. Radonic, "Novel Cost-Effective microfluidic chip based on hybrid fabrication and its comprehensive characterization," *Sensors*, vol. 19, no. 7, p. 1719, Apr. 2019, doi: 10.3390/s19071719.
[86] B. K. Gale *et al.*, "A review of current methods in microfluidic device fabrication and future commercialization prospects," *Inventions*, vol. 3, no. 3, p. 60, Aug. 2018, doi: 10.3390/inventions3030060.
[87] S. Scott and Z. Ali, "Fabrication Methods for Microfluidic devices: An Overview," *Micromachines*, vol. 12, no. 3, p. 319, Mar. 2021, doi: 10.3390/mi12030319.
[88] P. Kim et al., "Soft lithography for microfluidics: A review," *Lab Chip*, vol. 8, pp. 2189–2197, 2008.
[89] L. Zhang, W. Wang, X.-J. Ju, R. Xie, Z. Liu, and L.-Y. Chu, "Fabrication of glass-based microfluidic devices with dry film photoresists as pattern transfer masks for wet etching," *RSC Advances*, vol. 5, no. 8, pp. 5638–5646, Dec. 2014, doi: 10.1039/c4ra15907a.
[90] M. Huff, "Recent advances in reactive ion etching and applications of High-Aspect-Ratio microfabrication," *Micromachines*, vol. 12, no. 8, p. 991, Aug. 2021, doi: 10.3390/mi12080991.
[91] D. K. Mishra, J. Arab, K. Pawar, and P. Dixit, "Fabrication of Deep Microfeatures in Glass Substrate using Electrochemical Discharge Machining for Biomedical and Microfluidic Applications," *In Proc. IEEE EPTC*, pp. 263–266, Dec. 2019, doi: 10.1109/eptc47984.2019.9026714.
[92] M. J. C. Modarelli, D. M. Kot-Thompson, and K. Hoshino, "5-axis CNC micro-milling machine for three-dimensional microfluidics," *Lab on a Chip*, Nov. 2024, doi: 10.1039/d4lc00496e.
[93] Max, "Micro Milling: principal, tools, application, key consideration, and future trend," *Proleantech | Custom Parts On-Demand*, Sep. 04, 2024. https://proleantech.com/micro-milling/

[94] S. Shahriari, V. Patel, and P. R. Selvaganapathy, “Xurography as a tool for fabrication of microfluidic devices,” *Journal of Micromechanics and Microengineering*, vol. 33, no. 8, p. 083002, Jun. 2023, doi: 10.1088/1361-6439/ace05d.
[95] U. N. Lee *et al.*, “Fundamentals of rapid injection molding for microfluidic cell-based assays,” *Lab on a Chip*, vol. 18, no. 3, pp. 496–504, Jan. 2018, doi: 10.1039/c7lc01052d.
[96] S. H. Ng and Z. F. Wang, “Hot roller embossing for microfluidics: process and challenges,” *Microsystem Technologies*, vol. 15, no. 8, pp. 1149–1156, Oct. 2008, doi: 10.1007/s00542-008-0722-0.
[97] D. Patil, A. Sharma, S. Aravindan, and P. V. Rao, “Development of hot embossing setup and fabrication of ordered nanostructures on large area of polymer surface for antibiofouling application,” *Micro & Nano Letters*, vol. 14, no. 2, pp. 191–195, Oct. 2018, doi: 10.1049/mnl.2018.5462.
[98] P. Kim et al., “Soft lithography for microfluidics: A review,” *Lab Chip*, vol. 8, pp. 2189–2197, 2008.
[99] J. Ma, L. Jiang, X. Pan, H. Ma, B. Lin, and J. Qin, “A simple photolithography method for microfluidic device fabrication using sunlight as UV source,” *Microfluidics and Nanofluidics*, vol. 9, no. 6, pp. 1247–1252, May 2010, doi: 10.1007/s10404-010-0630-3.
[100] Y. Ma, J. Thiele, L. Abdelmohsen, J. Xu, and W. T. S. Huck, “Biocompatible macro-initiators controlling radical retention in microfluidic on-chip photo-polymerization of water-in-oil emulsions,” *Chemical Communications*, vol. 50, no. 1, pp. 112–114, Nov. 2013, doi: 10.1039/c3cc46733c.
[101] Gomez, I. Goenaga, I. Lizuain, and M. Ozaita, “Femtosecond laser ablation for microfluidics,” *Optical Engineering*, vol. 44, no. 5, p. 051105, May 2005, doi: 10.1117/1.1902783.
[102] K. Sugioka *et al.*, “Femtosecond laser 3D micromachining: a powerful tool for the fabrication of microfluidic, optofluidic, and electrofluidic devices based on glass,” *Lab on a Chip*, vol. 14, no. 18, pp. 3447–3458, Jan. 2014, doi: 10.1039/c4lc00548a.
[103] Y. T. Kim, A. Ahmadianyazdi, and A. Folch, “A ‘print–pause–print’ protocol for 3D printing microfluidics using multimaterial stereolithography,” *Nature Protocols*, vol. 18, no. 4, pp. 1243–1259, Jan. 2023, doi: 10.1038/s41596-022-00792-6.
[104] H. J. McLennan *et al.*, “Nano-liter perfusion microfluidic device made entirely by two-photon polymerization for dynamic cell culture with easy cell recovery,” *Scientific Reports*, vol. 13, no. 1, Jan. 2023, doi: 10.1038/s41598-023-27660-x.
[105] F. Chen and J. R. V. De Aldana, “Direct femtosecond laser writing of optical waveguides in dielectrics,” in *Springer series in materials science*, 2020, pp. 185–210. doi: 10.1007/978-3-030-59313-1_6.
[106] A. D. Castiaux, C. W. Pinger, E. A. Hayter, M. E. Bunn, R. S. Martin, and D. M. Spence, “PolyJet 3D-Printed Enclosed Microfluidic Channels without Photocurable Supports,” *Analytical Chemistry*, vol. 91, no. 10, pp. 6910–6917, Apr. 2019, doi: 10.1021/acs.analchem.9b01302.
[107] N. P. Macdonald, J. M. Cabot, P. Smejkal, R. M. Guijt, B. Paull, and M. C. Breadmore, “Comparing microfluidic performance of Three-Dimensional (3D) printing platforms,” *Analytical Chemistry*, vol. 89, no. 7, pp. 3858–3866, Mar. 2017, doi: 10.1021/acs.analchem.7b00136.
[108] “Fused Deposition Modeling (FDM),” *Additive Manufacturing Facility (AMF) | UZH*. https://www.amf.uzh.ch/en/additive-manufacturing/our_technologies/fdm.html.
[109] M. Abdelgawad and A. R. Wheeler, “Low-cost, rapid-prototyping of digital microfluidics devices,” *Microfluidics and Nanofluidics*, vol. 4, no. 4, pp. 349–355, Jul. 2007, doi: 10.1007/s10404-007-0190-3.
[110] E. Samiei, M. Tabrizian, and M. Hoorfar, “A review of digital microfluidics as portable platforms for lab-on-a-chip applications,” *Lab Chip*, vol. 16, no. 13, pp. 2376–2396, 2016. doi: 10.1039/C6LC00387G.
[111] MSHT, “Basics of Electrowetting-on-Dielectric (EWOD),” online. Aug. 1, 2025. Accessed: Aug. 1, 2025. Available: https://msht.utdallas.edu/Pages/EWOD_Basics.html.
[112] MSHT, “Basics of Electrowetting-on-Dielectric (EWOD),” online. Aug. 17, 2025. Accessed: Aug. 17, 2025. Available: https://msht.utdallas.edu/Pages/EWOD_Basics.html.
[113] P. M. Tavares, M. H. De Sá, and M. G. F. Sales, “Innovative screen-printed electrodes on cork composite substrates applied to sulfadiazine electrochemical sensing,” *Journal of Electroanalytical Chemistry*, vol. 880, p. 114922, Dec. 2020, doi: 10.1016/j.jelechem.2020.114922.
[114] D. Stan *et al.*, “What is the optimal method for cleaning Screen-Printed electrodes?,” *Processes*, vol. 10, no. 4, p. 723, Apr. 2022, doi: 10.3390/pr10040723.

[115] Mohan and V. Kumar, “Ion-selective electrodes based on PVC membranes for potentiometric sensor applications: A review,” *Int. J. Membr. Sci. Technol.*, vol. 8, no. 2, pp. 76–84, 2021. doi: 10.15379/2410-1869.2021.08.02.06.
[116] H. Da Silva, J. Pacheco, J. Silva, S. Viswanathan, and C. Delerue-Matos, “Molecularly imprinted sensor for voltammetric detection of norfloxacin,” *Sensors and Actuators B Chemical*, vol. 219, pp. 301–307, May 2015, doi: 10.1016/j.snb.2015.04.125.
[117] D. C. G. Bedor *et al.*, “Development and validation of a new method for the quantification of norfloxacin by HPLC-UV and its application to a comparative pharmacokinetic study in human volunteers,” *Revista Brasileira De Ciências Farmacêuticas*, vol. 43, no. 2, pp. 231–238, Jun. 2007, doi: 10.1590/s1516-93322007000200009.
[118] S. Sahoo, C. K. Chakraborti, P. K. Behera, and S. C. Mishra, “SPECTROSCOPIC INVESTIGATIONS OF A CONTROLLED RELEASE MUCOADHESIVE SUSPENSION,” *J. Pharm. Anal*, vol. 1, no. 4, pp. 280–285, Jan. 2011, [Online]. Available: http://dspace.nitrkl.ac.in:8080/dspace/handle/2080/1582
[119] K. Arshak, V. Velusamy, O. Korostynska, K. Oliwa-Stasiak, and C. Adley, “Conducting polymers and their applications to biosensors: emphasizing on foodborne pathogen detection,” *IEEE Sensors Journal*, vol. 9, no. 12, pp. 1942–1951, Nov. 2009, doi: 10.1109/jsen.2009.2032052.
[120] D. C. G. Bedor *et al.*, “Development and validation of a new method for the quantification of norfloxacin by HPLC-UV and its application to a comparative pharmacokinetic study in human volunteers,” *Revista Brasileira De Ciências Farmacêuticas*, vol. 43, no. 2, pp. 231–238, Jun. 2007, doi: 10.1590/s1516-93322007000200009.
[121] X. Lai, Y. Sun, M. Yang, and H. Wu, “Rubik’s Cube as reconfigurable microfluidic platform for rapid setup and switching of analytical devices,” *Micromachines*, vol. 13, no. 12, p. 2054, Nov. 2022, doi: 10.3390/mi13122054.
[122] L. V. De Souza Santos, A. M. Meireles, and L. C. Lange, “Degradation of antibiotics norfloxacin by Fenton, UV and UV/H2O2,” *Journal of Environmental Management*, vol. 154, pp. 8–12, Feb. 2015, doi: 10.1016/j.jenvman.2015.02.021.
[123] A. Babuponnusami and K. Muthukumar, “A review on Fenton and improvements to the Fenton process for wastewater treatment,” *Journal of Environmental Chemical Engineering*, vol. 2, no. 1, pp. 557–572, Oct. 2013, doi: 10.1016/j.jece.2013.10.011.
[124] “Infineon, “XENSIV PAS CO_2 Sensor2Go GUI,” online. Jul. 10, 2025. Accessed: Jul. 10, 2025. Available: https://softwaretools.infineon.com/tools/com.ifx.tb.tool.ifxpasco2gui.
[125] Charles Labs, “Microfluidics Electrowetting platform,” online. Jul. 25, 2025. Accessed: Jul. 25, 2025. Available: https://charleslabs.fr/en/project-Microfluidics+Electrowetting+platform
[126] I. Anshori *et al.*, “Versatile and Low-Cost fabrication of modular Lock-and-Key microfluidics for integrated connector mixer using a stereolithography 3D printing,” *Micromachines*, vol. 13, no. 8, p. 1197, Jul. 2022, doi: 10.3390/mi13081197.
[127] M. Vaz and L. Kumar, “3D printing as a promising tool in personalized medicine,” *AAPS PharmSciTech*, vol. 22, no. 1, Jan. 2021, doi: 10.1208/s12249-020-01905-8.
[128] T.-J. Chang *et al.*, “Micro and nanoscale 3D printing using optical pickup unit from a gaming console,” *Communications Physics*, vol. 4, no. 1, Feb. 2021, doi: 10.1038/s42005-021-00532-4.
[129] H. Felton, R. Hughes, and A. Diaz-Gaxiola, “Negligible-cost microfluidic device fabrication using 3D-printed interconnecting channel scaffolds,” *PLoS ONE*, vol. 16, no. 2, p. e0245206, Feb. 2021, doi: 10.1371/journal.pone.0245206.
[130] LSR Propotype, “What is multi jet fusion?,” online. Aug. 5, 2025. Accessed: Aug. 5, 2025. Available: https://www.lsrpf.com/blog/what-is-multi-jet-fusion.
[131] S. M. Peltola, F. P. W. Melchels, D. W. Grijpma, and M. Kellomäki, “A review of rapid prototyping techniques for tissue engineering purposes,” *Annals of Medicine*, vol. 40, no. 4, pp. 268–280, Jan. 2008, doi: 10.1080/07853890701881788.
[132] FacFox, “Binder Jetting (BJ),” online. Aug. 5, 2025. Accessed: Aug. 5, 2025. Available: https://facfox.com/service/binder-jetting-bj/.
[133] Manufacturing Guide, “Direct Laser Metal Sintering, DMLS | Find suppliers, processes & material,” online. Aug. 5, 2025. Accessed: Aug. 5, 2025. Available: https://www.manufacturingguide.com/en/direct-laser-metal-sintering-dmls.
[134] Elexan Science, “CNC Machining Microfluidics: Milling a Microfluidic Droplet Generator Chip,” online. Aug. 5, 2025. Accessed: Aug. 5, 2025. Available: https://elexansci.com/blog/cnc-machining-microfluidics-milling-a-microfluidic-droplet-generator-chip/.

Appendices

Appendix A1. Electrochemical Cleaning of the WE

The cleaning of screen-printed electrodes (SPE), particularly the surface of the working electrode (WE), is a crucial step in ensuring signal quality, whether by increasing the active area or facilitating the immobilization of biomolecules involved in transduction. Therefore, this study aims to achieve a significant improvement in the electrochemical performance of the sensors through proper cleaning.

However, if the electrode surface is not thoroughly cleaned, unwanted peaks may appear in the voltammograms, indicating the presence of compounds still adsorbed on the electrode surface. In such cases, electrochemical cleaning should be repeated or supplemented with mechanical cleaning until the voltammograms confirm the complete absence of extra electrochemical peaks.

Electrochemical cleaning of SPEs, illustrated in Graph A1, leads to improved resolution of oxidation and reduction peaks, as evidenced by the narrowing of the corresponding potential peaks ($\Delta Ep \approx 0.3$ V). This behaviour indicates a significant modification of the sensor surface, positively impacting the quality and reliability of the electrochemical signals obtained.

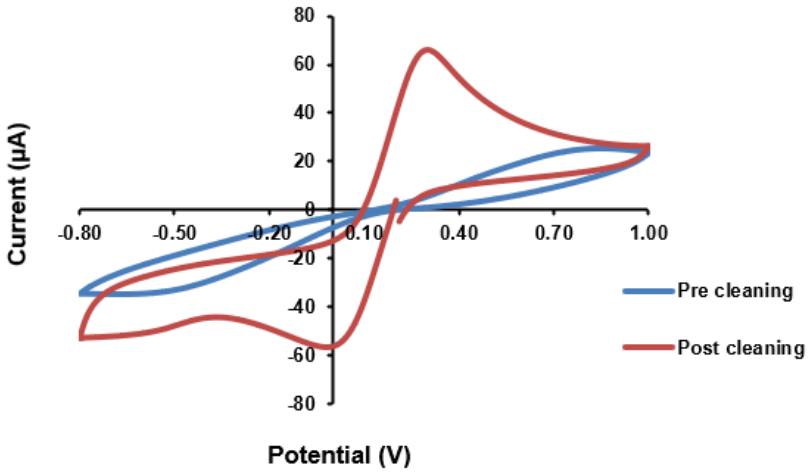

Graph A1 Electrochemical cleaning of carbon electrodes using a 0.5 mol/L H_2SO_4 solution. Experimental electrochemical results before and after the cleaning of a working electrode (WE) composed of five layers of carbon ink. Measurements were obtained by cyclic voltammetry (CV), using a 5.0 mmol/L $[Fe(CN)_6]^{3-/4-}$ redox solution (in 0.1 mol/L KCl), under the following conditions: 10 consecutive cycles; potential range from -0.8 V to 1.0 V; and a scan rate of 0.025 V/s.

Appendix A2. Characterization of Carbon Dots (CDs)

Appendix A2.1. Characterization of CDs

The nanomaterials were optically characterized by measuring their fluorescence properties using a Jasco fluorimeter, model FP 8650. Graph A2 shows the obtained emission and excitation spectra.

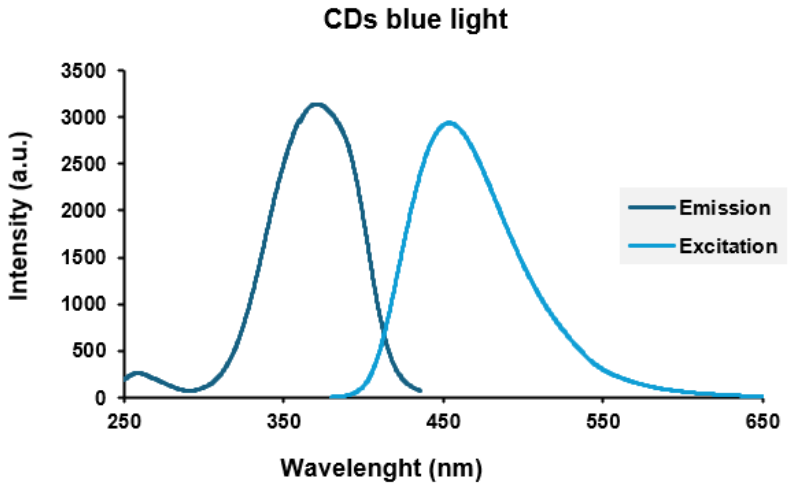

Graph A2 Characterization of CDs by fluorescence.

A close examination of the results revealed that the CDs absorb light strongly in the ultraviolet range, with a peak at 372nm. When excited at 458nm, they achieve their maximum emission spectrum.

Appendix A2.2. Modification of WEs with Carbon Dots (CDs)

After modifying the working electrode (WE) with 30 µL of the synthesized CDs solution, followed by electrochemical cleaning and incubation at 60°C for 60 minutes, a comparative analysis was conducted against the WE before modification with CDs, to assess the effect of these nanomaterials on the electrode surface. Indirect analysis was performed using a $[Fe(CN)_6]^{3-/4-}$ redox solution (CV: -0.8 V to 1.0 V; 10 consecutive cycles; 0.025 V/s). The results are in Graph A3 Graphical representation of the electrochemical results from the modification of a working electrode (WE) with CDs, incubated at 60 °C for 60 minutes on the electrode surface.

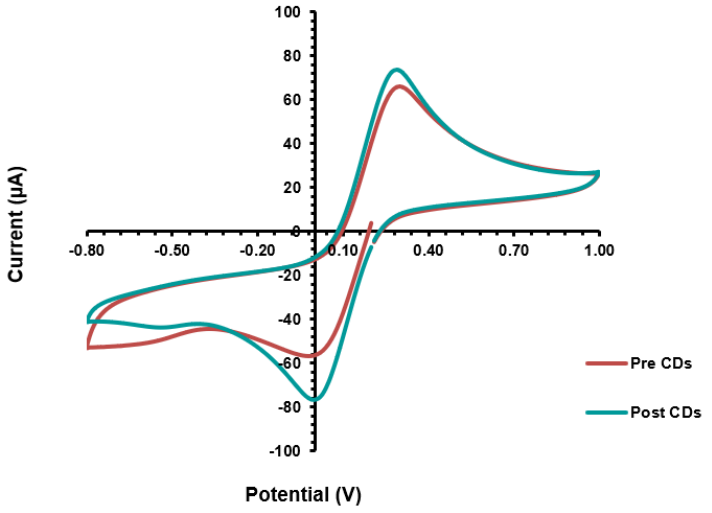

Graph A3 Graphical representation of the electrochemical results from the modification of a working electrode (WE) with CDs, incubated at 60 °C for 60 minutes on the electrode surface.

The incorporation of the CDs notably elevated the current signal, which strongly suggests that the electrochemical conductivity of the sensor improved. Curiously, however, the redox potential remained essentially constant, showing no significant shift when measured against the voltammogram recorded in the cleaning stage ($\Delta Ep \approx 0.3$ V).

These findings suggest that the CDs contribute to the current enhancement, possibly due to an increase in the electrode's active area and improved electron transfer, in agreement with reports in the literature.

Appendix A3. Complementary Microfluidic Transduction Modules

Colorimetric methodologies are common strategies for detecting antibiotic concentrations in water. For demonstration purposes, a preparation similar to that described in the colorimetric detection study of norfloxacin [62] was followed. The experimental protocol was adapted to a filter paper substrate, and the reading was performed using a photograph taken with a smartphone camera and processed computationally in Excel.

The experimental demonstration involved preparing the reaction on a filter paper substrate, such as Whatman #4 filters. The protocol we used is relatively straightforward;

we adapted it from an earlier study [62]. The core idea is simple mixing: we combine just 1 µL of a 0.15 M iron (III) nitrate nonahydrate solution with 20 µL of norfloxacin (NFX). Though the NFX volumes kept the same 1:20 volume ratio, we varied the NFX concentrations for each test [62]. The final solution was applied to filter paper, and subsequently, the paper with the colorimetric reaction assembly was placed in an oven at 45 °C for 10 minutes. This duration was determined to be sufficient for visual detection of the reaction on paper. Five minutes after removing the material from the oven, a color image was captured using an iPhone 15 camera, without flash, at an approximate distance of 10 cm. The images obtained from each paper represent the reaction between the iron solution and NFX solutions at different concentrations, as shown in Figure A1.

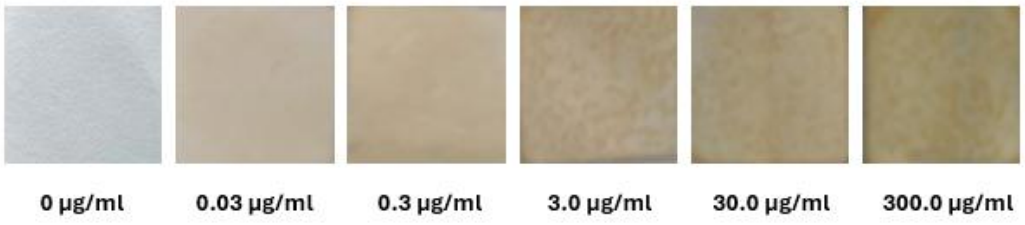

Figure A1 Photographic images from papers subjected to iron and norfloxacin reactions under varying concentrations.

The images are then processed in Excel and PowerPoint, where tools are used to evaluate the pixel intensities in the reaction zone, generating an RGB histogram (Red, Green, Blue) that represents the average of three points on the paper where the reaction coloration is observed. The average pixel intensity of the reaction zone is calculated and corrected by subtracting the average colour intensity of a non-reacted control well. By associating the average intensity value with the concentrations, a linear fit is obtained, as shown in Graph A4.

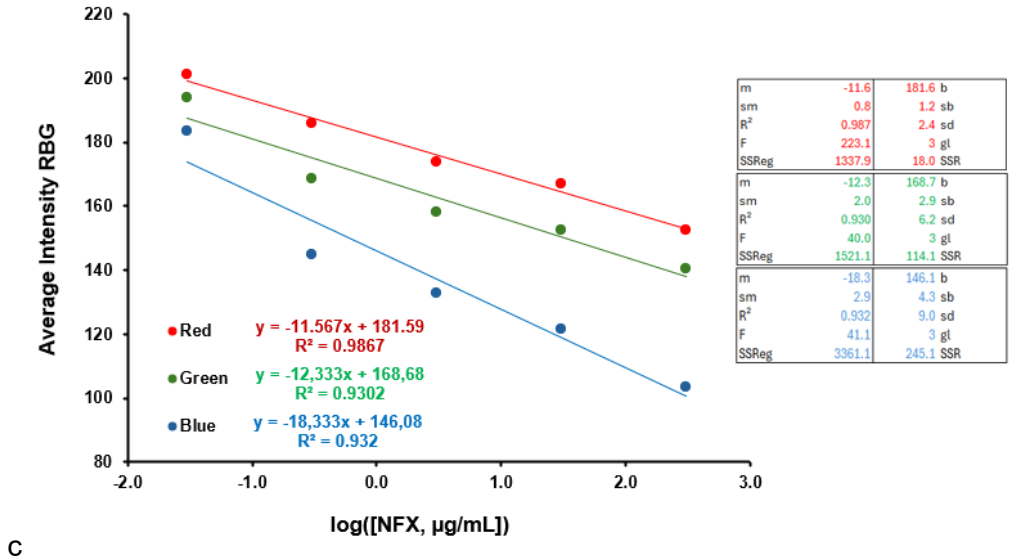

C

Graph A4 The graph presents the results of RGB analyses, where the logarithm of the concentration (log[NOR]) is plotted against the RGB colour coordinates.

The graph displays a linear reaction in which pixel intensity decreases as the concentration of NFX increases. This occurs because the yellow-orange coloration produced by the reaction absorbs more light at higher concentrations, resulting in lower pixel intensity readings by the camera.

The red curve shows the strongest linear correlation, indicating that the change in red pixel intensity is a more reliable indicator for quantifying NFX concentration in this system. Therefore, the method presents an interesting approach for qualitative assessments in terms of time and cost efficiency.

This work explored the photoacoustic effect to detect NFX concentration by indirectly evaluating the CO_2 ppm produced during Fenton degradation. This mechanism relies on the CO_2 generated when hydrogen peroxide and an iron source (Fe^{2+} or Fe^{3+}) react to create highly reactive hydroxyl radicals (·• OH) [122]. These radicals are highly reactive and capable of transforming organic molecules into simpler byproducts such as carbon dioxide, water, and inorganic ions. For norfloxacin degradation, iron (III) nitrate nonahydrate [$Fe(NO_3)_3 \cdot 9H_2O$] at 0.15 M and 30% hydrogen peroxide were used, along with NFX solutions at various concentrations. According to the literature, molar ratios of $Fe:H_2O_2$ between 1:5 and 1:10 are recommended for effective radical generation [123]. In this study, a 1:10 ratio was selected, where 10 µL of hydrogen peroxide was reacted with 65.27 µL of the iron compound. Norfloxacin was added to the 1:10 $Fe:H_2O_2$ solution at a fixed volume of 20 µL across different concentrations, to assess which solution, under fixed reagent conditions, would yield CO_2 in ppm.

The indirect reading of NFX concentration was performed using the XENSIV PAS CO_2 photoacoustic sensor from Infineon, illustrated in Figure A2 and Figure A3. Data processing can be done using software provided by the manufacturer, XENSIV PAS CO_2 Sensor2Go GUI, available for download from the company's website. This sensor is susceptible to CO_2 gas detection, utilizing a photoacoustic spectroscopy transduction mechanism. After CO_2 is released from NFX degradation, the gas enters the sensor through a hole in its surface. Inside the chamber, a modulated light beam passes through the gas and is absorbed by the gas molecules, causing periodic cycles of expansion and contraction. These generate pressure waves that are detected by a microphone within the chamber. The microphone produces CO_2 ppm curves that indicate the amount of CO_2 released during the Fenton degradation of the NFX-doped sample, providing an indirect correlation between NFX concentration and CO_2 output.

Figure A2 XENSIVPASCO2 photoacoustic sensor. Below the red circle, a hole serves as the access point for CO_2 gas after it is released from the degradation cell of the Fenton reaction. It is also important to highlight the presence of a complex signal amplification circuit integrated into the PCB associated with the sensor.

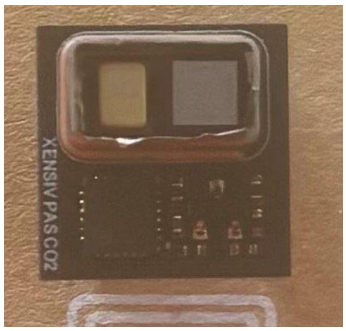

Figure A3 Visualization of transduction components with an infrared source (square-shaped component) on the right and a MEMS microphone (yellow rectangular component) on the left.

For evaluating photoacoustic transduction, our team selected the XENSIVPASCO2 sensor. The Infineon-manufactured transducer offers low power consumption, excellent sensitivity, and robust stability, enabling real-time data collection via a USB link to the computer. We gathered CO_2 ppm readings throughout a 5-minute incubation of the NFX solution mixed with the conjugated hydrogen peroxide and iron source inside the

microfluidic module. This specific 5-minute duration confirmed the reaction had ceased, as carbon dioxide bubbles were no longer observed escaping the photoacoustic reaction cell.

The CO_2 data came from the software of the Infineon company [124]. After adding iron and hydrogen peroxide to the norfloxacin solution, a five-minute pause allowed the reaction to finish. During this time, no CO_2 bubbles rose from the bottom of the cell, for each concentration of NFX, the five highest CO_2 ppm readings recorded by the sensor were averaged to obtain a representative value. A curve was plotted to link NFX concentration with CO_2 output. Graph A5 shows an exponential trend consistent with the data.

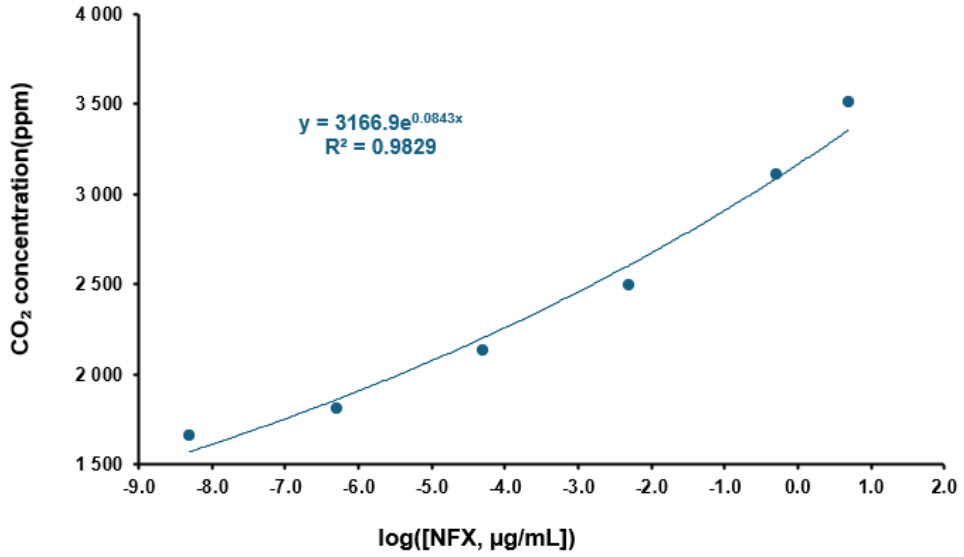

Graph A5 Exponential fit for calibration readings obtained from the photoacoustic sensor, indirectly correlating NFX concentration with CO_2 ppm detection.

For this data analysis, the regression fit yielded the equation $y = 3166.9e^{0.0843}x$ with an R^2 value of 0.9829. The Limit of Detection (LOD) and the Limit of Quantification (LOQ) were the same as those of the electrochemical sensor, equal to 0.005 pg/mL. This analysis reveals a promising mechanism for the quantitative measurement of NFX concentrations; however, further discussion is needed regarding which data should be used for calibration purposes. One may eventually acquire more CO_2 data points or consider other criteria such as distribution or standard deviation.

Appendix A4 Alternative/complementary transductions to the electrochemical detection of NFX

Appendix A4.1 Fluorescence System

Fluorescence and absorbance assays were conducted using a Jasco FP-8650 fluorimeter. This instrument provided both fluorescence spectra and absorbance readings for the samples. Each sample, with a total volume of 100 µL, consisted of a mixture of NFX and CD (carbon dot) solutions in a 2:1 volumetric ratio in acetate buffer.

The study investigated the quantification of NFX concentration using cumulative fluorescence, which combines the intrinsic fluorescence of norfloxacin with that of carbon dots. By analysing the combined fluorescence effects of both components, the experiment revealed a linear relationship between norfloxacin concentration and the fluorescence intensity of CDs in its presence. This approach emerged from the possibility of applying carbon dots, previously tested in electrochemical transduction, to a different modality, specifically fluorescence.

The cumulative fluorescence mechanism relies on interactions between the antibiotic molecules and the surfaces of the CDs. Norfloxacin contains functional groups such as C–F, C=O, C–N, and COOH, whereas the surface of CDs is rich in hydrophilic groups, including hydroxyl and carboxyl groups. Fluorescence arises from hydrogen bonding between these groups. When norfloxacin is added to the CD solution, strong hydrogen bonds between the two compounds passivate surface defects on the CDs, reducing non-radiative processes and enhancing quantum fluorescence efficiency. This increase in efficiency results in a greater light emission intensity.

After mixing CDs with NFX solutions at various concentrations in buffer, the fluorescence of NFX/CD samples was analysed using a spectrophotometer, as shown in Graph A6 and Graph A7. Calibration curves were generated for NFX in acetate buffer, both in the absence of NFX and in the NFX/CD combination, as illustrated in Graph A8.

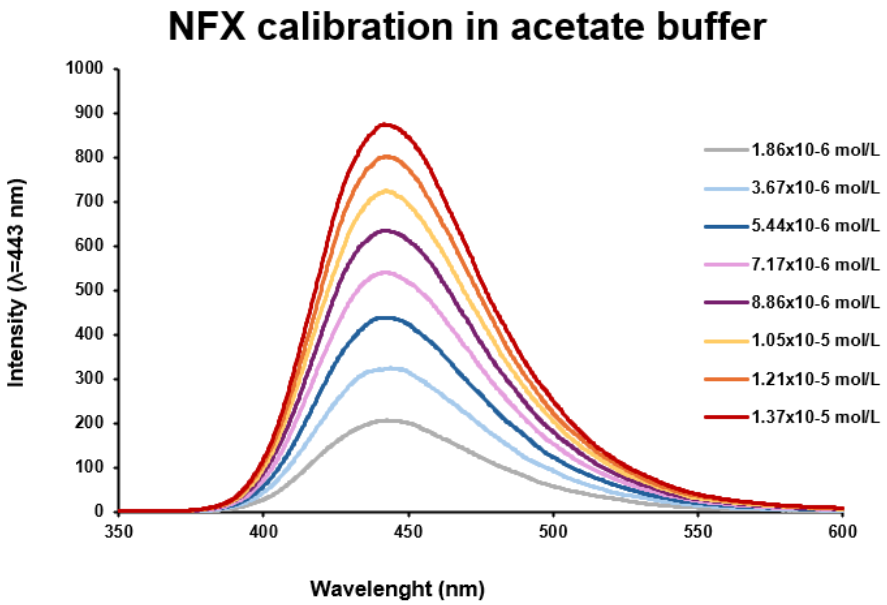

Graph A6 Absorbance of NFX solutions at different concentrations.

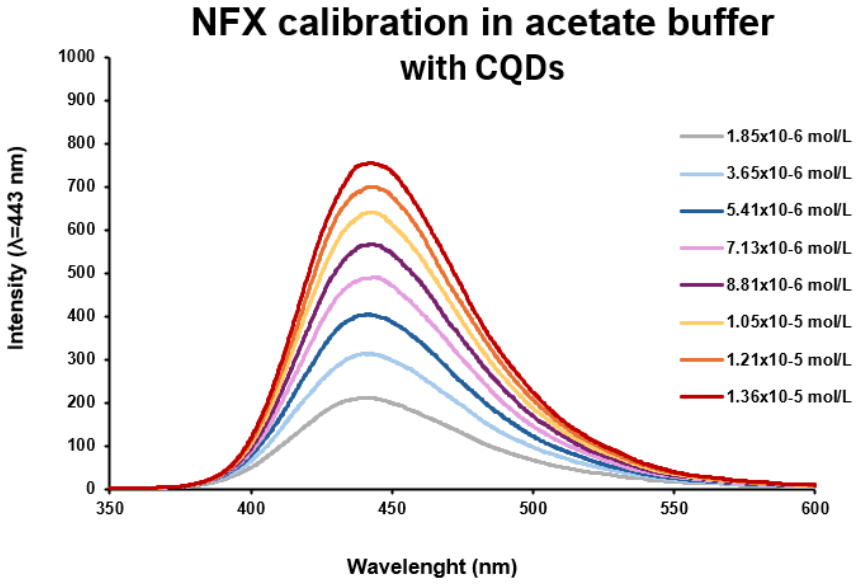

Graph A7 Absorbance of NFX/CD solutions at different NFX concentrations.

Graph A6 and Graph A7 illustrate the intrinsic fluorescence of norfloxacin, with a peak intensity detected at approximately 443 nm. Graph A8 presents the calibration of NFX in buffer with carbon dots (CDs), showing an apparent increase in fluorescence intensity as NFX concentration rises in the NFX+CDs solutions.

The calibration plots yield the following regression equations: for NFX in buffer without CDs, the equation is $y = 6.00 \times 10^7 x + 119.71$ with an R^2 of 0.9964; for NFX with CDs, the equation is $y = 5.00 \times 10^7 x + 145.49$ with an R^2 of 0.9946.

The key advantage of the NFX/CDs method lies in its ability to repurpose an electrochemical sensor, modified with carbon dots on its surface, for a different transduction mechanism that remains equally sensitive. However, measurements of norfloxacin without CDs also provide highly accurate concentration readings and are strongly recommended for samples requiring analysis at lower concentrations.

For these assays, the limits of detection (LOD) and quantification (LOQ) for norfloxacin with CDs were both 1.33×10^{-8} mol/L (4.25×10^{-3} µg/mL).

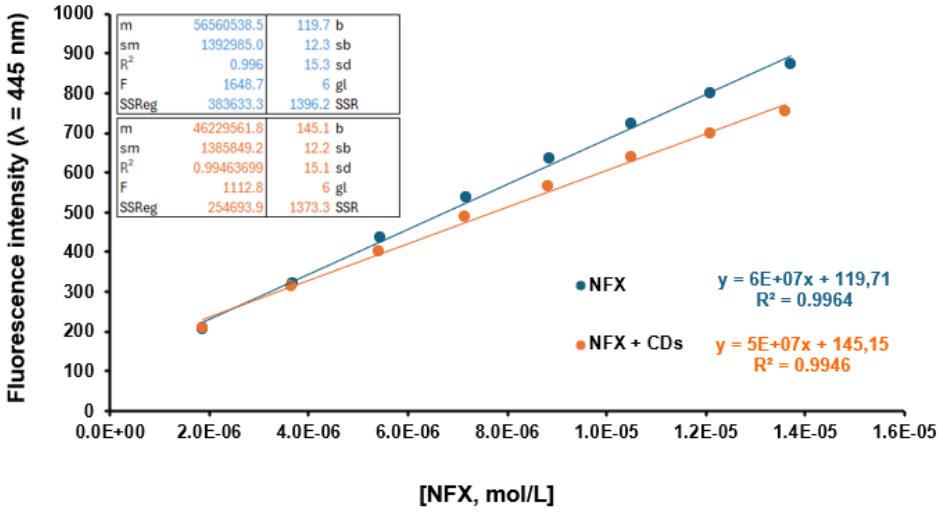

Graph A8 Calibration curves obtained for different concentrations of NFX and NFX/CDs based on fluorescence intensity detected at the wavelength of maximum absorbance (λ = 445 nm).

Appendix A4.2 Magnet-osmotic system transducer

One effective, low-cost transduction method with decent sensitivity relies on magneto-osmotic setups. To demonstrate this, we explored osmotic phenomena using hydrogels that are highly responsive to potential differences. The setup utilizes perfectly spherical sodium polyacrylate gels of equal size. Sodium polyacrylate is a polymer built from carboxylate groups (−COOH−). Once in water, these groups ionize. This ionization forces the polymer chains to repel and stretch. Simultaneously, water rushes into the structure via osmosis, triggering the swelling effect. Detecting NFX requires system adaptation. The simple principle is that varying NFX solutions automatically generate distinct osmotic gradients. These gradients influence how much the gel swells.

As a potent organic solute, NFX is crucial to the overall osmotic potential. High concentrations of NFX naturally reduce the osmotic potential difference between the gel sphere's internal and external environments. This reduced difference lessens the osmotic driving force, causing the gel to swell less. The reverse holds for low NFX concentrations. A much stronger osmotic gradient takes effect, which in turn triggers greater swelling of the gel spheres, a result vividly supported by Figure A4. In contrast, high-concentration NFX solutions produce a weaker gradient, resulting in less water absorption and a more subtle swelling effect, also illustrated in Figure A4. Beyond osmotic effects, NFX may interact with the polymer chains via functional group bonding, potentially limiting chain expansion and further reducing swelling at higher concentrations.

For the magneto-osmotic system, the team sourced sodium polyacrylate spheres from e-commerce platforms and selected only those with a diameter of 3 mm to ensure sample uniformity. The transduction process used a 3 mm N42 neodymium magnet purchased from Supermagnete.pt. A smartphone recorded the system's magnetic field data using the μMagnetometer app, which provides 3D magnetic field intensity components in microteslas (μT).

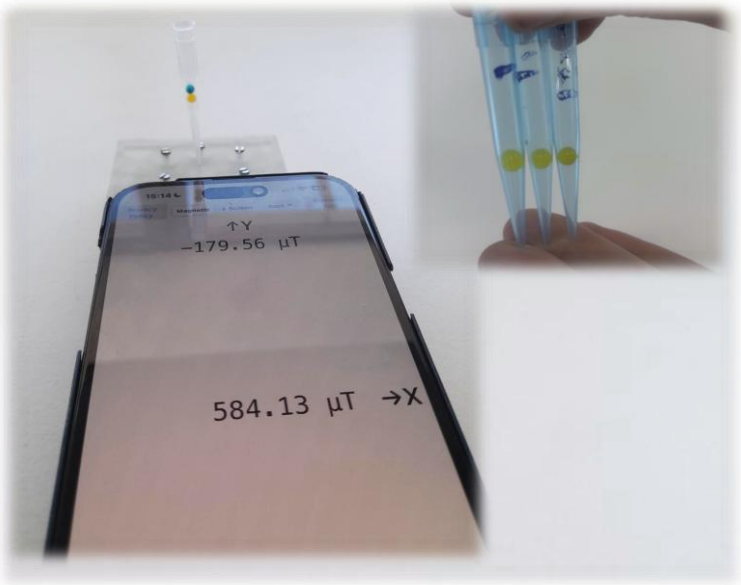

Figure A4 Magnetic spheres incubated in solutions with different NFX concentrations. From left to right, the incubations were performed in solutions with concentrations of 5.0×10^{-5} μg/mL, 5.0×10^{-3} μg/mL, and 5.0×10^{-1} μg/mL.

An apparent decrease in swelling is observed from the sphere incubated in the least concentrated solution to the most concentrated one. A key factor in the success of this transduction mechanism is maintaining a fixed distance between the sphere/magnet assembly and the smartphone, where the magnetometer is located. The neodymium

magnet rests just above the expanding/contracting gel sphere. This setup allows an external magnetometer to measure the resulting magnetic field, which, in turn, indirectly quantifies the distance between the magnet and the sensor after incubation (Magnetic field intensity (B) $\propto 1/r^3$). When placing the magnet on top of the sphere, the magnetometer behaves as follows: for larger spheres (lower NFX concentration), the distance between the magnet and the sensor increases if the sensor is positioned below the hydrogel or decreases if the sensor is placed above it. Thus, the sensor detects a weaker magnetic field when the hydrogel swells and the magnetometer sits beneath the sphere, and a stronger field when the magnetometer is positioned above the hydrogel. By collecting the magnetic field data recorded by the sensor at the end of incubation, it becomes possible to establish an indirect correlation between magnetic field intensity and NFX concentration.

To demonstrate this approach, the experiment used five NFX solutions with different concentrations. Five sodium polyacrylate spheres of equal diameter (3 mm) were incubated in these solutions for 25 minutes. After incubation, the spheres were placed in the setup with a fixed distance between the spheres and the magnetometer, which was positioned above the hydrogel spheres. Neodymium magnets, also 3 mm in diameter, were placed on top of the gel spheres, and the magnetometer measured the magnetic field. The linear fit correlating magnetic field intensity with NFX concentration appears in Graph A9.

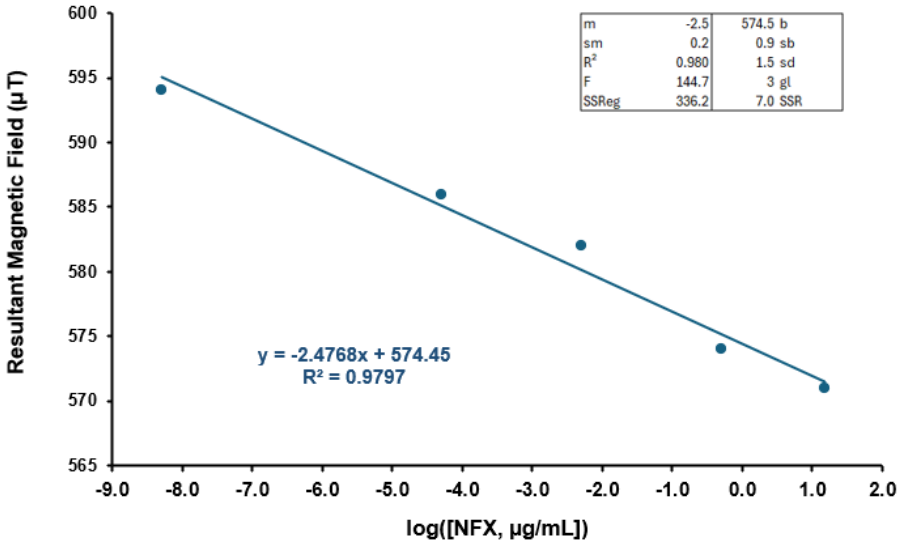

Graph A9 Calibration obtained from readings of the magnetometer integrated into the smartphone after incubation of NFX solutions at different concentrations in sodium polyacrylate spheres of equal size.

It is essential to note that the sodium polyacrylate spheres are positioned at a fixed distance from the smartphone. This setup includes the magnetometer (on the smartphone) placed above the hydrogel/magnet sphere assembly.

The linear fit analysis reveals a correlation between the logarithm of norfloxacin concentration (Log [NFX]) and the resulting magnetic field measured (in μT), with the regression equation $y = 2.4768x + 574.45$ and a coefficient of determination (R^2) of 0.9797. This correlation indicates that as NFX concentration increases, the magnetic field readings decrease. This occurs because the gel spheres swell less, causing the magnets placed directly above them to rise less toward the magnetometer compared to spheres incubated with very low NFX concentrations.

To enhance the sensitivity of this method, it is necessary to optimize several parameters and conditions, such as introducing selectivity mechanisms, ensuring uniform sphere size, and accounting for the influence of temperature on the swelling dynamics of the spheres. These factors point toward potential pathways for refining and characterizing this setup.

Appendix A5. Electrowetting Interfaces and Other "Touchless" Perspectives

In exploring sub-microliter manipulation techniques, the experiment tested an electrowetting module as proof of concept. Within this context, the team attempted to replicate an open-source electrowetting setup known as μDroplet [125]. This system is based on the physical principle of electrowetting on dielectric (EWOD), which operates through the phenomenon of dielectric wettability. The core idea involves manipulating fluid droplets in the microliter or sub-microliter range on a surface by using an electric field to alter the droplet's surface tension.

From a physical standpoint, an external electric field changes the contact angle of a conductive fluid droplet on an insulating surface. The platform consists of a matrix of flat electrodes mounted on a PCB. Over this matrix, the setup applies an insulating dielectric layer (a piece of Parafilm) and a hydrophobic layer (silicone oil). A thin layer of silicone oil also covers the surface to prevent air bubbles between the PCB and the dielectric layer. To observe the operation of the electrowetting platform, a high voltage must be applied to an electrode, causing the droplet to stretch toward this "active" electrode. Under voltage, the resulting electric field attracts the charges within the droplet, reducing the surface tension between the droplet and the electrode. As a result, the droplet moves

dynamically under the influence of electrowetting toward its new position. As shown in Figure A5, the experiment successfully reproduced the µDroplet platform.

Figure A5 Electrode Matrix on µDroplet replica PCB (8x8).

Removing the solder mask from the electrodes and opting for surface finishes such as immersion gold ensures better performance and durability. An Arduino Nano microcontroller receives commands via USB and sends signals to the driver chip to activate the desired electrode. The driver chip (HV507), with 64 channels, converts the Arduino's low-level serial signals into high-voltage signals (up to 300 V), functioning as a voltage amplifier for the electrodes. The power supply must be a switched-mode power source capable of generating voltages between 80-300 VDC from a low input voltage of 5-16 V. An integrated potentiometer allows for manual adjustment of the voltage to optimize particle movement.

Control is managed through computer software that communicates with the Arduino. The user can define the droplet's path by activating or deactivating electrodes on the matrix through interaction with the platform's graphical interface. The software translates this sequence into on/off commands that are sent to the Arduino. Arduino controls the necessary electrode sequence to guide the droplet along the desired trajectory. Both the software and its source code, along with the PCB files and the platform's component list, are available on the project's GitHub page https://github.com/CGrassin/microdroplet_electrowetting.

This setup is part of an open-source initiative. A functional example of the platform is shown in Figure A6, where an L-shaped trajectory is programmed, initially downward, then to the right. The droplet's progression across sequential electrodes is illustrated in Figure A6.

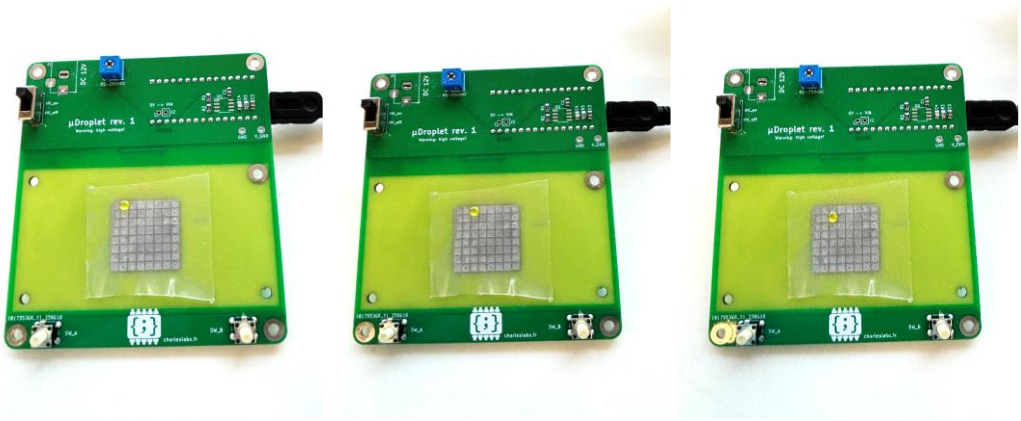

Figure A6 Droplet progression on a microfluidic platform under sequential electrode selection.

From the first to the second image, the bottom electrode is selected, causing the droplet to move right. From the second to the third image, the right electrode is selected, causing the droplet to move downward.

Appendix A6. Alternative Methods for Microfluidic Module Fabrication

The fabrication of microfluidic modules in the context of material testing and manufacturing methods explored various aspects of 3D printing technologies. The starting point involved printing a test module using stereolithography (SLA) to evaluate surface finish and the feasibility of this approach at the micrometer scale, as shown in Figure A9. The design was sourced from an open-source repository [126], and the printing service was provided by the company JLCPCB, which used transparent UV-sensitive 8001 Resin (containing photoinitiators that trigger polymerization under UV light) and applied an oil spray for surface finishing. The thickness of the microchannels was 850 µm for the platforms, except for the circular module, which was 550 µm.

The process takes place in a tank where the resin is exposed to a UV laser beam guided by mirrors. As the laser traces the surface, the resin solidifies. Meanwhile, a platform lowers slightly to expose a new layer, which undergoes the same solidification process when exposed to the UV beam. The following figures illustrate the stereolithographic setup (Figure A7) and the printed components (right side – Figure A8).

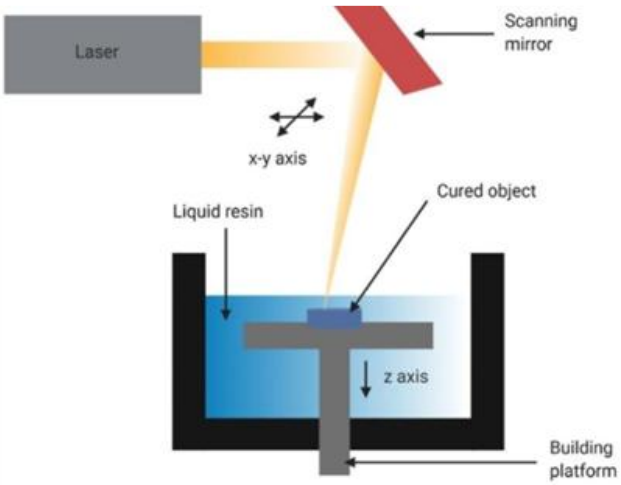

Figure A7 Schematic of stereolithography printing [127].

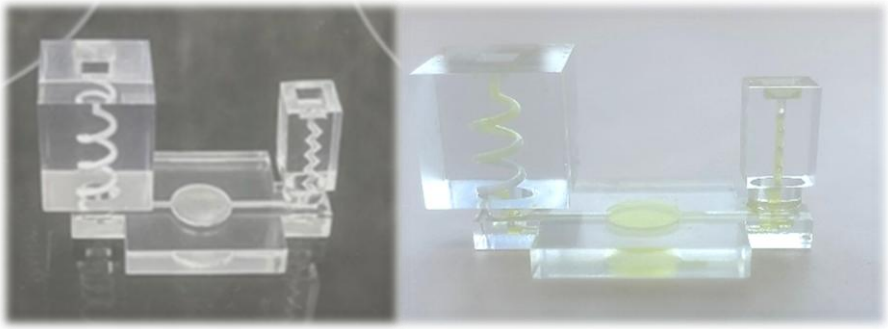

Figure A8 Open-source modular parts [126] printed at JLCPCB using stereolithography. The thickness of the microchannels was 850 µm for the platforms and 550 µm for the circular module. Left: Modular parts assembled before testing. Right: Platform for transporting iron solution.

Among the advantages of obtaining microfluidic modules through this methodology are the high channel resolution (which can reach 20-100 µm) and the smooth surface finish (which helps reduce flow resistance), as well as the freedom to choose the 3D geometry of the part. However, it is important to consider the costs associated with acquiring the equipment and, in terms of high scalability, optimize the design relative to the production time per unit. Additionally, some resins exhibit autofluorescence, which can be a significant source of interference in fluorescence-based detection applications.

Certain low-cost optical setups can be adapted for stereolithographic printing of simpler components. For example, OPU (Optical Pick-Up Unit) systems found in DVD players and gaming consoles can be repurposed for the synthesis of micro- and even nanostructures [128], as illustrated in Figure A9.

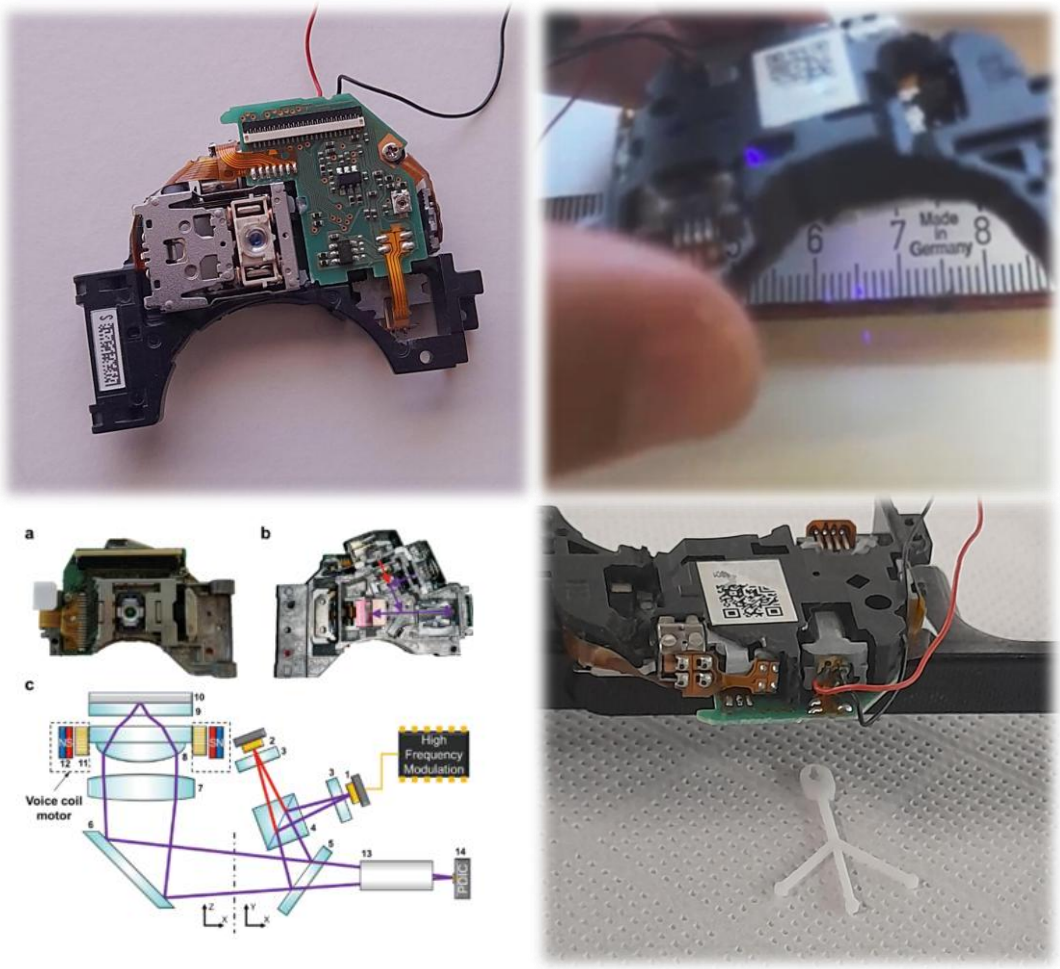

Figure A9 Top: OPU modules illustrating optical components used to focus the light beam in a low-cost micro-nano stereolithography system [128]. (a): top view of the module; (b): bottom view of the module; (c): schematic of lens optical components. Bottom: Left – Replica of the low-cost stereolithography proposal [128] using B150 Xbox One DVD drive modules as setups, accompanied by a current stabilizer circuit of 100mA at 5V. Right – Visualization of the micrometric dimension of the beam projected onto a ruler.

In this setup, based on adapted optical modules, an inverted stereolithography system is structured using an OPU optical system to polymerize a photosensitive resin selectively. The module used, model B150 Xbox One DVD drive, features a 405 nm laser (developed for HD-DVD technology) with micrometer-level resolution. However, other OPU modules exist whose lasers can achieve resolutions of 312.5 nm on the XY axis and 62.5 nm on the Z axis [128].

An experimental replica was carried out to fabricate moulds suitable for synthesizing microfluidic channels via imprinting. Two design models were chosen, with a resolution of 600 µm. The mould designs are available through an open-source reference [129] and are illustrated in Figure A10 and can be used for the synthesis of microfluidic modules through imprinting techniques.

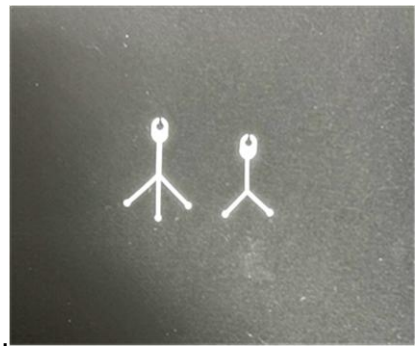

Figure A10 Microfluidic Molds (600×600 µm) printed using a low-cost OPU System via photopolymerization with 405 nm Resin [129].

Continuing with the theme of three-dimensional printing, a second test module, see Figure A11, was developed using the Multi Jet Fusion (MJF) approach, also through a request to JLCPCB's 3D printing services (The thickness of the microchannels is 850 µm). In this method, a thin layer of material (nylon was used in this trial) is spread across a platform similar to the SLA setup, as shown in Figure A12. Then, a printhead moves over the powder, simultaneously applying a liquid fusing agent (where the part will be built) and a detailing agent (along the edges to ensure resolution and fine details). Afterwards, an infrared (IR) unit passes over the platform, and the fusing agent absorbs the IR energy, causing the material to melt and fuse with the previous layer. In contrast, the detailing agent remains in powder form.

Similar to the SLA setup, the platform lowers, and a new layer of powder is added, repeating the process. To support the part being printed, the unfused powder itself is used. This powder can be removed after printing and reused in another print. The primary materials used in this printing method are Nylon (PA12 and PA11), known for their good mechanical properties, durability, and flexibility. The design of the test piece is available in an open-source repository [126]. Compared to SLA, the MJF technique produces parts more quickly and enables isotropic manufacturing (uniform mechanical properties in all directions) with lower cost per unit (multiple parts can be printed in a single batch). Additionally, it does not require support structures during printing, as the detailing agent serves that role. However, the porous surface and the grey/black finish may limit applications that require transparency. The initial setup cost of the printer and the post-processing steps (such as removing residual powder) can increase overall expenses if the technique is not applied on a large scale.

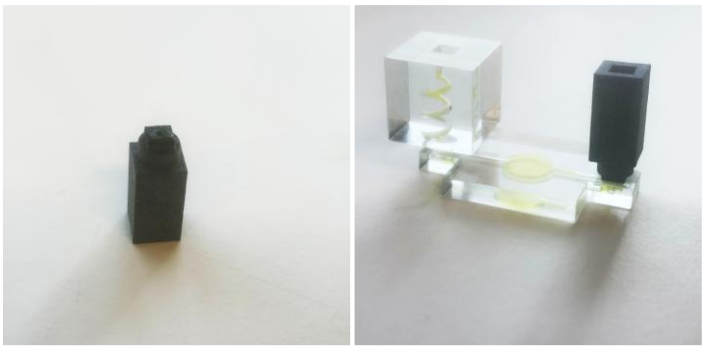

Figure A11 Module printed using the Multi Jet methodology, produced by JLCPCB 3D printing services [126]. The thickness of the microchannels is 850 µm. Left: Nylon module. Right: Coupling to stereolithographic parts.

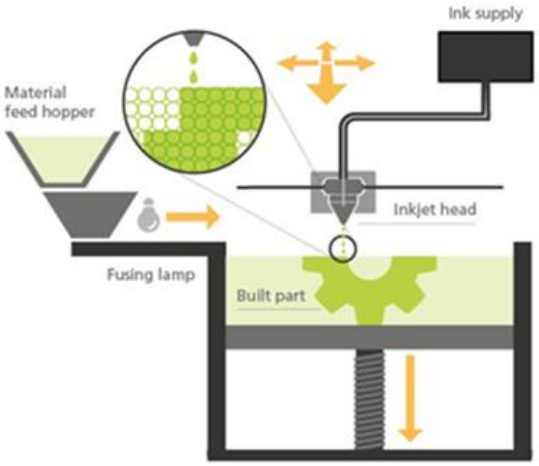

Figure A12 Schematic representation of printing using MJF [130].

Another approach very similar to MJF is Selective Laser Sintering (SLS), as shown in Figure A12. This technology was tested using a module sourced from an open-source database [126] and printed through JLCPCB's 3D printing service, as documented in Figure A13. The thickness of the microchannels is 550 µm. In summary, printing through this process involves building a chamber filled with powdered substrate material. The chamber must be heated to a temperature just below the powder's melting point. After that, the powder is added in thin layers and spread across the platform. A high-power laser, directed by mirrors, scans the surface of the powder. As it moves across the surface, it selectively fuses the powdered material to construct the part. The unfused powder remains in its original state, acting as a support material.

Sintering occurs layer by layer, with the platform lowering after each layer to allow the addition of a new one until the part is complete. The detail resolution may be slightly lower compared to SLA systems (Figure A14).

At the end of the process, the sintered part is excavated from the unfused powder (which served as support), and this powder can be reused in another print. The main advantages of SLS include design flexibility, isotropic part production, and the ability to fabricate complex structures without the need for support. On the other hand, post-processing and cleaning to remove residual powder, as well as the rough and porous surface finish, are potential drawbacks, along with the cost of acquiring an SLS setup. Finally, the resolution of fine details may be slightly inferior compared to SLA systems.

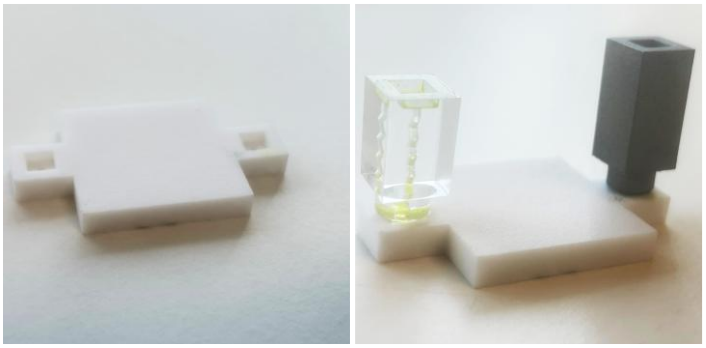

Figure A13 Module (thickness of the microchannels is 550 µm) printed using laser sintering technology through services requested from JLCPCB [126]. Left: View of the module obtained by selective laser sintering. Right: Coupling to the microfluidic platform; addition of the stereolithographic module and the Nylon module obtained by MJF.

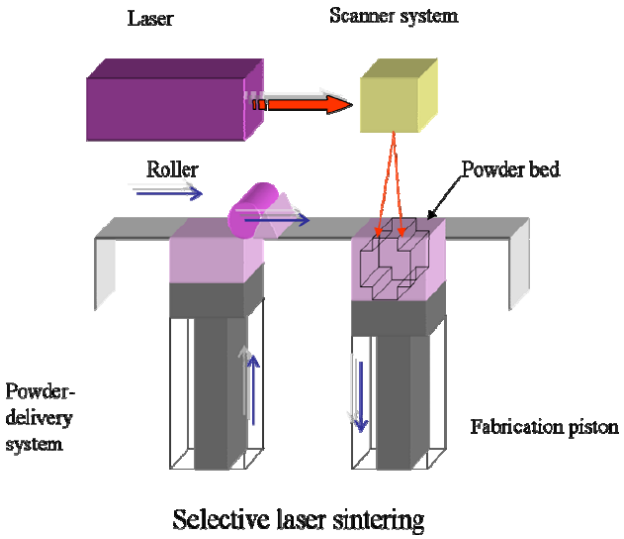

Figure A14 Schematic representation of setup and module printing using selective laser sintering [131].

Considering the possibility of adapting microfluidic detection methods to other setups in the future, this work aimed to explore substrates that could be used in contexts requiring high mechanical strength and durability, such as those made of metals. These functionalities require materials that are corrosion-resistant and capable of operating under high-temperature and high-pressure conditions. Microfluidic materials for biological applications were also considered, with a focus on aspects such as biocompatibility.

To bridge the two seemingly distinct topics of mechanical robustness and biomedical compatibility, a focus was placed on metal alloys, seeking to understand how 3D synthesis methodologies perform when working with these types of substrates. In this context, two materials were tested as substrates, each used to fabricate microfluidic modules through different methodologies. One of these substrates was 316L stainless steel, selected for microfluidic module fabrication using the Binder Jetting technique, as illustrated in Figure A16. The module design was sourced from an open-source repository [126], and JLCPCB's 3D printing services carried out the printing, and the thickness of the microchannels is 850 µm. This methodology involves using a binding agent that joins powder particles on a build platform, while a printhead selectively deposits the binder onto the powder layer, as shown in Figure A15. Through capillary action, the binder spreads among the particles, facilitating the formation of the part.

The procedure is repeated layer by layer, following the same platform movement principle used in previous printing methods. After printing, the part containing both bound and unbound powder is removed from the bed. The bound powder part is then subjected to a curing process in a high-temperature furnace under a controlled atmosphere, where the binder is burned off and the particles fuse, forming a consolidated 3D structure. It is essential to note that the part undergoes shrinkage during curing due to the high temperature, necessitating dimensional compensation in the initial design.

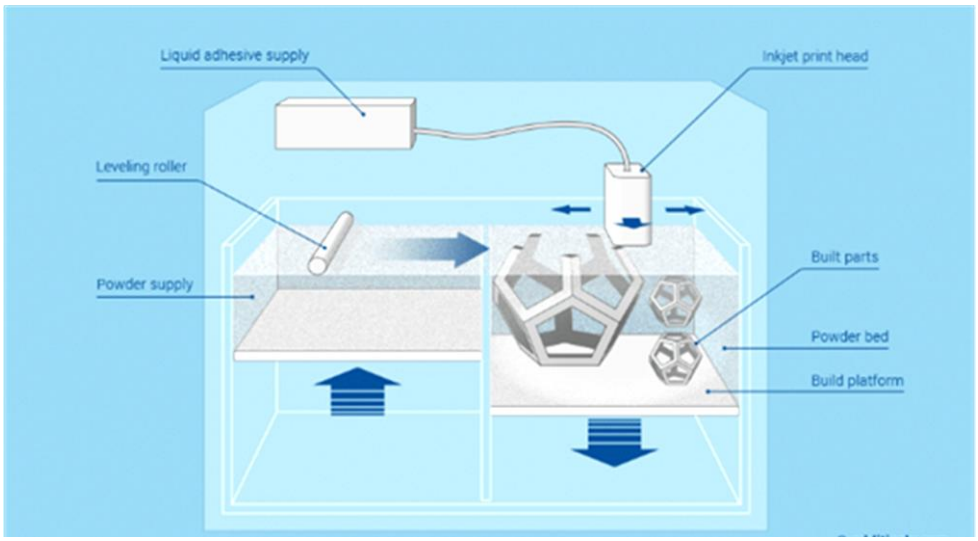

Figure A15 Schematic representation of the setup for printing using Binder Jetting[132].

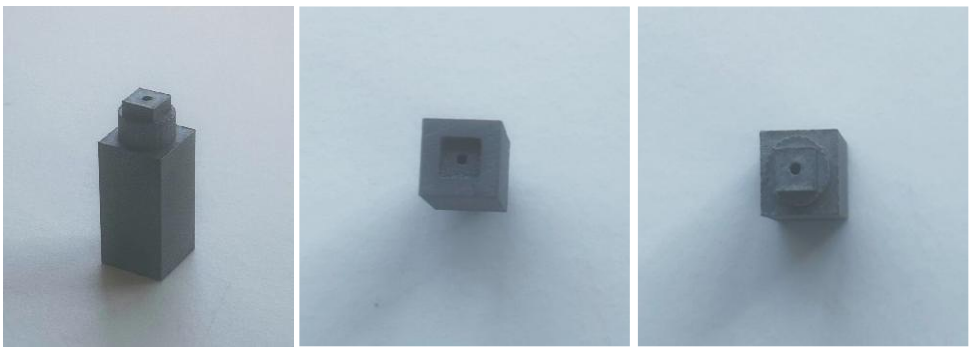

Figure A16 316 stainless steel microfluidic module printed via Binder Jetting through services provided by JLCPCB [126]. The thickness of the microchannels is 850 µm. Left: Overview of the part; center: View of the lower finish; right: View of the upper finish.

Another metallic substrate tested was titanium (Figure A17), using the Selective Laser Melting (SLM) technique. In SLM systems, a high-power laser generates dense and complex parts layer by layer through a process similar to SLS, differing mainly in the material (metal powder) and the need for complete melting, as shown in Figure A18. The printing environment must be filled with inert gas to prevent oxidation of the material during the high-temperature process. The precision and level of detail in the process depend on factors such as laser power, scanning speed, and focal point size. Other metallic materials can also be used, such as stainless steel (316L) and nickel alloys (Inconel). It is essential to consider that the laser must be selected based on the power required to raise the material's temperature above its melting point, allowing it to melt and solidify rapidly. The advantages and disadvantages are similar to those mentioned for the SLS methodology. For conceptual demonstration, a module was used whose

design originated from the previously cited open-source repository [126]. JLCPCB's 3D printing services were then utilized for printing. Figure A18 illustrates the final part and outlines the SLM process.

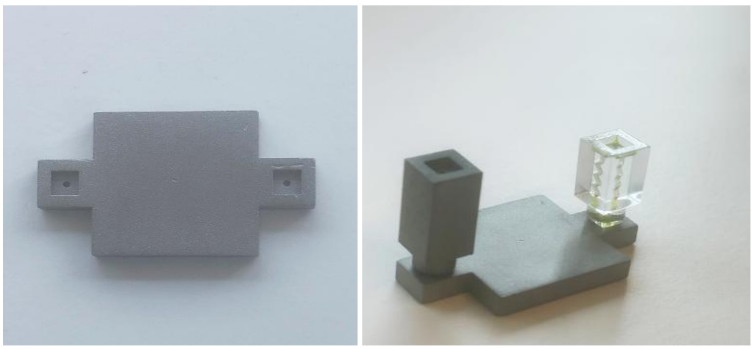

Figure A17 Left: Titanium module printed using SLM technology through services provided by JLCPCB [126]. The thickness of the microchannels is 550 µm. Right: Coupling of the titanium module to steel parts and a part produced by stereolithography.

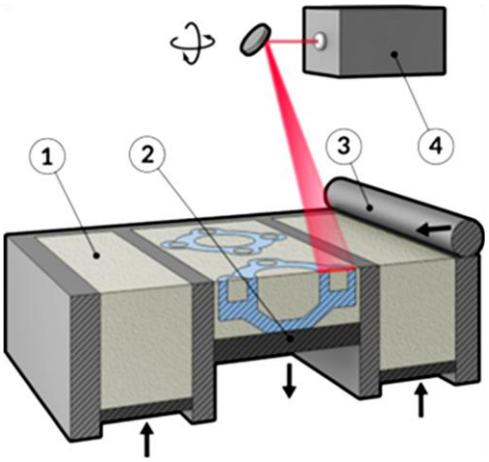

Figure A18 SLM Manufacturing machine [133].

In SLM Manufacturing, the metal powder (1) is heated and spread in a thin layer over the platform (2). A pulsed laser (4) sinters the powder particles, fusing them to form the cross-section of the CAD model. The platform is then lowered, the roller (3) adds a new layer of metal powder, and the process repeats, building the object layer by layer [133].

Finally, the work explored various perspectives on the fabrication of molds and counter-molds for the production of microchannels through imprinting (soft lithography), with a focus on subtractive strategies. One of the approaches applied was CNC machining (Computer Numerical Control) to achieve micrometric profiles on an acrylic plate, as

shown in Figure A19. CNC is a subtractive manufacturing method, where material is removed from a solid block to obtain the desired profile.

The methodology involves a computer program (G-code) responsible for translating the 2D or 3D structure into machine commands. These commands control the speed and position of a milling tool, which moves across the processed material (in this case, an acrylic block). The contact of the milling tool must be sufficient to overcome the material's resistance and allow its removal. The tool must operate at a speed capable of surpassing this resistance. However, the resulting friction generates heat, which can lead to unwanted deformation, especially affecting the final dimensions of the counter-mold. In the end, this may compromise the quality of the part. Therefore, it is necessary to incorporate heat dissipation systems during the counter-mold synthesis process.

In addition to acrylic (PMMA), other materials such as aluminum and steel can also be used, offering reusable, durable molds that are chemically resistant and long-lasting. The advantages to highlight are, in fact, the precision for simpler designs, tighter tolerances, and superior finishes, especially when working with metallic and acrylic substrates, which stand out when compared to the 3D printing methods mentioned above. However, there is material waste, the design is limited in terms of three-dimensional complexity and interconnections, and the cost of acquiring or renting the equipment for work time is high. Additionally, the synthesis time is significantly longer than that of other methods, requiring considerably more time to complete. For the CNC demonstration, an open-source design [134] was used and manufactured through a service provided by PCBWAY CNC.

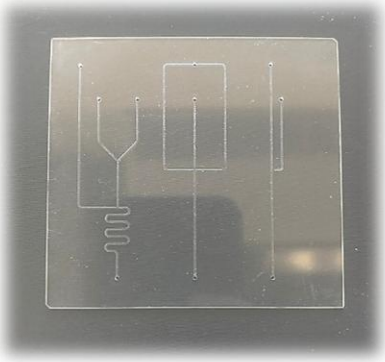

Figure A19 Acrylic counter-molds for Microfluidics produced by CNC machining [134].

The design, shown in Figure A19, is open source [134], and the machining service was provided by PCBWAY. These molds can be used to cure polymers for the fabrication of

templates suitable for microfluidic synthesis via imprinting. The final subtractive approach involved creating a sacrificial mold that can be embedded in a polymeric material, such as PDMS. Once the PDMS is cured, the sacrificial material can be dissolved and removed, resulting in microchannels within the PDMS structure. In this work, the synthesis of polyvinyl alcohol (PVA) molds was illustrated, produced via Fused Deposition Modelling (FDM). The design of these PVA molds can be sourced from an open-source reference [129] and dimensions adapted for a channel cross-section of 800×800 µm. This mold, which is mechanically and hygroscopically stable, dissolves completely in water, offering a fast method for fabricating complex microchannels (including intricate geometric features and multilayered microchannels).

The main advantages lie in simplicity and low material costs. However, the major drawback is the need for access to a 3D printer with sufficient resolution for microfluidic applications. Nonetheless, the cost of such printers is significantly lower compared to other methods. Figure A20 shows the PVA mold obtained through FDM.

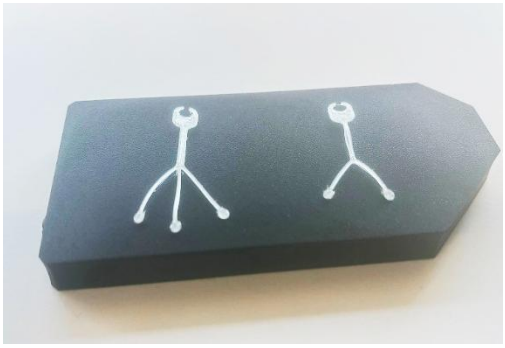

Figure A20 PVA molds for microfluidic channels produced using conventional 3D printing [129]**.**

These molds were designed using an open-source model [129] and serve as sacrificial templates that dissolve in water. Once embedded in liquid PDMS, and after the PDMS has cured, the molds can be removed simply by adding water. This process leaves behind well-defined microchannels within the solidified PDMS structure.

For the purpose of comparing the costs associated with the synthesis of microfluidic modules through the combination of substrate selection and manufacturing method, Table A1 summarizes the expenditure for each item (module, mold, or counter-mold) mentioned in this study, with 3D printing printing standing out in terms of cost-effectiveness.

Table A1 Unit cost for each methodology referenced.

Method	Cost in euros (€) per piece
SLA	€1,5
SLA-OPU DIY	€1,0 (OPU setup module costs €10 via e-commerce)
MJF	Less €1,0
SSL	€2,0
SLM	€8,0
BJ	€7,0
CNC	€35,00
Sacrificial Mold	€1,0
Stratasys Neo® 450/800 (This work)	Less €1

Note that the printing method chosen for the synthesis of microfluidic modules represents one of the most economical strategies when compared to modules synthesized by other methods. Finally, Table A2 gathers the information regarding the channel thicknesses obtained in each module.

Table A2 Microchannel resolution.

Method	Dimensions channel cross-section (adapted)
SLA	550×550 µm and 850×850 µm
SLA-OPU DIY	600×600 µm
MJF	850×850 µm
SSL	850×850 µm
SLM	550×550 µm
BJ	850×850 µm
CNC	200×200 µm
Sacrificial Mold	800×800 µm
Stratasys Neo® 450/800	500×500 µm

SLA: Stereolithography; SLA-OPU: Stereolithography Optical Processing Unit; DIY: Do It Yourself; MJF: Multi Jet Fusion; SSL: Selective Sintering Laser; SLM: Selective Laser Melting; BJ: Binder Jetting; CNC: Computer Numerical Control.